UNIVERSIDADE DE SÃO PAULO
INSTITUTO DE FÍSICA DE SÃO CARLOS

Yajaira Dalila Rivero Jerez

Observation of collective bistability in an ultracold cloud of strongly driven strontium atoms interacting with a ring cavity

São Carlos

2022

Yajaira Dalila Rivero Jerez

Observation of collective bistability in an ultracold cloud of strongly driven strontium atoms interacting with a ring cavity

Thesis presented to the Graduate Program in Physics at the Instituto de Física de São Carlos of Universidade de São Paulo, to obtain the degree of Doctor in Science.

Concentration area: Basic and Applied Physics

Advisor: Prof. Dr. Philippe Wilhelm Courteille

Original version

São Carlos

2022

Rivero Jerez, Yajaira Dalila
Observation of collective bistability in an ultracold cloud of strongly driven strontium atoms interacting with a ring cavity / Yajaira Dalila Rivero Jerez; advisor Philippe Wilhelm Courteille -- São Carlos 2022.
133 p.

Thesis (Doctorate - Graduate Program in Theoretical and Experimental Physics) -- Instituto de Física de São Carlos, Universidade de São Paulo - Brasil , 2022.

1. Strontium. 2. Ring cavity. 3. Saturation induced bistability. 4. Collective coupling. 5. Resonant regime. I. Courteille, Philippe Wilhelm, advisor. II. Title.

FOLHA DE APROVAÇÃO

Yajaira Dalila Rivero Jerez

Dissertação apresentada ao Instituto de Física de São Carlos da Universidade de São Paulo para obtenção do título de Doutora em Ciências. Área de Concentração: Física Teórica e Experimental

Aprovado (a) em: 14/12/2022

Comissão Julgadora

Dr(a). Philippe Wilhelm Courteille

Instituição: (IFSC/USP)

Dr(a): Sandra Sampaio Vianna

Instituição: (UFPE/Recife)

Dr(a). Sebastião José Nascimento de Pádua

Instituição: (UFMG/Belo Horizonte)

Dr(a): Celso Jorge Villas Boas

Instituição: (UFSCar/São Carlos)

Dr(a): Marcelo Martinelli

Instituição: (IF/USP)

to the curious child (still inside each one of us) of the reader,
to those who don't give up in their pursuit for knowledge,
especially for the dreamers,
for the ones that keep thinking of ways to make beautiful science...
keep it up!

ACKNOWLEDGEMENTS

First, to my advisor: You gave me the opportunity to enter this world by just trusting in my potential, even though I had zero experience. You supported me and believed in me like a friend. You took my hand and carefully showed me science through your eyes like a father to a son. And you brought me back to the right path, every time I lost focus, like a good mentor. I will always be grateful to you for everything. Danke schön Philippe!

To my lab partners and colleagues, over all these years. Each one of you gave me the tools to become what I am today, none of this would be the same without you. Every talk, every coffee, every hug, every advice, and critique... Thank you guys, I'm so lucky to meet you all.

To Yaja and Paula, my mom and sister, las mujeres mas importantes de mi vida! Gracias por todo el apoyo y amor que me dan, por cuidarme y aguantarme a pesar de todo. Yo soy fuerte porque las tengo a ustedes como inspiración, las amo mucho mis bellas.

To (this paragraph is the only one that will not be read by the person for which is intended) Rodolfo, my father. Thank you for everything you taught me viejo, the curiosity, the kindness, the humor, the energy, the strength... I still miss you, but I'm consoled by making you feel proud... Yes I know, we never stop learning, don't worry this path is still at the beginning... Te amo tigre.

To all the friends I have(had), maybe I meet you on this path, maybe we know from before and you also saw me evolving. Especially, to the people I've lived with, vocês são minha segunda familia. I'm deeply thankful for all I learned with you. Thank you for the support, and thank you for being there.

The pirate's queen is nothing without her friends to protect her.

To all the personnel of USP, administrative, secretaries, people at the offices and technicians, professors, and every other friendly helper. Also, thanks to the people in TOptica and Thorlabs. Thank you for making it easier to do science.

Ao Brasil, como pais, pela oportunidade de estudos que me foi dada e pela maravilhosa estadia (as pessoas, a comida, a música, a lingua... amo muito este país!). Estarei sempre em divida com vocês pelo amor recebido, muito obrigada!

Thank you to CAPES, CNPq, and FAPESP, the Brazilian agencies that make it possible for everyone to study and learn in this beautiful country. The path is easier if we all work together. This study was financed in part by the Coordenação de Aperfeiçoamento de Pessoal de Nível Superior – Brasil (CAPES) – Finance Code 001

ABSTRACT

RIVERO JEREZ, Y. D. **Observation of collective bistability in an ultracold cloud of strongly driven strontium atoms interacting with a ring cavity**. 2022. 133p. Thesis (Doctor in Science) - Instituto de Física de São Carlos, Universidade de São Paulo, São Carlos, 2022.

We report on our progress in the construction of a machine capable of cooling Strontium atoms to ultra-cold temperatures, to interact collectively with the modes of a ring cavity. We present the first observation of a novel manifestation of saturation-induced optical bistability in a resonantly pumped optical ring cavity, interacting with a narrow atomic transition cloud. The bistability emerges, above a critical pump rate, as an additional peak in the cavity's normal-mode spectra near the atomic resonance. The new regime addressed for our machine takes advantage of the narrow atomic transition enabling the observation of bistability in a strong resonant regime where the atoms couple collectively to the cavity.

Keywords: Strontium. Ring cavity. Saturation induced bistability. Collective coupling. Resonant regime.

RESUMO

RIVERO JEREZ, Y. D. **Observação da biestabilidade coletiva em uma nuvem ultrafria de átomos de estrôncio fortemente acionados interagindo com uma cavidade anelar**. 2022. 133p. Tese (Doutorado em Ciências) - Instituto de Física de São Carlos, Universidade de São Paulo, São Carlos, 2022.

Relatamos nosso progresso na construção de uma máquina capaz de resfriar átomos de estrôncio a temperaturas ultra-frias, para interagir coletivamente com os modos de uma cavidade em anel. Apresentamos a primeira observação de uma nova manifestação de biestabilidade óptica induzida por saturação em uma cavidade de anel óptico bombeado ressonantemente, interagindo com uma nuvem de transição atômica estreita. A biestabilidade surge, acima de uma taxa de bombeamento crítica, como um pico adicional nos espectros de modo normal da cavidade próximo à ressonância atômica. O novo regime endereçado para nossa máquina aproveita a estreita transição atômica permitindo a observação de biestabilidade em atomos fortemente acionados em ressonacia acoplados coletivamente à cavidade.

Palavras-chave: Estrôncio. Cavidade anelar. Biestabilidade induzida por saturação. Acoplamento coletivo. Regime ressonante.

LIST OF FIGURES

Figure 1 – Bloch oscillations in a ring cavity as a non-destructive method to measure matter-wave interferometry. 27

Figure 2 – Level scheme of strontium: wavelengths and linewidth (in parentheses). Values references: SANSONETTI*et al.*(1) and STELLMER(2) 32

Figure 3 – Technical drawing of the 2D-MOT and the science chamber. Note the ring cavity mounted inside the science chamber. 33

Figure 4 – Scheme of the distribution of the Blue light produced by the SHG. The Doppler-free spectroscopy technique is pictured at the bottom right. After frequency-shifting the laser light with the help of AOMs, the wavelengths are sent to the experiment via optical fibers. 36

Figure 5 – Lock-in spectroscopy signals: the blue curve is the signal provided by the photo-detector of the probe beam as a function of the laser frequency (The scan is being performed in the piezo of the master laser), the modulation of the Lock-in is appreciated all across the signal. The orange curve is the error signal created by the demodulation of the Blue curve. 37

Figure 6 – 2D-MOT scheme including the non-colinear input of the extra slower beams, also called Zeeman beams 39

Figure 7 – Photos of:(right) side view of the 2D MOT while the push beam is on. Notice the tail of atoms being pushed from left to right of the center of the window. (left) Top view of the 3D Blue-MOT and the cavity. . . . 40

Figure 8 – Time sequence for the production of a Blue MOT and subsequent imaging of the cloud. For the production of a red MOT or for cavity trapping we add sequences before the imaging stage. The main features of each controlled parameter are pictured, nonetheless, is important to notice that the time is not at scale since for loading the Blue-MOT the time is 1200 ms while the power ramp at the last stage occurs in 6 ms. Or analogously the Magnetic field switch-off takes 0.16 ms, and the probe pulses have a duration of 20 ns. 41

Figure 9 – (a) Number of atoms in the blue MOT as a function of the intensity of the slower beams of the 2D-MOT. (b) Blue-MOT temperature (Each point represents a TOF sequence) as a function of the final intensity of the 3D-BlueMOT beam intensity. The change experienced by the cloud's size is also shown in contrast to the temperature behavior. . . . 42

Figure 10 – Blue MOT loading and decay after switching off the 2D-MOT push beam as a function of time. The red curve is an exponential fit to the experimental data from which the time constants are extracted. 42

Figure 11 – Scheme of the setup used to lock the master laser in the super-cavity (upper-left) and to perform injection lock. Colored arrows at the right of the beams (red lines) indicate the propagation direction. The scheme also pictures the beat measurement technique. 45

Figure 12 – Characterization of the performance of the Pound-Drever Hall (PDH) stabilization. Beat signal of two independent PDH locked lasers with 464 MHz frequency difference recorded with (a) 30 kHz and (b) 10 Hz bandwidths resolution of the spectrum analyzer. The PDH modulation sidebands are visible as small peaks at ±20 MHz. The red curve in (b) is a Lorentzian fit with an FWHM of 450 Hz. This allows us to assert that any one of the lasers has an emission bandwidth below this width. 46

Figure 13 – (a) Beat of the correlated lasers Master and Slave showing the reduction of the linewidth after the injection process lock. The curves were frequency-shifted for easier visualization. When the injection process occurs the spectrum shows the modulation bands of the master, as well as 'extra bands' that come from the beat of the bands of the slave with the bands of the master. Using the light transmitted from the SC we may avoid this behavior. (b) 10 Hz Bandwidth resolution of the correlated lasers beat, the red curve is a Lorentzian fit with an FWHM at 3 dBm of 10 Hz. (c) The blue curve shows the spectrum of the beat frequency between laser 1 (ν_{las1}) and the red MOT light (ν_{redMOT}) when the light injected into the slave laser is frequency-modulated with a triangular wave-function with a fixed peak-to-peak frequency excursion of 8 MHz. The red curve has been taken without this modulation. . . . 47

Figure 14 – Locking scheme illustrating the frequency shifts and locking points of the lasers with respect to the super cavity spectrum (upper peak array). The ^{88}Sr resonance ν_{Sr} is shown by a vertical dashed line. The acronyms are Pound-Drever-Hall (PDH) stabilization, and acousto-optic modulator (AOM). 48

Figure 15 – (a) Time sequence for the production of a Red MOT and subsequent imaging of the cloud. (b) Switching of the magnetic field gradient (axial direction) between the blue and the red MOT. (c) Implemented red MOT frequency (blue) and power ramp (red). For clarity of illustration the modulation frequency, which in reality is 55 kHz in the first part and 25 kHz in the second, has been reduced by a factor of 200. 49

Figure 16 – Evolution of the measured atom number (blue curve) and temperature (red curve) for different times in the ramp. The insets are OD images of the cloud at different times, the background changes since the image are normalized to the maximum intensity. (inset) Red mot with 4x zoom and the pancake shape is visible. 50

Figure 17 – Lifetime measurement of the RedMOT cloud. The red line represents an exponential fit from which the time constants are extracted. This measurement is performed by varying the time of the last stage of the modulation ramp in the frequency of the red MOT. 52

Figure 18 – Measure of the Blue transition linewidth using the Red cloud. The Blue dots represent the mean of two experimental measurements. The scanned parameter was the frequency of the blue light used to image the atoms. The red line is a Lorentzian fit of our experimental data, from which the linewidth of the transition was extracted. 52

Figure 19 – (left) Ring cavity inside of the science chamber (Solidworks schematic). (right) The 2D scheme at the cavity plane of the input and output beams in the science chamber. The red and orange light beams represent the different directions of light coupling and the expected transmissions. 55

Figure 20 – (left) Photo of the Blue-MOT in the cavity plane(Dec-2021), where the top HR mirror displacement is also appreciated. (right) Scheme of the input and output beams in the science chamber for the tilted cavity, a black line was added to serve as a guide. 56

Figure 21 – Optical setup of the cavity spectrometer. Colored arrows at the right of the beams (colored blurred lines) indicate the propagation direction. Black solid lines represent electronic connections. The master laser is tightly locked to a reference cavity (Super cavity) via a Pound-Drever-Hall servo (PDH), tuned close to the narrow atomic resonance. It serves for cooling the atomic cloud (red MOT). The ring cavity length can be controlled via the piezo (PZT) located in one of the high reflectors (HR). The PZT is locked via PDH to a second laser (Red 2). The light of the master and the red2 lasers is overlapped in a fast photo-detector (PD). The frequency difference (Beat) is phase-locked via a DPLL to laser red2. The light of the laser red2 inside the ring cavity generates an optical dipole potential for the atoms in the red-MOT. (inset) Locking scheme illustrating the frequency shifts and locking points of the lasers with respect to the atomic resonance, the cavities spectra are pictured in scale. 57

Figure 22 – Locking scheme illustrating the frequency shifts and locking points of the lasers with respect to the atomic resonance. The cavities transmissions spectra (TEM_{00}'s) quasi at scale, is also pictured. The lock chain direction is pictured as $\longmapsto$. In that way, the laser that interacts with the narrow atomic resonance is phase-locked to ($\longmapsto$) the master laser via injection lock. The master laser by its time is locked to ($\longmapsto$) the closest super cavity mode via PDH and a FALC. The ring cavity piezo follows ($\longmapsto$) the Red_2 laser through the scan module and a Digilock. The PDH modulated Laser2 can simultaneously be arbitrary (limited to frequency differences of $\Delta\nu_{\pm|\text{master}-\text{red2}|} < 6\text{GHz}$) locked to ($\longmapsto$) the stable master laser via a DPLL and a FALC. 58

Figure 23 – Long-term characterization of the frequency drifts of the ring cavity. The black curve shows the natural drifts of the ring cavity. The red curve shows the same signal when the ring cavity was additionally locked to laser 1 via a lock-in amplifier and PID servo electronics (Toptica, DigiLock). 59

Figure 24 – (a) Beat signal of the two mutually phase-locked lasers recorded with 30 kHz resolution bandwidth of the spectrum analyzer. For this measurement, the lasers had a frequency difference of 1.6 GHz. (b) Same as (a) but with 3 kHz resolution bandwidth. (c) Same as (a) but with 10 Hz resolution bandwidth. (d) Transmission spectrum of the supercavity. 60

Figure 25 – Transmission line-shapes and Lorentzian fit (red) of the mode profiles for the (blue) High finesse and (green) low finesse polarization. 62

Figure 26 – Photo of cavity mirrors and the scattered light of the locked cavity used to calculate the distances between mirrors. The red arrows indicate the spots where the beam is reflected in the mirror. The side of the incoupler mirror (left) and the HR mirror (bottom and top) are used as calibration (l = 5mm). 63

Figure 27 – Characterizations of the displacement coils on the $\hat{x}$ direction. a) While we increase the current of the coils the red cloud displaces linearly, correspondingly with the red MOT gradient. b) The number of atoms measured from the cloud decreases drastically when the position changes further than the beam's waist/2. 70

Figure 28 – Time sequence for introducing the red cloud inside of the Cavity mode. Analogous to the scheme already presented for the blue cloud the time is not at scale, further details can be found in the main text. 71

Figure 29 – Absorption images of the atoms entering in the dipolar trap a) One-sided pumping trap, b) Both-sided pumping trap. The white arrows represent the cavity mode direction and gravity. c) Experimental setup used to perform the measurements shown in this chapter 72

Figure 30 – Comparison between the absorption images taken with the camera a) aligned with the gravity and b) aligned with the cavity mode direction. 72

Figure 31 – Step by step of the Red cloud entering the cavity trap for decreasing the current in the displacement coils. a) The red cloud at TOF= 2 ms; b,c,d) unidirectional pumping of the cavity light. e) bidirectional pumping, creating a standing wave that avoids the cloud from falling for gravity, TOF= 2 ms, T_{hold} = 4 ms, corresponding TOF of the atoms that didn't enter the trap TOF_{redMOT} = 6 ms. 73

Figure 32 – Lifetime measurement of the atoms inside of the dipolar trap created in the cavity mode. The red line on top of the experimental data is an exponential fit used to extract the time constant. 73

Figure 33 – Studies of the trapping of atoms as a function of the detuning for both sides pumped at fixed I. (a) The position of the atoms, as extracted from the fitting of our absorption imaging. (b) The atom number and the analogously the optical density dependence. (c) The temperature, measured at each fitting direction, as a function of the detuning of the cavity from the resonance. 74

Figure 34 – Schematics illustrating redistribution of atoms (purple dots) from the initial random distribution to a periodic density grating. The density grating is ($b = 0$) initially shallow, but becomes deeper ($b = 1$) as a consequence of the interference between the laser beam and the backscattered light. 79

Figure 35 – Bistability induced by saturation as a function of η_+ and (a) varying the collective cooperativity $N\Upsilon$ and (b) the atomic transition linewidth $\Gamma' \equiv 4g^2/(N\Upsilon\kappa)$. The different colors denote three different transmissions $T_\pm$ obtained from the analytical solution of Eq. 3.8. 82

Figure 36 – Normal-mode spectra $T_\pm$ calculated using Eq. 3.29 for various pump rates (d) $\eta_+ = 1\Gamma$, (e) 160Γ, and (f) 250Γ and all other experimental parameters as specified in the text. The anti-diagonal black dashed lines show the mode of an empty cavity ($N = 0$). The dash-dotted black lines are calculated from 3.9, and the dotted black lines from 3.10 using a saturation broadening estimated from $\Omega_\eta = 2g\eta_+/\kappa$. The bistable region is delimited by a red dotted line. 84

Figure 37 – Normal-mode splitting $T_\pm$ calculated using Eq. 3.12 with $\Gamma = 0.0022\kappa$, $g = 0.0027\kappa$, $N = 100000$, and $b_\pm = 1$. Furthermore, for (a) $\Omega = 0$, $\eta_- = \eta_+$; the dashed line is calculated from 3.48. (b) $\Omega = 200\Gamma$, $\eta_- = \eta_+$; the dispersive dashed line is calculated from 3.49. (c) $\Omega = 0$, $\eta_- = 0$; the anti-diagonal dashed line is calculated from 3.50, and (d) $\Omega = 200\Gamma$, $\eta_- = 0$. 85

Figure 38 – Scheme of the lasers controlling the atom-cavity interaction. Laser 1, which is tightly locked to a reference cavity via a Pound-Drever-Hall servo (PDH), is tuned close to the narrow atomic resonance (Δ_a). It serves for cooling the atomic cloud (red MOT) and for driving one or two of the counter-propagating modes ($\alpha_\pm$) of the ring cavity formed by three mirrors, the input coupler (IC), and two high reflectors (HR). The transmission through the high reflectors ($T_\pm$) is recorded. A second laser (laser 2) is phase-locked (DPLL) to laser 1 at 4 GHz below the atomic resonance. In contrast to laser 1, its intensity is high. Overlapped with laser 1 and also coupled into one or two counter-propagating modes of the ring cavity it generates an optical dipole potential for the atoms. Transmission spectra showing normal mode splitting are obtained by ramping ν_{rf} and/or ν_{mw}. 87

Figure 39 – Time sequence for probing the normal mode splitting. Analogous to the schemes already presented, the time is not at scale, further details can be found in the main text. 88

Figure 40 – Measured transmission spectra (blue crosses) of the ring cavity T_+ (b) without and (d) with atoms. The curve in (d) shows a typical normal-mode splitting. The red lines are fits using (a) a Lorentzian profile and (b) the normal mode expression 3.12 89

Figure 41 – (top) Avoided Crossing maps and (bottom) Normal-mode spectra ($\Delta_{ca} = 0$) $T_\pm$ Measured for different values of probe intensity. The dash-dotted line describing avoided crossing is calculated from 3.9, the anti-diagonal dashed line is calculated from 3.50, and the dispersive dotted line is calculated from 3.12 using as Rabi frequency the value extracted from the fit of the experimental measurement. 90

Figure 42 – (top) Avoided crossing of the normal-mode spectra $T_\pm$ Measured with different scan directions of the probe laser.(a) from $-2 \rightarrow 2$, (b) from $-2 \leftarrow 2$. As pictured with an arrow at the left of the scanned parameter. (bottom) Avoided Crossing maps using as Rabi frequency the value extracted from the fit of the experimental measurement presented in (a); (c) $\eta_+ = 115\Gamma$ (d) Zoom of the bistable region. 91

Figure 43 – Illustration of Bloch oscillations of a matter wave inside of an optical potential seen in (a) real space, (b) momentum space, and in (c) the moving frame. 97

Figure 44 – Dynamics of Bloch oscillations (a-b) for $W_0 = 0.4\omega_{rec}$, (c-d) for $W_0 = 0.8\omega_{rec}$, and (e-f) for $W_0 = 1.6\omega_{rec}$. Furthermore, $\omega_{rec} = (2\pi)\ 4.8$ kHz and $\nu_{blo} = 0.05\omega_{rec}$. 100

Figure 45 – Bloch parameter simulation, according to equation 4.20, as a function of the trap detuning for a fixed gain, the lines limit gains of 10 and 400 respectively. The shaded blue area represents the band at which BO can be observed. 101

Figure 46 – (a,c,e) Calculated displacement (in pixels for our setup) for a free fall cloud (kicked at different directions ($\uparrow = y_{0+}$ and $\downarrow = y_{0-}$)), for different temperatures, as a function of the time of flight (TOF). The error bar describes the thermal expansion of the cloud-centered at the position displacement. (b,d,f) shows the net separation expected for different temperature clouds. 103

Figure 47 – Typical experimental characterization of the absorption images acquired in a BO experiment, TOF= 7 ms, $V^{\updownarrow}_{0,dip}/\hbar = 7\omega_{rec}$. a,b) Relative initial position of the cloud in the specified direction, the error bars correspond to the rms of the cloud. c) Number of atoms, and optical density of the cloud as a function of time. d) FFT of the parameters analyzed. 107

Figure 48 – Scheme of the Absorption imaging system: A resonant laser beam interacts with the cloud and the absorbed part is imaged in a camera to extract the OD. The lenses are used to zoom in (or zoom out) without losing resolution. 123

Figure 49 – a)OD: Resulting OD image of an atomic cloud. b) I_{atoms}: image of the light absorbed by the atoms. c) I_{probe} image of the probe beam without atoms. d) I_{dark} Dark image containing information of the camera noise (Without atoms and probe beam). 124

Figure 50 – Interface of our analysis program, *SrProcess* © : An image of the OD of the Blue atomic cloud is being analyzed and the results are shown in the rightest panel. The op bar offer tools to treat the images, as well as visualization. Traces taken from the oscilloscope are also accessible through those buttons. Automatic graphs generated from the analyzed data can also be displayed. 125

Figure 51 – Interface of our control program, *SrControl* ©: The top bar represents the steady state, or default experimental parameters. The different color boxes are organized in a color scale related to their appearance in the experiment. The vertical direction is given by the time (second column from left to right). The time periods are established then by rows, and an experimental trial begins at period **5**. The sequence for the Blue-MOT is pictured until period **5** and afterward, the Red-MOT sequence is programmed until period **13**. From period **21** until period **30** the absorption imaging sequence is executed in this script. The colored vertical bars represent each of the controlled channels (Analogic and TTLs) already named accordingly to the experimental parameters. At the top right panel, different tools can be called, among those we have: automatic communication with the *SrProcess*, simulation of TOF images, call the *SrCamera* (activates record of images), data recording of the oscilloscope traces, modification of the modulation matrix created in the fast board, calibration of channels, simulation of experimental parameters as well as remote control of extra external devices. 126
Figure 52 – Atomic Forces as a function of the detuning. The dispersive behavior of the radiative pressure can be understood easily when comparing the strength of the effects with the detuning from the resonance. 130

CONTENTS

INTRODUCTION 25

1 COOLING OF STRONTIUM ATOMS TO RECOIL TEMPERATURE 31
1.1 Strontium 31
1.1.1 Vacuum 33
1.2 Cooling of Strontium atoms 34
1.2.1 The blue laser system 36
1.2.1.1 Doppler free spectroscopy 37
1.2.2 2D MOT 38
1.2.2.1 Optimization of the 2D MOT 38
1.2.3 3D-Blue MOT 39
1.2.3.1 Repumpers 40
1.3 Blue MOT characterization 41
1.4 Narrow transition cooling 44
1.4.1 The red laser system 44
1.4.1.1 Injection Lock 46
1.4.2 Ultracold cloud of Sr atoms 49
1.5 Red MOT characterization 51
1.5.0.1 Spectroscopy of the blue transition with the red MOT 51
1.6 Preliminary conclusions 52

2 THE RING CAVITY 55
2.1 Design and setup 55
2.2 The cavity laser spectrometer 57
2.2.1 Controlling the cavity length 58
2.2.2 Phase-locking of the lasers - three locks chain 59
2.3 Characterization of the empty ring cavity 62
2.3.0.1 Finesse 62
2.3.1 Geometry of the ring cavity 64
2.3.1.1 Gain by resonant enhancement of the intracavity field 65
2.3.2 Ring cavity parameters 66
2.4 Trapping atoms in an intracavity optical dipole potential 66
2.4.1 Intensity in the free space focus 67
2.4.2 Dipole trap depth for one-sided pumping 68
2.4.3 Dipole trap depth for double-sided pumping 68
2.4.4 Atoms trapped in the dipolar potential created by the cavity 69

2.4.5 Coils to move the atomic cloud position. . . . 69
2.5 The cavity trap characterization . . . 73
2.5.0.1 The lifetime of the atoms inside of the cavity trap . . . 73
2.5.0.2 Trap vs Frequency . . . 73
2.6 Preliminary conclusions . . . 75

3 OBSERVATION OF BI-STABILITY IN A STRONGLY COUPLED ATOM-CAVITY SYSTEM . . . 77
3.1 Theoretical description . . . 78
3.1.0.1 Weak excitation: . . . 79
3.1.1 Strong excitation, the role of saturation . . . 80
3.1.1.1 Saturation-induced bistability . . . 80
3.1.2 Bistability for our case, the homogeneous clouds . . . 81
3.1.2.1 Critical pump rate on resonance for homogeneous clouds and one-sided pumping . . . 82
3.1.2.2 Hand-waved equation for describing our experimental results . . . 84
3.2 Normal mode splitting Measurement . . . 86
3.2.1 Optical setup and sequence . . . 87
3.2.2 Experimental observations . . . 89
3.2.3 Discussion . . . 89
3.3 Preliminary conclusions . . . 93
3.3.1 Remarks and prospects . . . 94

4 SEARCH FOR BLOCH OSCILLATIONS . . . 95
4.0.1 1D Periodic potential . . . 95
4.1 Bloch dynamics simulation . . . 99
4.2 Experimental search for Bloch oscillations . . . 101
4.3 Preliminary conclusions . . . 105

CONCLUSION . . . 109

REFERENCES . . . 111

ANNEX A – PUBLICATIONS: . . . 119
A.1 Hollow Bessel beams for guiding atoms between vacuum chambers: a proposal and efficiency study . . . 119
A.2 Progress towards a matter wave interferometer for inertial sensing with non-destructive monitoring of Bloch oscillations . . . 119

APPENDIX 121

APPENDIX A – DATA ACQUISITION AND ANALYSIS 123
A.1 Absorption imaging 123
A.2 Experiment: Control and analysis programs 125

APPENDIX B – LIGHT MATTER INTERACTION FORCES . . . 129

INDEX 133

INTRODUCTION

This thesis focuses on the progress in the realization of a matter wave interferometer with an application as a gravimeter. The original proposal is resumed in patent (3), submitted by Philippe Courteille and Romain Bachelard in 2015 to the Brazilian patent agency*.(3) The gravimeter proposed in this patent attempts to measure the gravitational force an atom feels in the presence of a periodic potential. This atom-interferometer will monitor continuously the dynamics of cold atoms inside a pumped ring cavity and in this way extract information from the system in a non-destructive way. The machine, besides operating as a gravimeter, seeks to probe atom-cavity interactions measurables as effects in the light fields escaping the cavity after interacting with the atomic cloud.

Different proposals for the nondestructive monitoring of atom-cavity interactions can be found in the literature. (4–7) The authors demonstrate that when a cold cloud of atoms subject to the action of gravity is also exposed to a co-linear periodic potential they perform Bloch oscillations. Under certain circumstances, in the presence of a ring cavity, the oscillation of the atoms will interact in a non-destructive way with the light mode in the cavity. The light leaking from the ring cavity exhibits periodic features which are synchronized with the oscillation performed by the atoms. This technique for non-destructive real-time monitoring of the dynamics of a matter wave has great potential for improving atom interferometry. The such technique could record Bloch oscillations continuously with a single matter wave. Consequently, the strength of the force can be measured in shorter times, the duty cycle can be reduced, and measurement uncertainties due to the process of generating a new matter wave can be avoided.(8)

Let us take a look at the work done in this area.

Interferometry is based on the principle that a wave can be divided and recombined to give an interference pattern in which the information of some measurable property of the medium is stored. In other words, the phase difference between the interfering waves carries all the information of the measured phenomena. Matter-wave interferometry uses the same principle but applied to ultra-cold atomic matter whose propagation is understood as that of a wave with the De Broglie wavelength ($\lambda_B = h/\sqrt{mk_BT}$), where h is the Planck's constant, m the atomic mass, k_B is the Boltzmann's constant and T is the temperature.

The most common inertial sensors for matter waves are Ramsey-Bordé interferometers.(9) These interferometers also exploit the wave-like behavior of ultra-cold matter,

* Patent status: "Patent or certificate of addition of invention granted[chapter 16.1 patent gazette]" on the date: August 09, 2022

the working principle is explained as follows: the atoms are driven to a superposition state and then subjected to a series of pulses.This sequence of pulses mixes the trajectories of the atoms, and at the end of the interrogation time, an interference signal can be extracted from the ensemble. In the available atomic interferometers, the measurement process is destructive. Normally the atomic cloud is probed with a resonant beam of light to extract information about the momentum distribution using absorption imaging or fluorescence imaging techniques. Unfortunately, the radiation pressure exerted by the light destroys the coherence of the matter wave, as the photonic recoil imparted by the scattered light is randomly distributed in all directions. This holds for techniques measuring the instantaneous density distribution (e.g. absorption imaging), as well as for techniques measuring the velocity distribution, such as recoil-induced resonance spectroscopy (10) or Bragg spectroscopy. (11)

In fact, very few non-destructive techniques have been demonstrated so far. Dispersive imaging (12) allows taking dozens of pictures of a matter-wave before destruction. Electron beam imaging (13) is another example of non-invasive mapping of ultracold atomic density distributions.

The goal of this research project is to demonstrate a possible way around by providing a non-destructive 'live' monitor of the dynamics of the matter-wave.

To implement our non-destructive and continuous monitoring approach to a matter-wave interferometer, two different physical phenomena need consideration (see figure 1): Bloch Oscillations (BO) (14, 15) which will be the phenomena that carries information about the force that gravity exerts on the atoms. The second is the concept of the Collective Atomic Recoil Laser (16–19) (CARL) that will synchronize a probe light field injected into the cavity with the BO dynamics that the atoms suffer. Let us analyze these concepts with more detail:

Bloch Oscillations (BO) are a quantum effect that consists of oscillatory movement for a coherent wave packet inside a periodic potential, and under the action of a constant force, the oscillation frequency is proportional to the applied force and the lattice constant. BOs were just recently observed with cold atoms at temperatures below the limit of the photonic recoil(20) and in matter-waves. (21, 22) In these experiments, the atoms are placed within a stationary wave of light and subjected to an external force. When the constant force acting on the atoms is given by the gravitational field, we may have an accurate measure of the gravitational acceleration upon monitoring the oscillations period.

Collective atomic recoil laser or CARL, is an effect that converts kinetic energy into coherent radiation. When atoms in a **ring cavity** are placed inside of a red-detuned dipolar potential created by a moving standing wave, they will experience a push towards the maxima and feel an accelerating force. This effect can be described as a backscattering

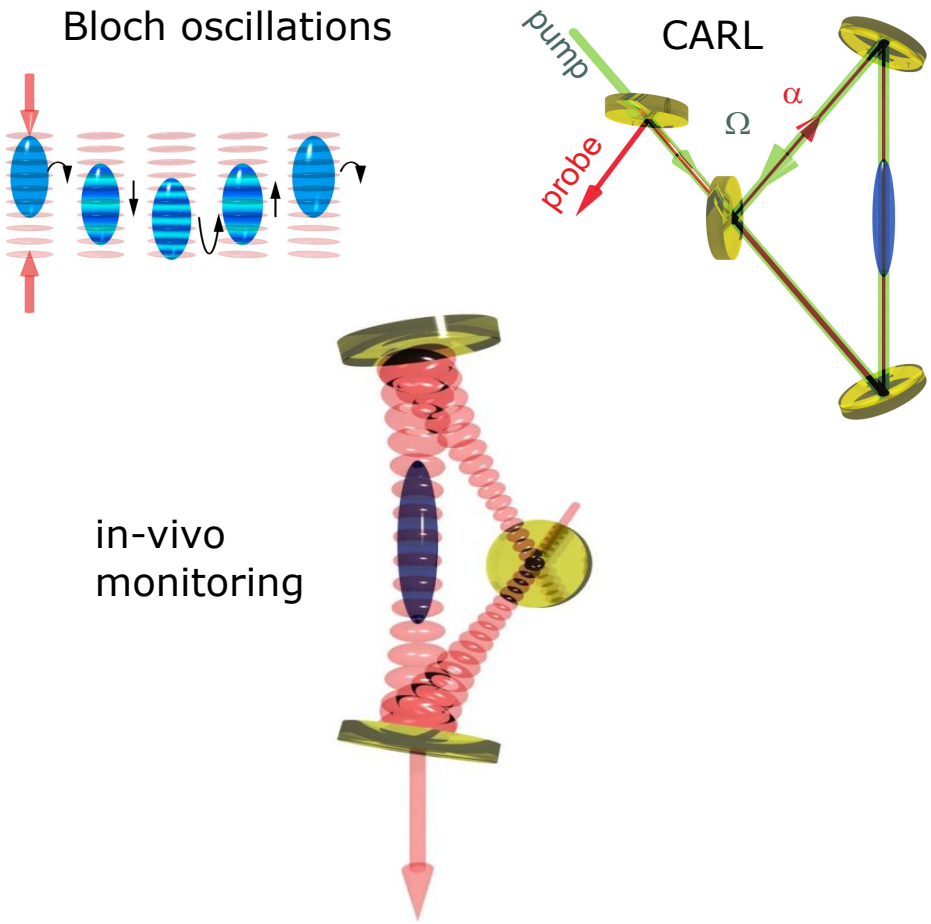

Figure 1 – Bloch oscillations in a ring cavity as a non-destructive method to measure matter-wave interferometry.

Source: Adapted from SAMOYLOVA *et al.* (7)

of photons from the co-propagating into the contra-propagating mode. The backscattering will create a stronger standing wave that will (recursively) scatter more photons into the probe mode. This redistribution of energy amplifies the contrast of the standing wave leading to an exponential gain in the counter-propagating mode (self-amplification), displaying a behavior very similar to those of lasers.

The use of optical cavities to steer the scattered light into a single cavity mode makes use of the very large Purcell factor of resonant cavities. Now, the scattering process becomes coherent, the mechanical impact of the incident light becomes predictable and can be taken into account, while heating can be avoided. The dynamics have been experimentally demonstrated in Refs. (23, 24) using a ring cavity. In those experiments, when one of two counter-propagating cavity modes was pumped by a sufficiently far-detuned laser, a matter-wave confined in the mode volume responded by scattering light exclusively into the backward direction. The time evolution of the recorded backscattered light contained all information on the condensate's trajectory, while the purely dispersive interaction with the cavity mode prevented decoherence of the matter-wave.

The popularity of ultra-cold strontium (25–29) in matter-wave interferometry (30–33) has various reasons. The existence of a strong dipole-allowed transition (linewidth $\Gamma_{461}/2\pi = 30.5$ MHz) and a narrow inter-combination line (linewidth $\Gamma_{689}/2\pi = 7.6$ kHz) allows rapid optical cooling close to the recoil temperature. The electronic ground state $^1S_0$ of the bosonic isotopes has no magnetic moment, which makes it insensitive to stray magnetic fields. The abundant ^{88}Sr isotope exhibits a small s-wave scattering length ($a_s = -2a_B$, with a_B the Bohr radius), such that inter-atomic collisions can be neglected. It is thus not surprising that very stable Bloch oscillations induced by gravity on ultra-cold ^{88}Sr trapped in a vertical standing wave could be observed (22) and applied to gravity measurement. Finally, as we will show in this thesis, the narrowness of the inter-combination line, although requiring stable laser sources to drive it, facilitates cavity-assisted spectroscopy on this transition. Combining the aforementioned advantages of ^{88}Sr atoms with the coherent interaction between the atoms and the counter-propagating modes of a ring cavity will open up the path to a non-destructive, continuous measurement of gravity (8) with state-of-the-art precision, as already proposed in the literature. (6,7,34).

BO is not the only quantum effect, we are interested to measure in our experiment. Cavity-mediated interactions between atoms also provide a promising route to generate non-trivial interatomic correlations leading to phenomena such as spin-squeezing (35–39, 39–43), superradiant lasing (44–51), or quantum state magnification (52, 53), which are of utmost interest for metrological applications.

One important request is that the rate of spontaneous emission Γ is small, leaving cavity decay occurring at a rate κ as the only available decay channel. In this limit, known as the 'bad cavity' regime, the photon statistics become more robust (54–58) and correlations more stable.

A second requirement is high collective cooperativity, which guarantees that light emitted from one photon may be reabsorbed by another one and thus information be shared between atoms.

A third requirement is non-linear system dynamics leading to bistability. For the optical mode, the bistability can manifest as two stable states of transmission, whose realization depend on the history of the system. The bistability can originate in different features of the system. For example, in (59–62) it is caused by the multilevel structure of the ground state (63, 64). Bistability can also be induced by saturation (65–67). and is therefore the region where to expect quantum correlations (46, 54).

The nonlinearity of a system critically depends on the coupling strength between atoms and optical modes selected by the cavity and can be quantified by the observation of normal-mode splitting (68–72). For the case of saturation Gripp *et al.* (65) predicted the existence of an additional mode besides the two normal modes, which should emerge when the cavity and the pump laser frequencies are tuned to resonance. In practice, this

mode is heavily suppressed because of absorption. A solution to the problem can be the use of a narrow atomic resonance.

Gothe *et al.*. (67) studied ytterbium atoms coupled to a cavity via a narrow transition. However, the atomic decay rate was still twice the cavity decay rate so that, on resonance, spontaneous emission remained the main decay channel. In order to avoid spontaneous emission leading to heating and trap loss they coupled the atoms dispersively to their cavity, so that the interesting features appear far from the atomic resonance.

In this work, we choose experimental parameters, i.e. a narrow atomic resonance and a 'bad cavity', such that the atoms couple resonantly to the cavity, but dispersively to the pump light. This regime allows us to excite and experimentally study the resonant normal mode, as a novel manifestation of saturation-induced bistability. Our atomic transition is the $\Gamma/2\pi = 7.6\,\mathrm{kHz}$ narrow intercombination transition ${}^1S_0 \leftrightarrow {}^3P_1$ in atomic strontium, interacting with a 'bad' ring cavity, whose amplitude decay width is $\kappa/2\pi = 3.9\,\mathrm{MHz}$. The transition has a low enough saturation intensity to be saturated with single photons in our ring cavity, whose atom-field coupling constant is $g/2\pi = 9.1\,\mathrm{kHz}$.

This thesis presents a novel setup for controlling the coherent interaction between the internal and external degrees of freedom of cold ${}^{88}\mathrm{Sr}$ atoms and laser light stored in a mode of an optical ring cavity,(8).

Chapter 1 will focus on the setup and characterization of the system to achieve ultra-cold temperatures with Strontium atoms. In chapter 2 the focus is the characterization of our ring cavity and the creation of the periodic potential. The effective realization of a dipolar trap for atoms using a narrow transition was demonstrated. Chapter 3 confirms the atom-cavity interactions via experiments of normal mode splitting. A peculiar new signature that the atoms create in the ring cavities spectrum's is preliminary studied and observed for the first time in this thesis. Chapter 4 focuses on the unsuccessful, quest for Bloch oscillations. A resume of our principal results as well as future perspectives of the experiment is summarized in the conclusion's chapter 4.3.

1 COOLING OF STRONTIUM ATOMS TO RECOIL TEMPERATURE

The present chapter will explain the accomplishment of the first part of the matter-wave interferometer for Bloch Oscillations. The cold cloud of atoms will be used as a playground to perform the oscillations.

In our experiment atoms of Strontium are cooled down to temperatures of 800 nK. The process to reach these temperatures was achieved for the first time in our laboratory (**Sr2**) in the course of this thesis.

1.1 Strontium

A particularly versatile atomic species for applications in quantum sensors is Strontium, specifically ^{88}Sr the most abundant isotope (82.88% of natural abundance (2)). The ground-state electronic configuration of Sr has an outer s-shell filled with two valence electrons, this pairing explains one of its best attributes, $I = 0$ for the nuclear spin momentum. The ground state insensitivity with the magnetic field, of Strontium, makes it a perfect candidate for atomic sensing devices that are not affected by stray magnetic fields.

Figure (2) shows the Grotrian diagram of Strontium with some of the relevant optical transitions and in parenthesis its linewidth. The linewidth is related to the lifetime of the upper-state, therefore the lifetime of a state can be calculated by $\tau = 1/\Gamma$. The linewidth is also a reference (experimentally) for the maximum instability that our laser needs to have in order to excite this transition.

The excited states can happen under the anti-parallel alignment of the spins, also known as singlet states (S=0). As an example, we can name the main cooling transition at 461 nm, also known as a broad transition because of the $\Gamma \approx 2\pi \times 32$ MHz characteristic linewidth. This transition represents a dipole coupling between the energy levels $(5s^2)^1S_0$ and $(5s^2)^1P_1$. Parallel alignment of the spins or triplet states (S=1) also occurs for Strontium and we find fine and broad cycling transitions. It is nice to notice that most of those wavelengths are in the VIS spectrum, which makes it easier to manipulate in the laboratory. In our setup, we use 679 nm and 707 nm for the re-pumping of the atoms.

A peculiarity of Alkali atoms is that the singlet and triplet states mix through inter-combination transitions. For atoms heavier than $Z > 30$ spin-orbital interactions becomes larger than spin-spin or orbital-orbital interactions (73), giving rise to finite lifetimes through higher order process like E1, E2, M1 and M2.(2) *. The mixing of states with the same total angular momentum J and different spin S produces a manifold of

* Electric dipole (E1), Magnetic dipole (M1), Electric quadrupole (E2), Magnetic quadrupole (M2).

three inter-combination lines in Strontium that can be seen in red in fig 2.

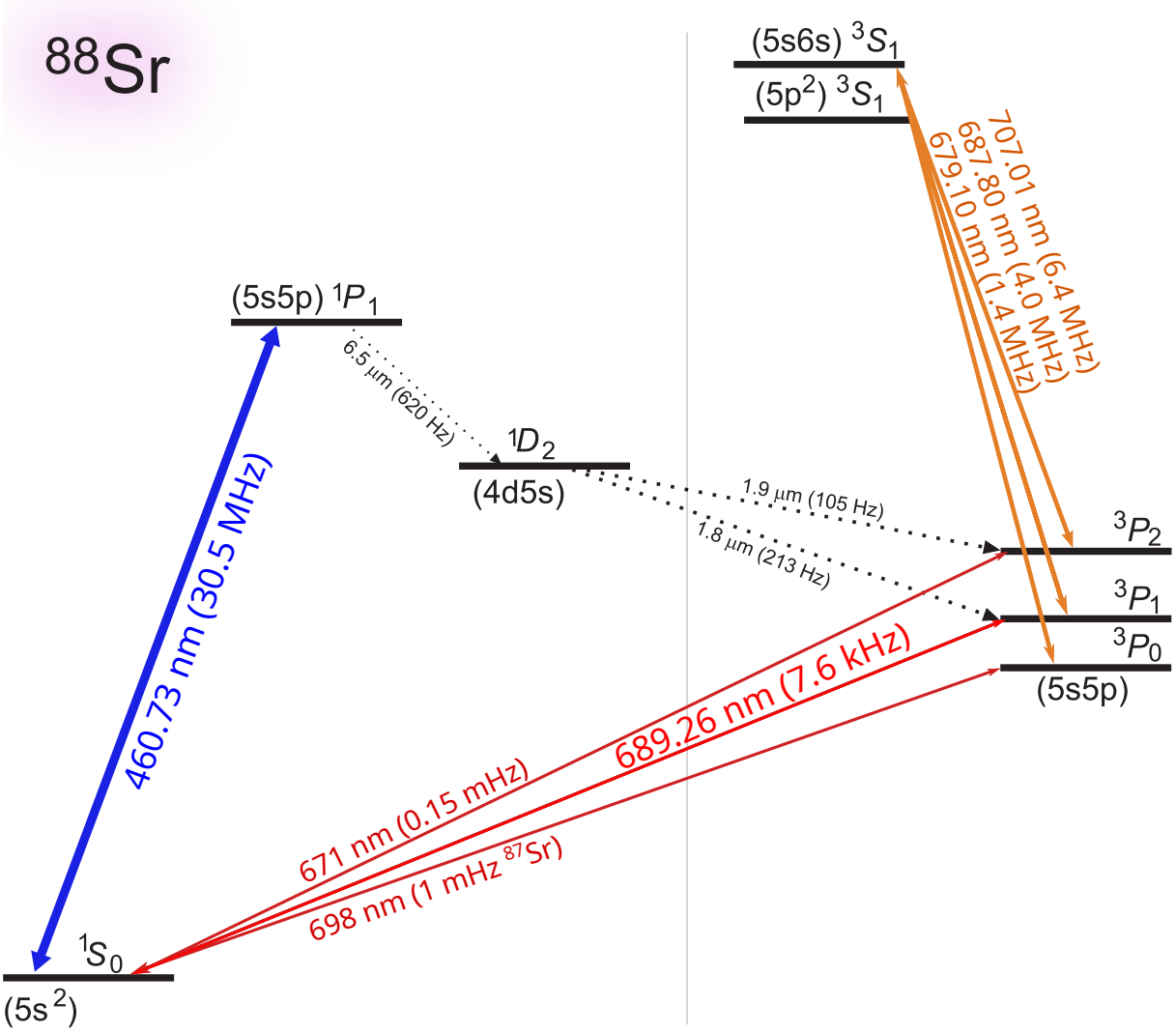

Figure 2 – Level scheme of strontium: wavelengths and linewidth (in parentheses). Values references: SANSONETTI*et al.*(1) and STELLMER(2)

. Source: By the author.

$1S_0 \leftrightarrow 3P_1$ This transition is also known as the narrow transition in Sr. The lifetime is of about 21μs ($\Gamma/(2\pi) \approx 7.6$ kHz). We perform a second cooling process using laser light at this wavelength 689 nm, therefore more details on this meta-stable state will be explained further on in this chapter.

$1S_0 \leftrightarrow 3P_2$ and $1S_0 \leftrightarrow 3P_0$ these transitions have decay times of several seconds and therefore are used as atoms reservoirs in our experiment. The wavelength of those transitions is 671 nm and 698 nm respectively. They are not relevant for the development of this work, nonetheless, it is interesting to notice that the recycling of atoms accumulated there is made via the wavelengths 707 nm and 679 nm that couple the transitions $3P_2$ and $3P_0 \leftrightarrow 3(5s6s)S_1$. Notice how several of the aforementioned transitions are separated a

few nanometers of each other, which also makes strontium even more versatile. In practice, a commercial laser can be bought for a specific wavelength (AR-coated diodes), that can be tuned for ±10 nm.

Besides the aptitude of its electronic level system for efficient optical cooling and the existence of a hyper-fine inter-combination transition in the optical regime. Is also interesting to note the availability of several bosonic and fermionic isotopes, some of which exhibit very weak inter-atomic interactions (the scattering length for ^{88}Sr is only -2a$_B$). Therefore, line shifts due to collisions are negligible.

The lack of collisions of ^{88}Sr also makes it impossible to Bose-condensate it using only this isotope (Strontium condensates can be achieved with sympathetic cooling (74)). For the demonstration of matter-wave interferometry, the use of condensates is unnecessary since ultra-cold strontium at sub-Doppler temperatures has a matter-wave behavior enough for the observation we pursue. At 800 nK the de Broglie wavelength ($\lambda_{dB} = h/p = h/\sqrt{k_B T m}$) is of $\approx 0.5\mu$m.

1.1.1 Vacuum

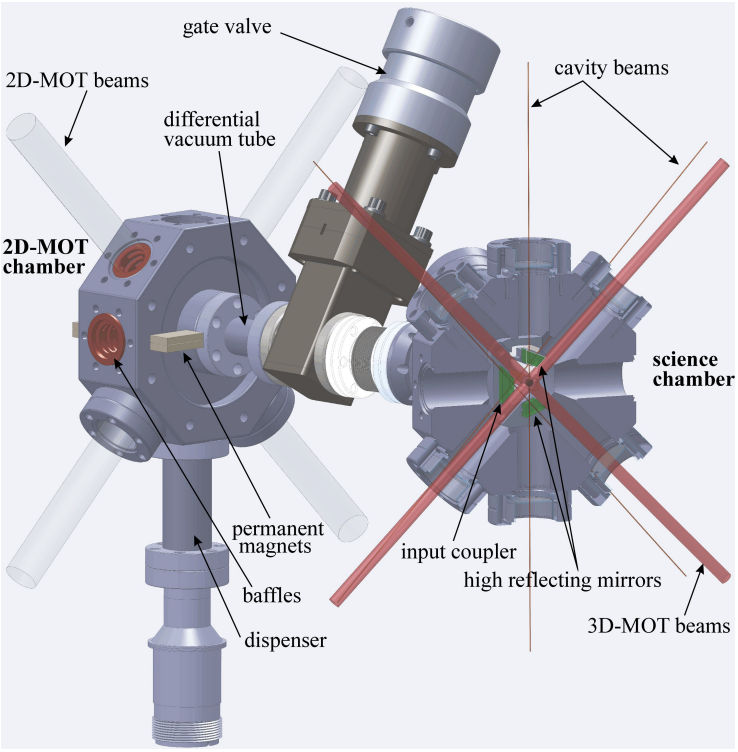

Figure 3 – Technical drawing of the 2D-MOT and the science chamber. Note the ring cavity mounted inside the science chamber.

Source: By the author.

Fig. 3 shows the layout of our experiment. The whole vacuum chamber setup fits on top of a 50 by 50 cm base plate. It consists of two separate vacuum chambers linked by a 2 cm long differential vacuum tube with 2 mm inner diameter.

The lifetime of a cloud of trapped atoms is inversely proportional to the pressure of the chamber, therefore an ultra-high vacuum (UHV) is necessary to ensure fewer collisions with the background atoms. The presence of residual background gases may knock the atoms out of the trap. (75)

In order to reach UHV pressure a standard cleaning and sealing process is followed [†]. The late stage of the process is called baking. It consists in covering the chamber with electric heating tapes distributed uniformly. The rise in temperature creates a degassing of the products that stick to the walls of the chambers, this gas is simultaneously extracted via a turbo or ionic pumps. Baking time and temperature are inversely proportional to the final pressure achieved. In our setup baking was performed for 21 days at 120^oC.

In the preparation chamber, the pressure is about $9 \cdot 10^{-8}$ Torr while in the science chamber the value is $1.5 \cdot 10^{-9}$ Torr. the difference comes from the fact that in the preparation chamber strontium atoms are ejected from a heated dispenser to be pre-cooled in a 2D-MOT. The heat of the dispenser increases the pressure of the residual gas according to the ideal gas law. In order to maintain the vacuum difference these two are connected through a 20 mm long and 2 mm wide differential pumping tube that ensures a lower pressure in the science chamber.

1.2 Cooling of Strontium atoms

In order to reach ultracold temperatures with strontium we will perform a two stages cooling process. As mentioned before the two main transitions that will be used are the broad and fine transitions at 461 nm ($\Gamma/(2\pi) = 30.5$ MHz) and 689 nm ($\gamma/(2\pi) = 7.6$ kHz) respectively.

Each stage asks for different experimental details, therefore the description of the cooling processes will be done separately. Nonetheless, both cooling processes rely on the same principle, which is the use of laser light close to the resonant to slow down the atoms together with the magnetic field, also known as Magnetic Optical Trap (MOT).

$$F = -\hbar k \Gamma \frac{\Omega^2}{4\Delta^2 + 2\Omega^2 + \Gamma^2} \tag{1.1}$$

Equation 1.1 describes the Force an atom feels when in the presence of a light field tuned close to resonance. A resumed deduction of the forces involved in the light atom interaction can be found in Annex B, for further details try references (76,77). With $\Omega^2 \propto I$ the intensity of the laser beam. The term Δ represents the frequency difference between the atomic resonance frequency and the laser light frequency ($\Delta = \omega_{atom} - \omega_{laser}$), and it is normally referred to as detuning. The radiation pressure force is dissipative. It can be interpreted as resulting from absorption processes followed by spontaneous emission. It is

[†] UHV - Wikipedia

important to notice that Δ does not depend only on the laser-tuned frequency, but it can be modified (from the atom's point of view) for the atom's velocity distribution (Doppler effect) and the presence of fields that can change the resonance (ex: Zeeman shift, stark shift, etc). In that way, a moving atom in direction $\mathbf{i}$ in the presence of a magnetic field will see a light field detuning of:

$$\Delta_{eff} = \Delta_i \pm k.\mathbf{v_i} \pm i\partial_i\omega_{Zeeman} \tag{1.2}$$

The reason for the necessity of two cooling stages is then explained when we look at the Doppler Temperature which is the lowest velocity distribution that can be achieved by means of radiative pressure and is limited by the linewidth of the transition (Γ).

$$k_B T_D = \frac{\hbar}{2}\Gamma \tag{1.3}$$

Equation 1.3 gave us a Doppler temperature of $T_{D-461} = 720\mu K$ for the blue transition and $T_{D-689} = 180nK$ for the red transition. That means that for ideal experimental conditions the temperatures can reach the nK scale.

On the other hand, we have to take into account another effect that light exerts on the atoms. Notice that from equation 1.3 the typical velocity of the atoms at this temperature is given by: $v = \sqrt{k_B T_D/m} = \sqrt{\hbar\Gamma/2m}$. This is the velocity limit that enables us to consider the total light force as a friction force. The friction by its time is exerted by photons, which carry one unit of momentum $p = \hbar k$, with $k = 2\pi/\lambda$ the wave-vector of the incident radiation, this quantity momentum is transferred to the atom during an absorption or emission process. When comparing this with the velocity limit condition (for two photons interaction), we found:

$$kv \ll \Gamma \rightarrow \frac{\hbar k^2}{2m} \ll \Gamma \tag{1.4}$$

That is, the light exerts a recoil on the atoms, with ω_{rec} defined in 1.4. Therefore, if we use light to slow down the atoms the lowest velocities are limited by the momentum imparted by two photons. In other words, the absorption and consequently spontaneous emission of one photon, equivalent to the action of two photons, is the recoil experienced by the atom. And we can now define an analogous temperature

$$k_B T_{rec} = \frac{\hbar^2 k^2}{2m} \tag{1.5}$$

analogously, equation 1.5 results in temperatures of $T_{rec-461} = 1.02\mu K$ for the blue transition and $T_{rec-689} = 460nK$ for the red transition. Comparing these values with the ones obtained from equation 1.3 (T_D) we see that the lower temperature limit for the blue transition is given by the Doppler broadening, meanwhile, for the red transition, the temperatures are limited by the recoil energy imparted by the light.

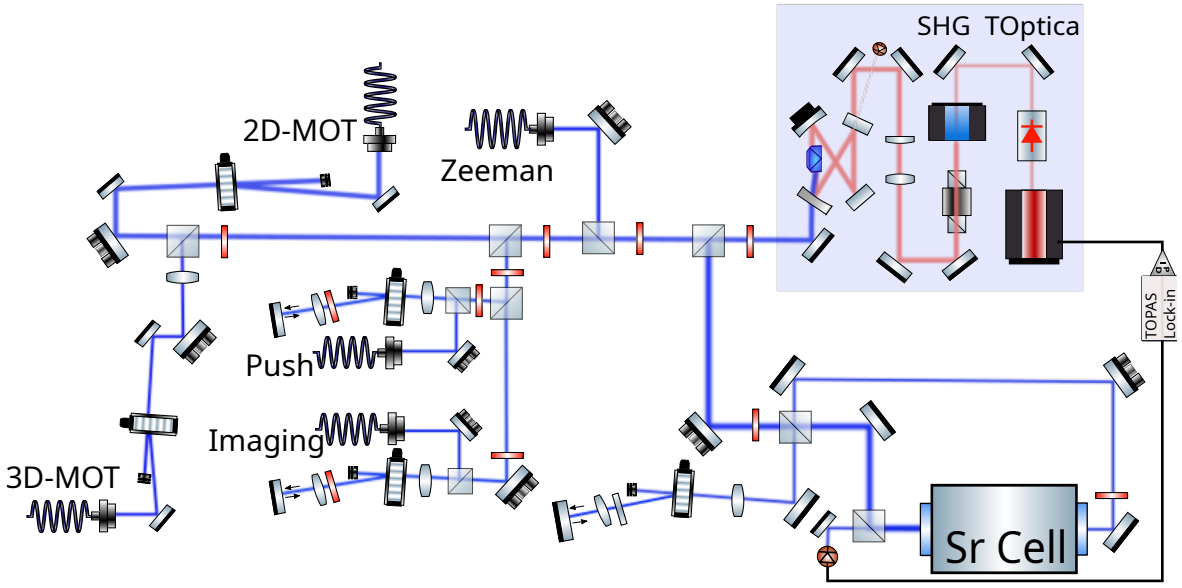

Figure 4 – Scheme of the distribution of the Blue light produced by the SHG. The Doppler-free spectroscopy technique is pictured at the bottom right. After frequency-shifting the laser light with the help of AOMs, the wavelengths are sent to the experiment via optical fibers.

Source: By the author.

1.2.1 The blue laser system

To generate the blue laser light we use a commercial frequency-doubled tapered amplified diode laser (Toptica, DLC TA-SHG pro). We tune the master laser to 922 nm, and after amplification, it provides ≈2 W of infrared light power, that is ultimately frequency doubled in a bow-tie ring cavity delivering power of ≈ 700 mW at 461 nm with a linewidth of Blue ≈ 0.5 MHz. The blue laser path is shown in figure 4, where Acoustical Optic Modulators[‡] (AOMs) are used to shift the frequency of the light as well as to control the amplitude of the light that passes through them. Polarizing beam splitters (PBS) are used to filter the polarization and to distribute the power when in front of a half-waveplate. Waveplates shift the polarization direction of linearly polarized light ($\lambda/2$) or convert it to circularly polarized light ($\lambda/4$) and vice-versa. Optical fibers are used to deliver the laser frequencies, in a Gaussian mode with low divergence, to the experiment. The frequency of the laser is stabilized at 140 MHz to the red of the atomic transition with a technique called Doppler-free spectroscopy.

[‡] AOMs are electronic devices that allow us to change the frequency of the light that transit through them in an amount determined by the radio frequency used to drive the device. The amplitude of the modulation also translates into an amplitude modulation of the light, which allows us to control in a versatile way the experimental parameter. The response speed of those devices is given by the speed of sound on the crystal, this translates into switch and modulations on the order of 1 MHz

1.2.1.1 Doppler free spectroscopy

This technique allows for the stabilization of the laser frequency while avoiding the broadening of the linewidth due to the velocity distribution of the atoms. If a strong resonant laser beam interacts with the gas of Strontium, the light will be absorbed if the atom changes its state from a lower to a higher energy level, and since the gas has a distribution of velocities, the absorption spectrum will be Doppler and saturation broadened. If the excited atoms are exposed to a counter-propagating beam, the light emitted when the atom falls back into a lower energy state will be subtracted from the absorption spectrum. The laser frequency is scanned and when the transmitted light is analyzed by a photo-diode, this shows a frequency-dependent intensity spectrum. Since light is absorbed in the resonance frequency, less light is transmitted through the cell. The transmission spectrum is used to lock the laser wavelength.

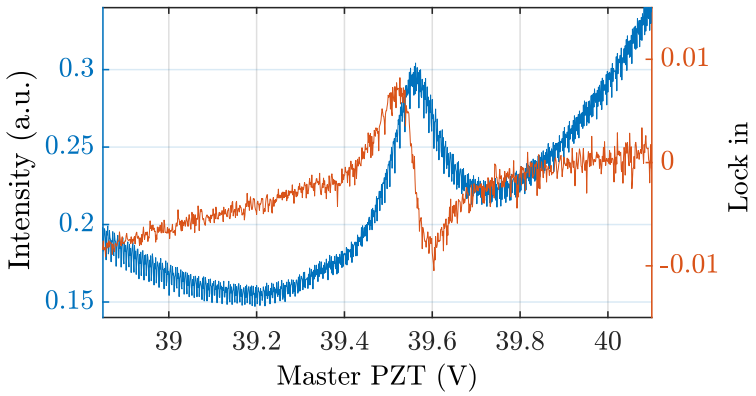

Figure 5 – Lock-in spectroscopy signals: the blue curve is the signal provided by the photo-detector of the probe beam as a function of the laser frequency (The scan is being performed in the piezo of the master laser), the modulation of the Lock-in is appreciated all across the signal. The orange curve is the error signal created by the demodulation of the Blue curve.

Source: By the author.

We lock using the top-of-fringe lock, which means that we lock in the top of the absorption peak of the absorption spectrum. In our experiment, the modulation of the lock is of $\approx$ 40kHz, and it is done by means of an AOM in the probe beam. The signal is then demodulated using a lock-in integrated into the control software of our laser (DLC pro Lock), and the correction is sent back to the laser and fed to the piezo of the master laser (see figure 4). Figure (5) shows in blue a typical spectroscopy spectrum with the laser piezo scanned by 200 mV which is translated to a scan of several MHz, in red the error function created with demodulation. The lock feedback is of the order of 100 kHz, and the laser stability after locking is of $\approx$ 500 kHz, and after doubling we have 250 kHz. When this is compared with the linewidth of the blue transition we can be sure that our laser is good enough to perform the cooling process, as well as question the transition.

It is also possible to appreciate in figure 5 the broadening due to power and velocity distributions, that is the blue curve on which the spectroscopy signal sits. Also, at the left of the Sr^{88}absorption visible at 39.35 V it is an appreciable tiny curve of absorption, this is due to the absorption of isotope Sr^{86} atoms that are also present in our hot vapor cell.

After the stabilization, all the frequencies necessaries to manipulate the atoms can be achieved with AOMs. The push and the imaging beams (see figure 4) are resonant with the atomic transition. The cooling lights of the Zeeman beam, 2D-MOT, and 3D-MOT have -140,-70, and -40 MHz of detuning with the atomic transition respectively. More details of our blue setup can be found in the master thesis of Armijos M.(78)

1.2.2 2D MOT

A Magneto Optical Trap (MOT) is a widely used technique for trapping atoms using laser light and magnetic field since first realized (1987).(79) For a detailed explanation of the functioning of the cooling processes involved in a MOT a variety of texts and materials is available online.(76, 77, 80)

The 2D-MOT is loaded from a strontium dispenser (AlfaVakuo e.U.) that runs at a current of 6.6 A. We have observed that, although there is no direct path from the dispenser to the vacuum viewports and although the strontium atoms have the tendency to stick to the walls that they encounter, they eventually deposit on the viewports, coating them with an opaque layer. In order to minimize this problem, baffles have been mounted around the dispenser and the viewports of the 2D-MOT chamber obstructing simple atomic trajectories (such as single reflections from the walls). The baffles are simply stacks of concentric copper rings with an outer diameter made to fit into the CF16 ports of the vacuum chamber and an inner diameter leaving a 1 cm clear aperture adapted to the size of the 2D-MOT beams. No coating of the viewports has been observed since this measure, which was implemented five years ago.

The 2D-MOT is operated with permanent magnets arranged such that the symmetry axis is magnetic field-free.(81) The retro-reflected laser beams operating the 2D-MOT have 19 mW each with waists of 0.7 cm and are tuned 30 MHz below the strong blue cooling transition $(5s^2)^1S_0 \leftrightarrow (5s5p)^1P_1$ at 461 nm (see Fig. 2).

1.2.2.1 Optimization of the 2D MOT

Additional single-path laser beams with 19 mW power and tuned 134 MHz below resonance are injected under 55° to the atom beam ejected from the dispenser. These beams, which we will call 'Zeeman beams' are meant to decelerate fast atoms and to increase the loading efficiency of the 2D-MOT.(82) Further on in this chapter a charac-

terization of the loading efficiency of our Blue MOT as a function of the Zeeman beams intensity will be shown.

The atoms captured in the 2D-MOT create a thin tube structure, which afterward is illuminated by a resonant light beam perpendicular to it, the so-called 'push beam', which has an intensity of $0.8I_{sat,461}$, where $I_{sat,461} = 40.6$ mW/cm^2 is the saturation intensity of the cooling transition. The push beam accelerates the atoms towards the science chamber, where they are recaptured by a standard 3D magneto-optical trap called 'blue MOT'.

We studied by numerical simulations a scheme for guiding cold atoms through a hollow Bessel beam generated by a single axicon and a lens.(83) The proposed method would provide an enhancement of the loading efficiency of the atoms transferred from a 2D magneto-optical trap toward the science chamber. The implementation of this proposal in our experiment is delayed for multiple reasons, but principally we didn't have enough power on the Blue laser during the first 3 years of the development of this thesis. Further details on this work can be found in reference (83) or Appendix A.1.

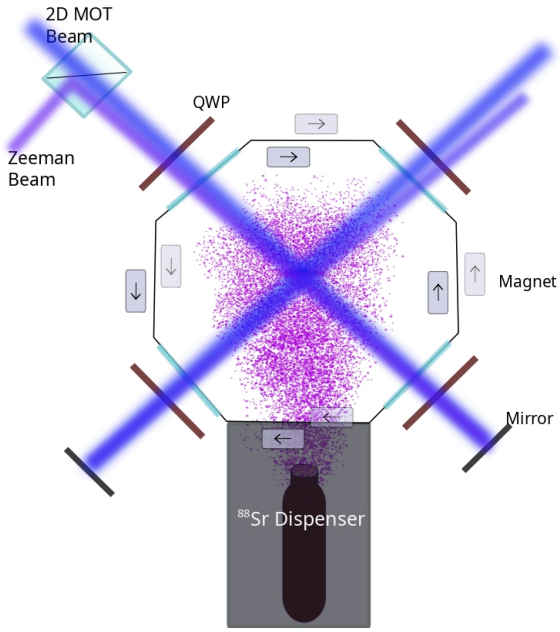

Figure 6 – 2D-MOT scheme including the non-colinear input of the extra slower beams, also called Zeeman beams

Source: By the author.

1.2.3 3D-Blue MOT

The blue MOT is realized with three pairs of counter-propagating laser beams, each beam with 3.5 mW power tuned 32 MHz below the blue cooling transition. The magnetic field for the blue MOT is created by a pair of coils in anti-Helmholtz configuration, being

zero at the center of the coils and having a gradient of 65 G/cm along the coils' axial direction.

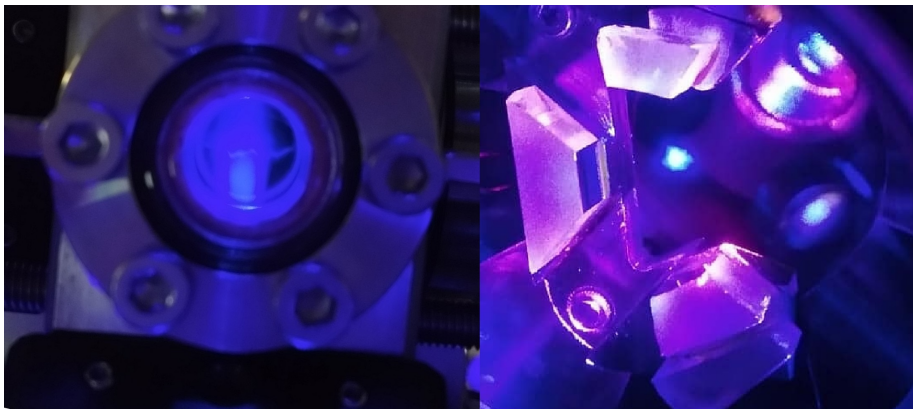

Figure 7 – Photos of:(right) side view of the 2D MOT while the push beam is on. Notice the tail of atoms being pushed from left to right of the center of the window. (left) Top view of the 3D Blue-MOT and the cavity.

Source: By the author.

1.2.3.1 Repumpers

Additionally, 'repumping' lasers are required to recycle the population of atoms eventually pumped into meta-stable states. One of them is the long-lived $(5s5p)^3P_2$ (see Fig. 2). We deplete this state by driving the transition at $\lambda = 707$ nm ($\gamma_{707}/2\pi = 6.4$MHz).(84, 85) We perform this by using about 9 mW of laser power shined to the cloud uninterruptedly through the same path of the 3D-MOT beams. This state can also be depopulated by a laser at $\lambda = 403$ nm, which is also available in our setup, but the results related to this thesis are not relevant. However, both transitions can lead to non-negligible decay into another meta-stable state $(5s5p)^3P_0$, from which the atoms are recycled by driving a second repumping transition at 679 nm (all lasers are Toptica, DLC pro). For this state, our laser delivers around 4 mW of power, which translate to a broadening of the transition of several γ ($\gamma_{679}/2\pi = 1.4$MHz). Ensuring stable recycling of the atoms even if the frequency of our laser drift ($\Gamma_{broadened}/\Gamma_{nat} < 1$) for the measuring time. The laser frequency drifts on about $\approx$ 500 kHz/h, stable enough to be used in the experiment without being locked to a reference. Nonetheless, we monitor their wavelength with a wave-meter (High-Finesse - Angstrom WS Ultimate 30t) and we found that the drifts of the lasers can be in expressed as $\Delta\nu_{707} = 0.3\gamma_{707}/day$ and $\Delta\nu_{679} = 5\gamma_{679}/day$, in counterpart we adjust the frequency manually when necessary. Among the future projects of the experiment, we plan to build a lock system for the re-pumpers.

More details on the characterization and setup of our Blue MOT can be found in the dissertation of Michelle Armijos.(78) Detailed explanations of the experimental setup and implementations are listed there.

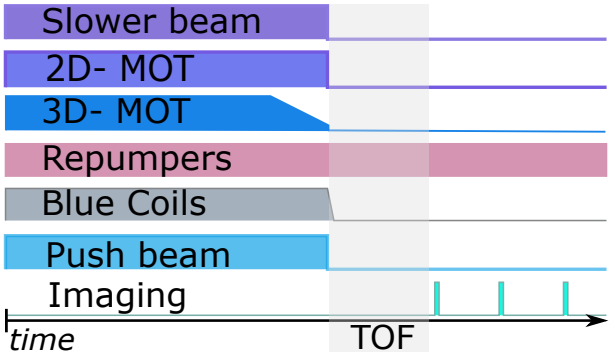

Figure 8 – Time sequence for the production of a Blue MOT and subsequent imaging of the cloud. For the production of a red MOT or for cavity trapping we add sequences before the imaging stage. The main features of each controlled parameter are pictured, nonetheless, is important to notice that the time is not at scale since for loading the Blue-MOT the time is 1200 ms while the power ramp at the last stage occurs in 6 ms. Or analogously the Magnetic field switch-off takes 0.16 ms, and the probe pulses have a duration of 20 ns.

Source: By the author.

The joint action of the repumpers efficiently pumps the population from the metastable states to the $^3P_1$ state, from which the atoms finally decay into the ground state.

As a final step to achieve the lowest temperatures a ramp in the intensity of the beams is performed to reduce saturation broadening of the transition (See figure 9). In that way, we ensure a cloud of cold atoms (Blue-MOT) with temperatures close to the Doppler limit of the blue transition that is of the order of some few mK. In figure 7, a photo of our 'Blue MOT' can be appreciated, the purple visual effect comes from the scattered light in the science chamber when the red light of the re-pumpers is shined in.

1.3 Blue MOT characterization

After optimization and fine-tuning of the parameters (detuning, intensity, alignment, field amplitude, optimal times, etc) on our experiment we realize an optimized Blue-MOT. The characterization of the trapped cloud is performed by means of the parameters extracted via absorption imaging using the TOF technique (see AppendixA). The steady-state atom number of the blue MOT as a function of the intensity of the additional slower beams named in section 1.2.2.1 is presented in Fig. 9(a). The growth of the atom number as a function of the intensity of the beams suggests that this by-chromatic scheme provides further trapping. Figure 9b) shows a characterization performed for the final intensity of the power ramp performed at the last stage of the Blue-MOT. We found, as predicted by theory, that lower final intensity ensures lower (Doppler) final temperatures of the cloud, nonetheless, the atom number in the trap diminishes as the trap becomes shallow and the atoms escape. This behavior is also understood when we look at the size of the cloud (σ_x or σ_y) (See yellow traces at 9b) measured by absorption imaging.

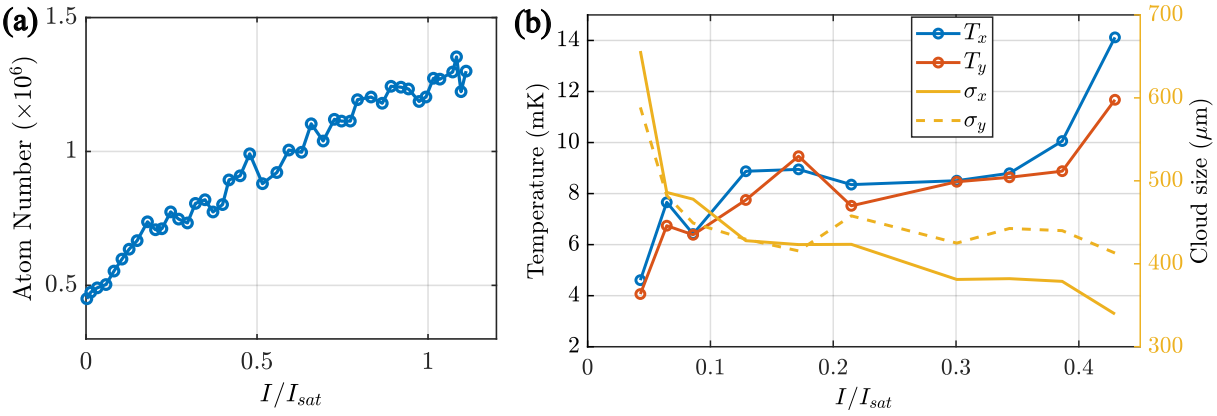

Figure 9 – (a) Number of atoms in the blue MOT as a function of the intensity of the slower beams of the 2D-MOT. (b) Blue-MOT temperature (Each point represents a TOF sequence) as a function of the final intensity of the 3D-BlueMOT beam intensity. The change experienced by the cloud's size is also shown in contrast to the temperature behavior.

Source: By the author.

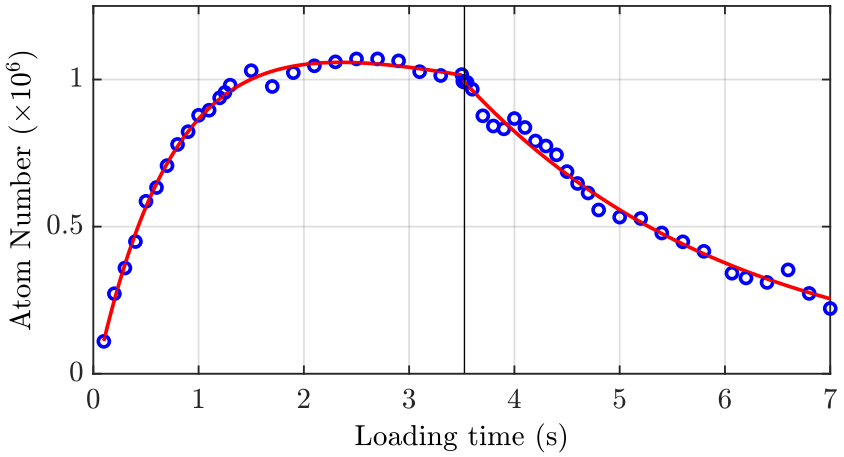

Figure 10 – Blue MOT loading and decay after switching off the 2D-MOT push beam as a function of time. The red curve is an exponential fit to the experimental data from which the time constants are extracted.

Source: By the author.

Since the trap becomes shallow the atoms spread and the fit on the distribution widens. Finally, we decided to perform the ramp until values of around $I_{3D-Blue}/I_{sat} \approx 0.1$ to ensure a bigger atom number and a lower spread of the cloud.

We currently trap around $N = 10^6$ atoms in the blue MOT (see Fig10). While this atom number is relatively low in comparison to other experiments, and probably due to conservative handling of the Sr-dispenser ($I = 6.5$A), it is plenty for the purpose of the intended experiments. The final temperature is about $T \approx 4$ mK. The left side of Fig. 10(a) shows the number of atoms accumulating in the blue MOT via absorption imaging as a function of time, with the light beams of the 2D-MOT turned on at $t = 0$

and off at $t = 3.5$ s, illustrating the loading of the cloud. After 3.5 s the light beams are turned off but the Magnetic trap remains on, and the decay of the blue MOT is measured. By means of fitting an exponential function to the experimental data, the red curve in Fig.10, we measure a loading time of 0.66 s and a decay time of 2.47 s.

1.4 Narrow transition cooling

The temperature of the atoms cooled in the blue MOT is Doppler-limited by the linewidth of the transition to theoretically $T_D = \hbar\Gamma_{461}/2k_B \approx 0.72$ mK, with $\hbar$ the reduced Planck constant and k_B the Boltzmann constant. In practice, we reach $T_{blue} \approx 4$ mK. Lower temperatures could be achieved but the atom number would be way lower.

In order to reach lower temperatures, we cool the atoms in a second stage, called 'red MOT', operated on the narrow inter-combination line, the ${}^1S_0 \leftrightarrow {}^3P_1$ at $\lambda_{689} = 689$ nm, which is sufficiently narrow so that the Doppler-limit is below the recoil limit at $T_{rec} = \hbar^2k^2/2k_Bm \approx 460$ nK, with $k = 2\pi/\lambda_{689}$ the wave-number of the resonant light and m the mass of a ^{88}Sr atom.

1.4.1 The red laser system

The red light necessary to cool the atoms on the narrow transition (see Fig. 2) of Strontium must fulfill three main conditions:

1. The stability of the lock must be accurate to values below the atomic linewidth ($\Delta\nu_{3D-Red} < (2\pi)7,5$kHz) in order to achieve recoil temperatures.
2. The available laser intensity needs to be sufficient to be sent through a fiber to the experiment and afterward be divided into three counter-propagating beams with a waist of $w_{3D-red} \approx 1.2cm$ ($I \geq 20$ mW).
3. The spatial mode at the position of the atoms should remain stable to cold the atoms while a modulation in frequency is performed.

To satisfy the request of first item, we use a commercial laser (DL-Pro TOptica, $\Delta\nu_{free-running}/(2\pi) \approx 150$ kHz) to generate light on the wavelength of the red cooling transition ($\lambda = 689.5$nm), that from now on will be called **Master laser**. When coupled to a Super Stable Cavity (SSC - VH-6010-4 Stable Laser Systems), see figure 11, the reflected signal can be measured in a fast Photodetector and used to create an error function with a Pound Drever Hall (PDH) circuit. The PDH technique for laser stabilization mixes the photo-detector signal with a local oscillator, which is in phase with the light (due to the fact that a part od th LO frequency is injected as current modulation in the laser diode). The detected signal is proportional to phase rather than frequency changes which makes this technique strong against intensity fluctuations.(86) After phase shifting and filtering, the resulting electronic signal gives a measure of how far the laser carrier is off resonance with the cavity. The dynamic error function is then used as a frequency reference in a Fast Analog Linewidth Control (FALC 110 - TOptica) that works as a fast proportional-integral-differential (PID) regulator for stabilization of the current driving the master laser.

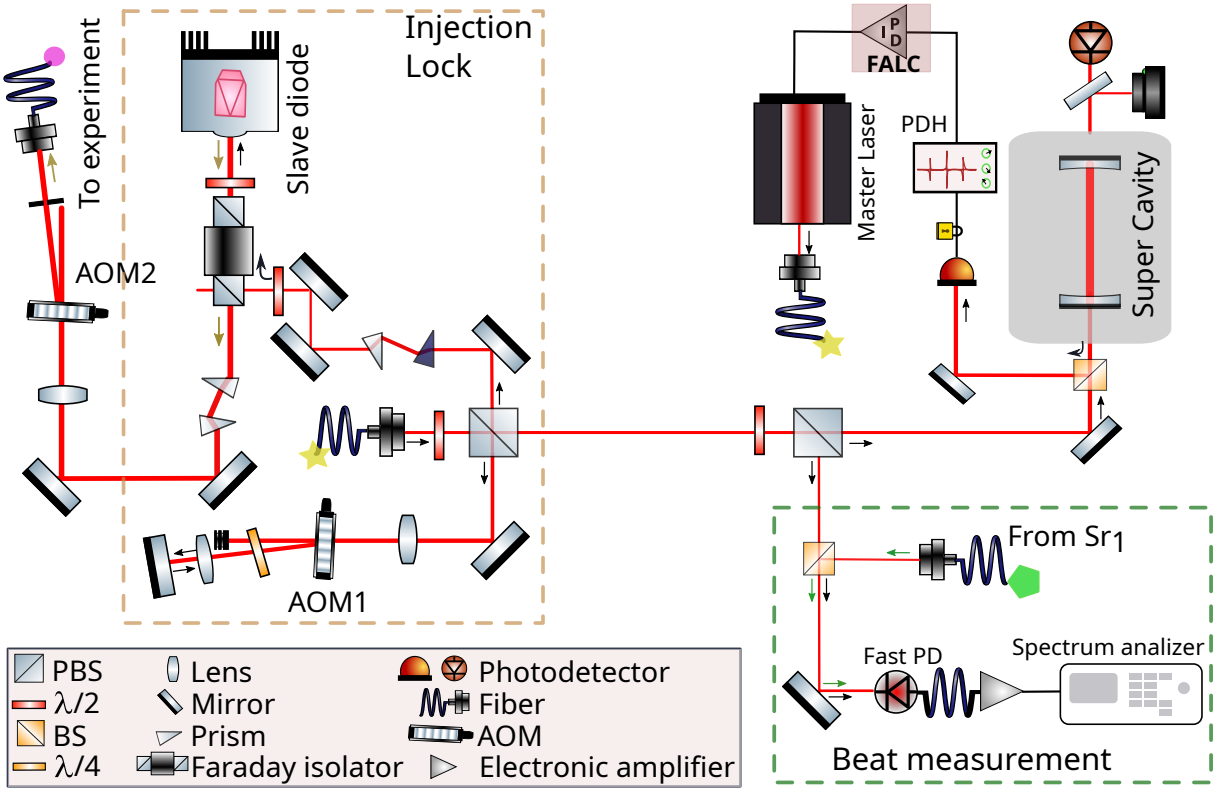

Figure 11 – Scheme of the setup used to lock the master laser in the super-cavity (upper-left) and to perform injection lock. Colored arrows at the right of the beams (red lines) indicate the propagation direction. The scheme also pictures the beat measurement technique.

Source: By the author.

A measure of the stability of the linewidth of our master laser was performed, by beating its light with the light of another laser with a similar frequency that is also stabilized to a High finesse cavity, that is the master laser used for our neighbor laboratory ($Sr1$). A beat measurement is an interferometry measure where two lasers are superimposed on a fast photodetector (Thorlabs PDA8GS - InGaAs Fiber-Coupled Amplified Photo-detector). It requires a perfect phase matching of the Gaussian laser modes. The result will be components of the frequency differences between the two lasers. This allows us to visualize variations of the path lengths of two or more partial waves following different pathways as an alteration of constructive and destructive interference, as described by eq. 1.6.

$$I = |E_1 + E_2|^2 = AB[2 + 2\cos(\omega_1 - \omega_2)t] \tag{1.6}$$

When this technique is used in uncorrelated lasers, the beat signal will give us a convolution of the spectrum differences. For correlated lasers, the beat note will give us information on the 'noise' of the correlation.

A scheme of the experimental setup used to perform this measurement is pictured

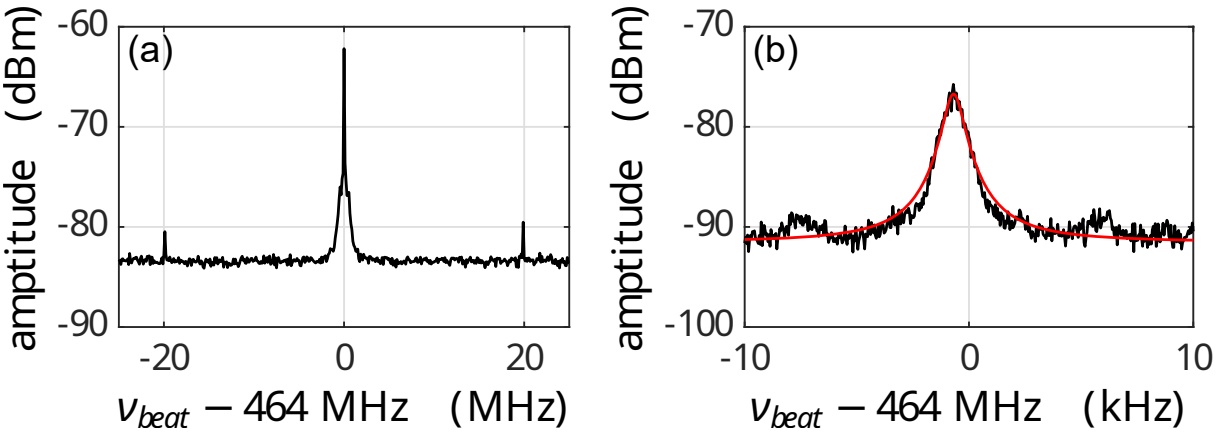

Figure 12 – Characterization of the performance of the Pound-Drever Hall (PDH) stabilization. Beat signal of two independent PDH locked lasers with 464 MHz frequency difference recorded with (a) 30 kHz and (b) 10 Hz bandwidths resolution of the spectrum analyzer. The PDH modulation sidebands are visible as small peaks at ±20 MHz. The red curve in (b) is a Lorentzian fit with an FWHM of 450 Hz. This allows us to assert that any one of the lasers has an emission bandwidth below this width.

Source: By the author.

at the bottom-right of figure 11. It is important to point out that a tilted PBS (or some polarization mixing tool) stands in front of the photo detector. This is to remove the problem that the superposition of light field amplitudes in different modes does not interfere. Therefore a mixing of the polarizations of both light fields needs to be performed to increase the contrast of the beat signal.

After stabilization, the linewidth of the Master laser is about ≈ 450 Hz as it can be appreciated in the measure shown in Fig.12. This value is sufficient request to interact with the inter combination line, the linewidth of which is of $\gamma_{red} = (2\pi)7.6$ kHz, solving item *1* of list 1.4.1. More details on the stabilization and characterization of this system can be found in the master thesis of Beli C.(87)

1.4.1.1 Injection Lock

After frequency stabilization, the available power of the Master laser is not sufficient to perform cooling of the atoms. Even though this can be solved with a Tapered Amplifier, we also deal with the necessity of performing a wide-band modulation in the AOM, that can change the angle of the diffracted light[§] according to the RF value. Therefore we implemented an injection-locked system (Master-Slave) to amplify and control the parameters of importance for the light of the fine transition, the scheme is shown on the

§ The RF driving an AOM, or also called Bragg cells, determines the angle at which the light is diffracted as: $2\Lambda \sin\theta = m\lambda/n$, where Λ is the wavelength of the sound, m is the diffraction order, n the refractive index of the medium, and λ the frequency of the light in vacuum

left side of figure 11. A percentage of the light of the master is injected into the diode laser through an optical insulator to achieve an injection lock. After ensuring spatial mode matching and when inside the injection frequency range, the slave laser will synchronize in phase with the master, and as a result, the frequency and phase of both will be identical.

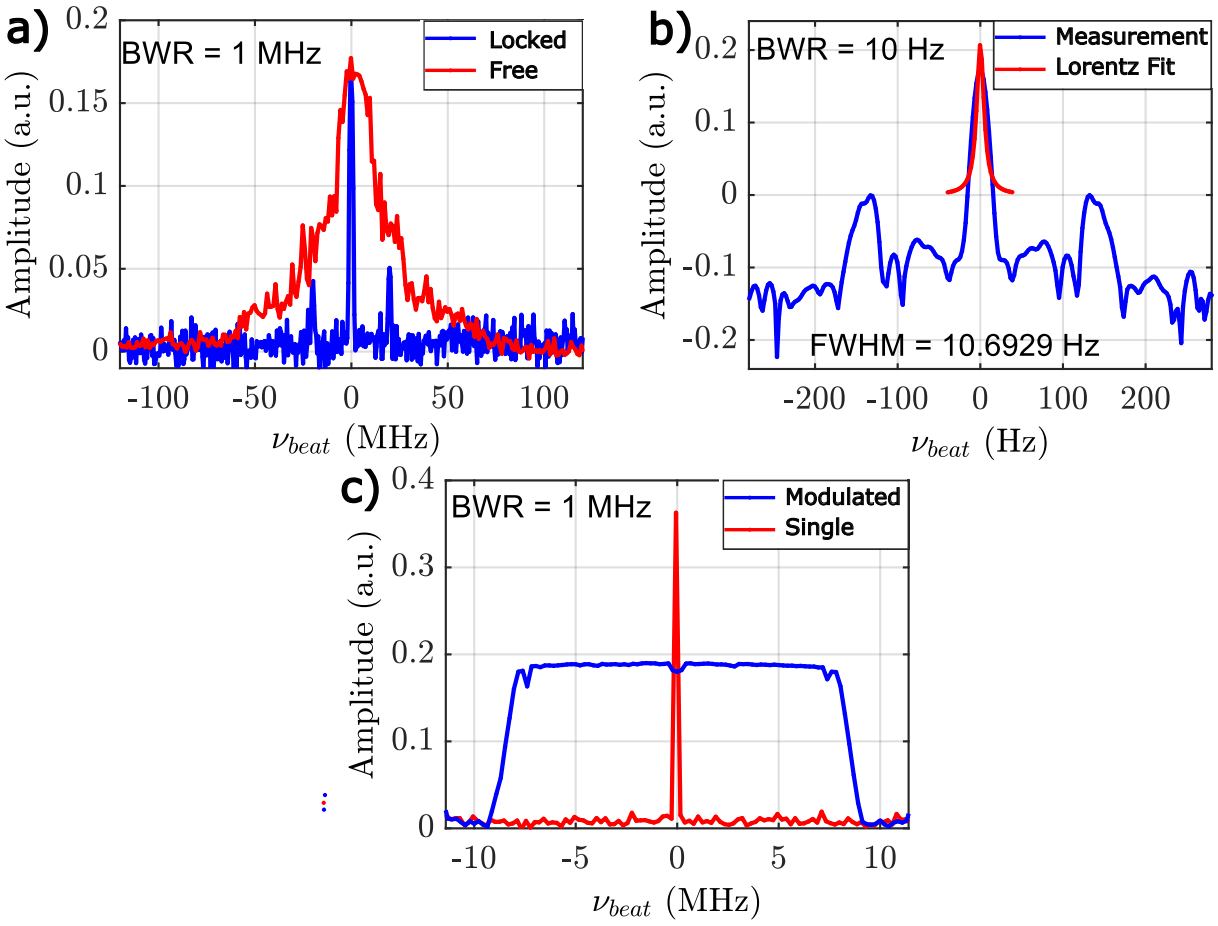

Figure 13 – (a) Beat of the correlated lasers Master and Slave showing the reduction of the linewidth after the injection process lock. The curves were frequency-shifted for easier visualization. When the injection process occurs the spectrum shows the modulation bands of the master, as well as 'extra bands' that come from the beat of the bands of the slave with the bands of the master. Using the light transmitted from the SC we may avoid this behavior. (b) 10 Hz Bandwidth resolution of the correlated lasers beat, the red curve is a Lorentzian fit with an FWHM at 3 dBm of 10 Hz. (c) The blue curve shows the spectrum of the beat frequency between laser 1 (ν_{las1}) and the red MOT light (ν_{redMOT}) when the light injected into the slave laser is frequency-modulated with a triangular wave-function with a fixed peak-to-peak frequency excursion of 8 MHz. The red curve has been taken without this modulation.

Source: By the author.

The working principle of **Injection Lock** is well described by (88, 89), and it is possible to resume these phenomena doing an analogy with oscillators; if two oscillators, let us call them Master and Slave, which have different linewidths are superimposed,

then for a specific range of frequency and injection power (coming from the master), a synchronization phenomenon can occur.(90) When this happens the slave oscillator which has a broad linewidth ($\Delta\nu_{Master} < \Delta\nu_{Slave}$), will synchronize in phase with the master and the frequency of both will be the same. This also implies a narrowing in the linewidth of the slave that matches with the Master ($\Delta\nu_{master} \equiv \Delta\nu_{injectedslave}$). This process can ensure a higher laser power with the desired frequency and stability that can be controlled independently, fulfilling in that way the two remaining items of list 1.4.1.

The light of the slave laser after the synchronization has the same frequency of the master and the intensity of the slave. Another advantage of the injection system is that we can modulate the resulting light without losing spatial coherence (frequency modulation in AOMs produces a shift in the angle of the light, which translates into a spatial shift of the beam). A modulation of frequency performed in AOM1 (Fig.14) will be instantly followed by the slave laser as seen in Fig 13b. A beat of the correlated lasers (Master and slave) can give us information about the noise of the correlation. Figure 13(c) shows a long integration time measurement of the correlation together with a Lorentz Fit. The FWHM of the fit is 10.7 Hz, which is also in the order of the resolution bandwidth used for the measurement. This indicates that the correlation noise of our lasers is lower than this value, as expected for phase-locked lasers.

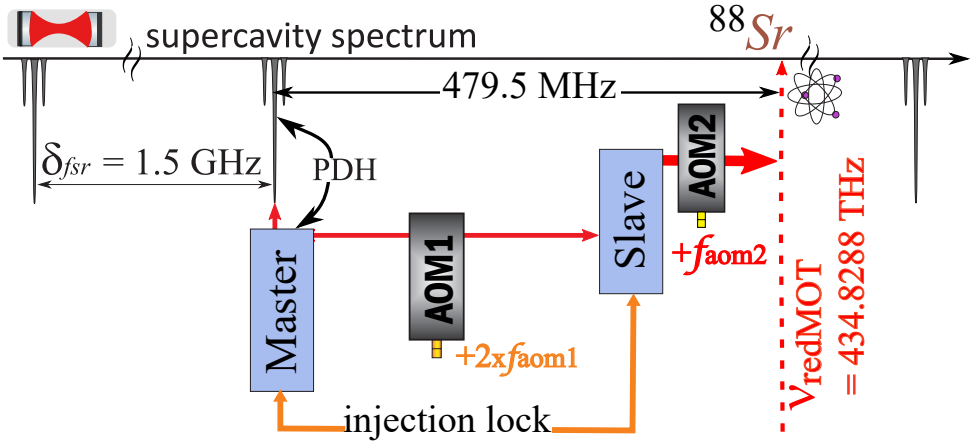

Figure 14 – Locking scheme illustrating the frequency shifts and locking points of the lasers with respect to the super cavity spectrum (upper peak array). The ^{88}Sr resonance ν_{Sr} is shown by a vertical dashed line. The acronyms are Pound-Drever-Hall (PDH) stabilization, and acousto-optic modulator (AOM).

Source: By the author.

Near-resonant light is needed for the red MOT cooling stage and, eventually, for the on-resonance excitation of the atoms. The frequency gap between the strontium line ($\nu_{Sr} = 434.8288$ THz) and the nearest super cavity mode is measured to be $\nu_{Sr} - \nu_{sup} = 479.5$ MHz. To overcome the gap, the laser beam is double-passed through a first AOM (f_{aom1}), amplified by injection into a slave laser which, after single-passing another AOM (f_{aom2}), finally illuminates the atomic cloud. The frequency modulation of the red MOT

light (see Fig. 15(c)) is implemented by modulating the frequency $f_{aom1}/2$ of the RF produced by a synthesizer (Rohde & Schwarz, SMB100A) controlling the double-pass AOM. The injection lock is clearly fast enough to handle the modulation, as demonstrated in Fig. 13(a), which shows the presence of the PDH modulation bands in the light amplified by the slave laser.

1.4.2 Ultracold cloud of Sr atoms

The problem with using the intercombination line for a MOT is that its narrow linewidth entails a small velocity capture range, far below the Doppler width of the precooled atomic cloud in the blue MOT. The temperature ($T_{blue} \sim 4$ mK) of the atomic cloud at the time of the transfer from the blue to the red MOT corresponds to a half-width of the Doppler broadening equivalent to $\sqrt{\frac{k_B T_{blue}}{m}}.\lambda_{689}^{-1} = 1$ MHz at the wavelength of the intercombination line. This is much larger than the linewidth of the transition ($\Delta\nu_{689}/2\pi = 7.6$ kHz), which reduces the spectral overlap with the red MOT laser. Since

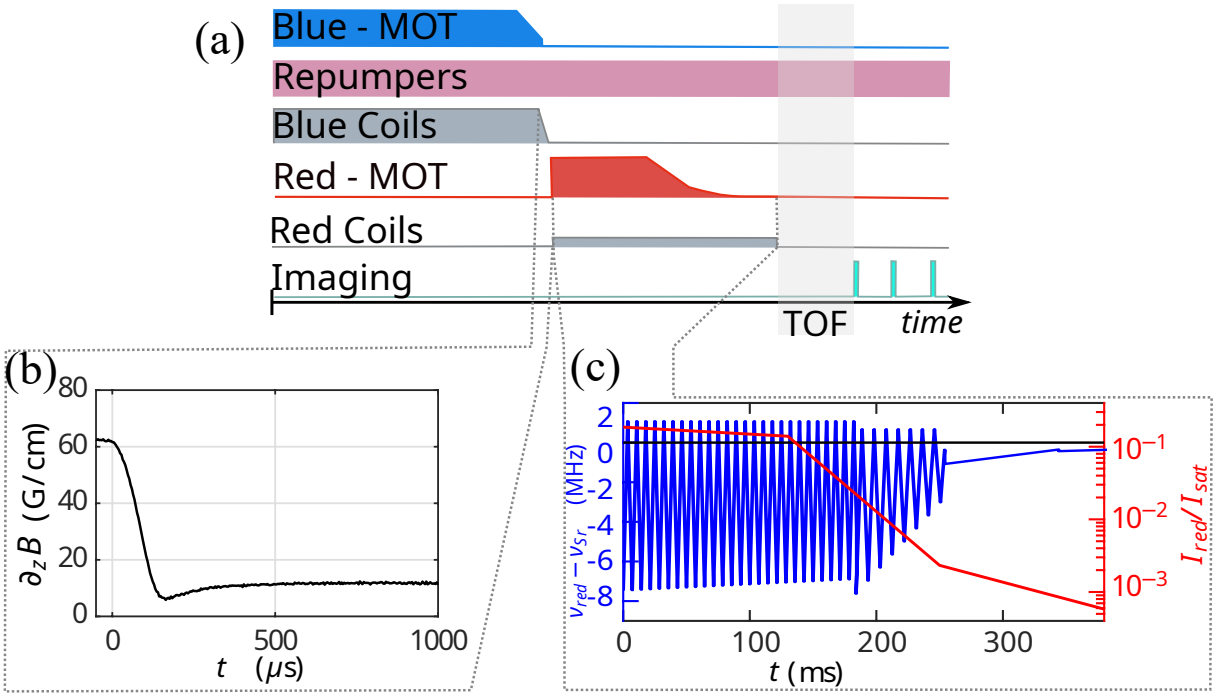

Figure 15 – (a) Time sequence for the production of a Red MOT and subsequent imaging of the cloud. (b) Switching of the magnetic field gradient (axial direction) between the blue and the red MOT. (c) Implemented red MOT frequency (blue) and power ramp (red). For clarity of illustration the modulation frequency, which in reality is 55 kHz in the first part and 25 kHz in the second, has been reduced by a factor of 200.

Source: By the author.

the blue and red transitions have different magnetic gradients ($\Delta B_{Blue} = 65$ G/cm for the Blue and 12.6 G/cm for the Red), a switch of the amplitude of the magnetic field is

necessary to transfer the atomic cloud from the blue to the red MOT without losing the atoms to high field seeking regions. Nonetheless, this switch needs to happen in a short time, since the blue cloud temperature (≈ 4 mK) is so high that most of the atoms leave the trap after 1ms. In our experiment the magnetic field gradients are quickly switched within 160 μs, as shown in Fig. 15(b). For this, we need to reduce the current in the anti-Helmholtz coils generating the magnetic fields from 8.75 A to 1.7 A. This is achieved with fast, high-voltage MOSFETs (type SCT2080KE, 1220V-44A) that allow for peak high-voltage transients caused by the coils' inductance upon fast switching of their current, and a snubber circuit in parallel with the coil, composed of a capacitance of 47 μF in series with a resistance of 100 Ω. More details on the magnetic setup and design can be found in the master thesis of Armijos M(78), and the internship report of Comito G.(91)

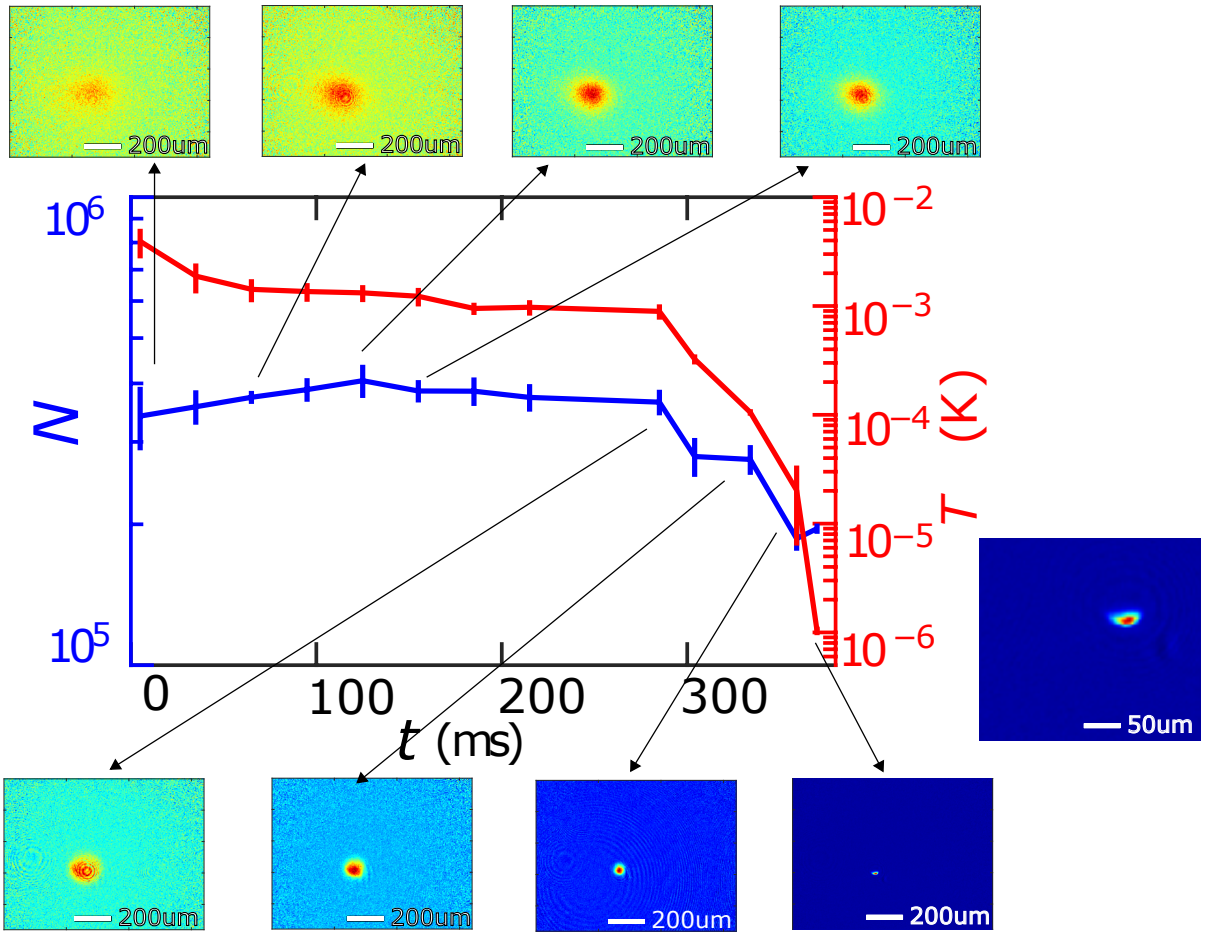

Figure 16 – Evolution of the measured atom number (blue curve) and temperature (red curve) for different times in the ramp. The insets are OD images of the cloud at different times, the background changes since the image are normalized to the maximum intensity. (inset) Red mot with 4x zoom and the pancake shape is visible.

Source: By the author.

To cool every velocity class of atoms within a certain velocity range (given by

the Doppler and saturation broadening), we frequency-modulate the red MOT laser with an excursion of $\Delta\nu_{aom1} \approx -8$ MHz, ensuring in that way the interaction with most of the atoms that remain in the beam's path after the turn off of the Blue Magnetic field. The modulation frequency is of 55 kHz in the first stage of constant excursion amplitude (1 MHz, corresponding to ≈ 140 sidebands[¶]) that last 180 ms, with an intensity of $\approx 20 I_{sat}$ per sideband ($I_{sat,689} = 3\ \mu\mathrm{W/cm^2}$). For the second stage the modulation frequency is of 25 kHz at which the excursion amplitude is reduced to $\Delta\nu_{aom1} \approx -1$ MHz, this corresponds to 40 sidebands, (see Fig. 15 and Fig.11), and lasts 100 ms. With intensities of $\approx 2 I_{sat}$. The third stage is a single-frequency ramp that slowly approaches the final frequency ($\Delta\nu_{aom1} = 0 = \nu_{red}$). Finally, for 75 ms we maintain the single frequency value fix as the cloud cools down by the final intensity ramp that can reach $I_{red} \approx 2 I_{sat}$(25), to avoid excessive power broadening exceeding the Doppler width of the atomic cloud while it cools down. A typical signature of low temperatures is given by the pancake shape that the red MOT acquires when the radiative pressure of the beams is not enough to hold the atoms against gravity. At this stage, we can see that the final position of the cloud is frequency-dependent since the atoms falling due to gravity will see the detuning of the vertical beam with a shift. This peculiarity of fine transitions allows us to adjust the final frequency of the red beam to the same relative detuning each day by putting the atoms back in the same position (remembering that the stabilization of our red light depends on the stability of the SC cavity, which shifts between $20 - 60$ kHz a day).

1.5 Red MOT characterization

After 400 ms of red MOT cooling, we typically have a cloud of 10^5 atoms at a temperature of 800 nK. As shown in Fig. 16, we capture about 10% of the atoms from the blue MOT. The frequency and the power ramps are illustrated in Fig. 15(c). For TOF = 0 the size of our cloud is of $\sigma_x = (50 \pm 3.75)\mu$m and $\sigma_y = (20 \pm 3.75)\mu$m. The lifetime of our Red MOT was measured by varying the duration time of the last stage of the frequency ramp, and maintaining the intensity of the red laser constant at a value of $I_{red} \approx 2 I_{sat,689}$. Figure 17 shows the results obtained from this measurement. An exponential fit of the curve allowed us to extract $\tau = 136$ ms.

1.5.0.1 Spectroscopy of the blue transition with the red MOT

As our Red cloud has such low temperatures, an interrogation realized with the Blue light will show no Doppler broadening. The measure shown in Fig. 18 was performed by scanning the frequency of the imaging probe beam and measuring the atom number dependence.

¶ calculated as: excursion amplitude/modulation frequency

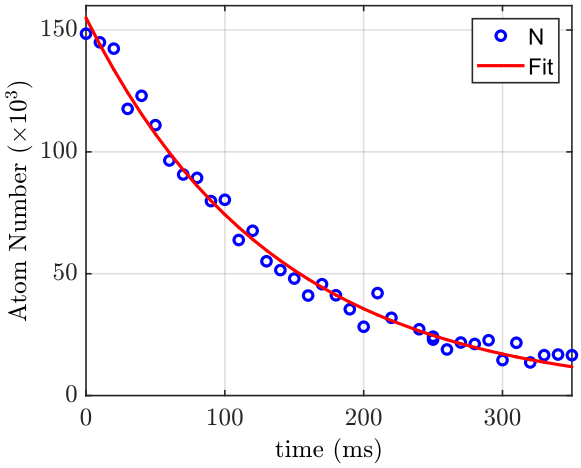

Figure 17 – Lifetime measurement of the RedMOT cloud. The red line represents an exponential fit from which the time constants are extracted. This measurement is performed by varying the time of the last stage of the modulation ramp in the frequency of the red MOT.

Source: By the author.

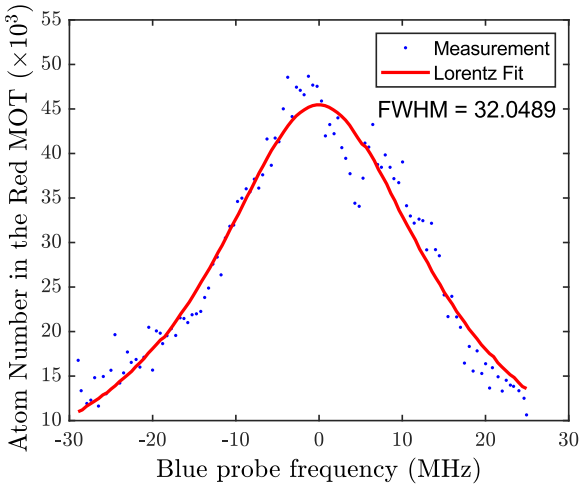

Figure 18 – Measure of the Blue transition linewidth using the Red cloud. The Blue dots represent the mean of two experimental measurements. The scanned parameter was the frequency of the blue light used to image the atoms. The red line is a Lorentzian fit of our experimental data, from which the linewidth of the transition was extracted.

Source: By the author.

A Lorentz Fit of the data allowed us to determine a linewidth of the blue transition of $\Gamma/2\pi = 32.0489$ MHz. This result is in good agreement with the values measured by SANSONETTI *et al.* (1) and STELLMER (2)

1.6 Preliminary conclusions

This first chapter resumed the construction and realization of an experiment capable of producing a cold cloud of atoms in ≈ 2 seconds, characterized by temperatures

of the order of T = 1μK that will serve as a matter wave on an interferometer.

- Enhancement of 2D-MOT efficiency employing a bi-chromatic scheme.
- Stable and accurate control of light to interact with the red transition, utilizing injection. With laser emission bandwidth reduced to below $\Delta\nu_{689} < 0.07\gamma_{red}$.
- Implementation of a bi-frequency ramp for cooling of atoms in the narrow transition.
- Cool down of Strontium atoms to temperatures of 800 nK.

2 THE RING CAVITY

The next step of this project asks for a periodic potential in which the atom will perform the oscillations. For this, we propose to use a ring cavity pumped from both directions. This chapter focuses on the setup and characterization of the ring cavity system and the loading of atoms in a dipolar 1D-trap realized inside the cavity.

The first part of the chapter will focus on the stabilization of the light at which the cavity will be tuned. Later on, we will describe and characterize our bare ring cavity. Next, the cavity will be used as a far-detuned trap for the atoms, from the narrow transition. The characterization of the trap will be done at the end of the chapter, and relevant parameters will be discussed.

2.1 Design and setup

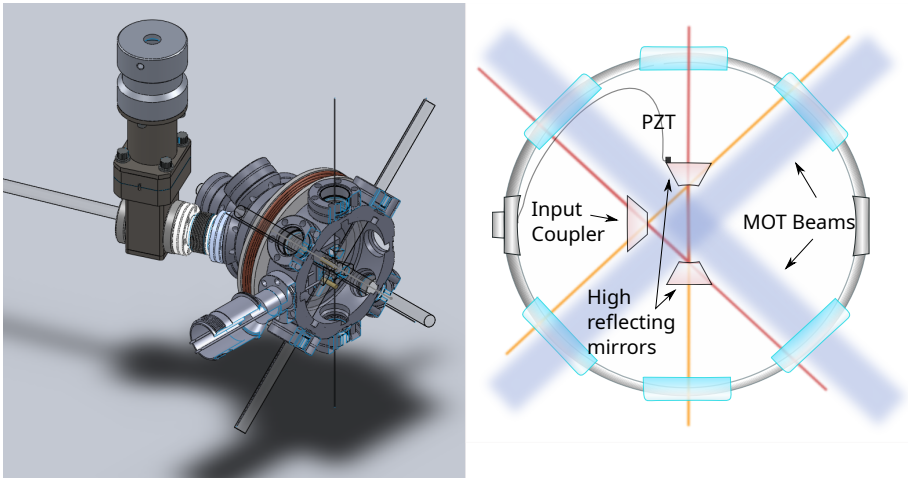

Figure 19 – (left) Ring cavity inside of the science chamber (Solidworks schematic). (right) The 2D scheme at the cavity plane of the input and output beams in the science chamber. The red and orange light beams represent the different directions of light coupling and the expected transmissions.

Source: By the author.

In order to keep the experiment simple, we decided to trap and cool the atomic cloud at the same location of space, where the cavity-atom interaction takes place. The challenge of this approach, however, is to design the experimental setup such as to ensure optical access to all 6 ports of the ring cavity, as well as to the cooling beams of the magneto-optical trap (MOT) (see figure 19), which also come from 6 different directions of space and must have a minimum diameter to ensure a sufficiently large velocity capture range.(92) Furthermore, there must be a clear passage for the atomic beam feeding the MOT (push) and for the laser beams used for imaging the atomic cloud.

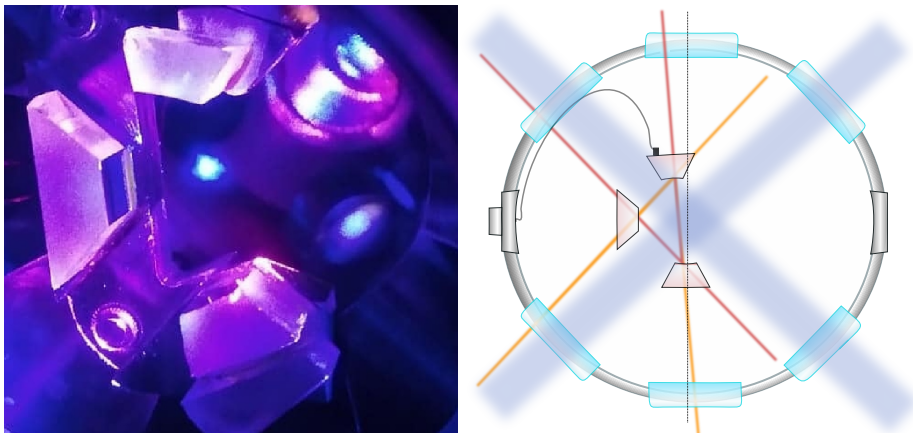

Figure 20 – (left) Photo of the Blue-MOT in the cavity plane(Dec-2021), where the top HR mirror displacement is also appreciated. (right) Scheme of the input and output beams in the science chamber for the tilted cavity, a black line was added to serve as a guide.

Source: By the author.

The final design of the ring cavity was projected as shown in figure 19. In that way, the cavity would be an isosceles triangle with the longest side of the triangle in the same direction of gravity. Our projection also included finesses of 1500 and 500 (calculated with eq.2.1 and the reflectivities indicated from the mirror's manufacturer) as well as 4 transmission beams (2 for each HR mirror). Unfortunately, our setup suffered an unlucky modification. When the main chamber was being baked (as part of the UHV process) one of the cavity mirrors moved and we end up with a slightly different geometry. It is possible to appreciate in the photo of figure 20 how the top mirror of the cavity lays outside of the cavity support. This (un)lucky event affected the cavity (and the experiment) in the following way:

- The isosceles triangle is now an almost isosceles triangle, that is also tilted from the vertical in $\alpha = 0.214\text{rad} = 12.3°$.
- The cavity length is shorter, therefore the free spectral range (δ_{fsr}) is larger.
- Instead of 4 accessible transmissions we have access to just two since 2 of the transmission beams now are blocked by the chamber(See Fig. 20b).
- One of the MOT beams is partially cut by the cavity mirror, therefore a misalignment is necessary to ensure an effective trapping region.
- The misaligned MOT will now be formed outside of the cavity mode, and a method for moving it a short distance is also necessary.

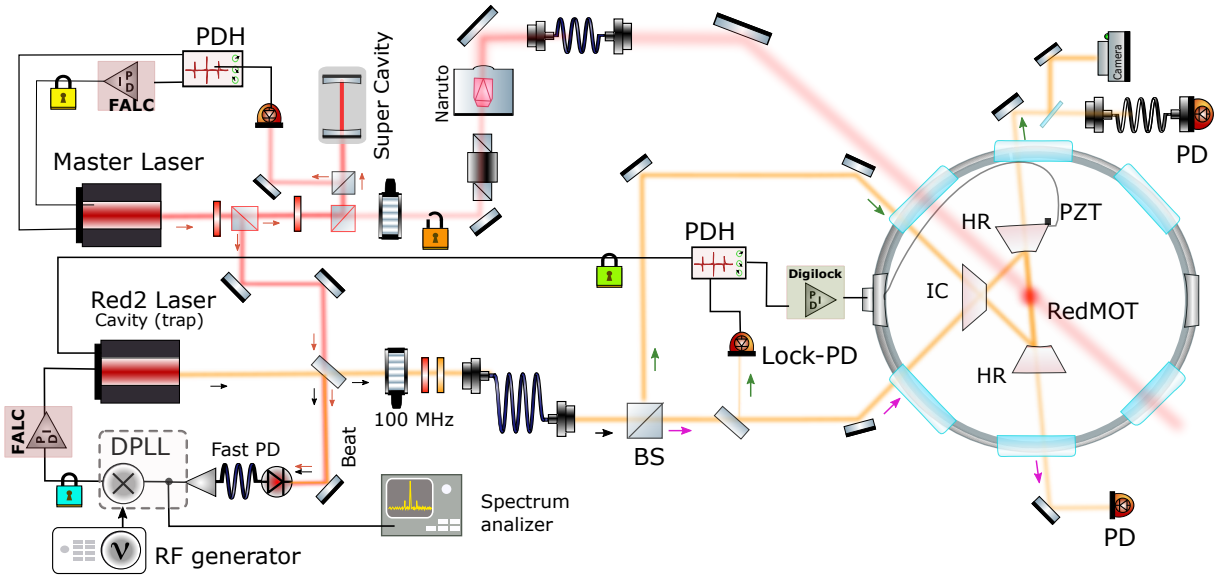

Figure 21 – Optical setup of the cavity spectrometer. Colored arrows at the right of the beams (colored blurred lines) indicate the propagation direction. Black solid lines represent electronic connections. The master laser is tightly locked to a reference cavity (Super cavity) via a Pound-Drever-Hall servo (PDH), tuned close to the narrow atomic resonance. It serves for cooling the atomic cloud (red MOT). The ring cavity length can be controlled via the piezo (PZT) located in one of the high reflectors (HR). The PZT is locked via PDH to a second laser (Red 2). The light of the master and the red2 lasers is overlapped in a fast photo-detector (PD). The frequency difference (Beat) is phase-locked via a DPLL to laser red2. The light of the laser red2 inside the ring cavity generates an optical dipole potential for the atoms in the red-MOT. (inset) Locking scheme illustrating the frequency shifts and locking points of the lasers with respect to the atomic resonance, the cavities spectra are pictured in scale.

Source: By the author.

2.2 The cavity laser spectrometer

A laser operating near the 689 nm inter-combination line is injected in the cavity to be used as a reference for it. This laser is also responsible to generate the vertical standing wave along the ring cavity axis, in which the strontium atoms shall perform Bloch oscillations. The optical setup for coupling light into the cavity and the locking scheme of the red laser spectrometer is shown in Fig. 21. This setup gave us control over the length of the ring cavity with high precision, such that we can tune one of its resonance frequencies close to the strontium line or to the frequency detuning we desire.

We implement this via a sequential chain of three locking systems, see fig 22. A first laser (Master laser ν_{las1}) is locked to a stable reference cavity (supercavity), a second laser (Red2 ν_{las2}) is offset-locked to the first one via a digital phase-locked loop (dPLL),

and finally the ring cavity length is stabilized to the second laser. We will explain the procedure in detail in the following sections.

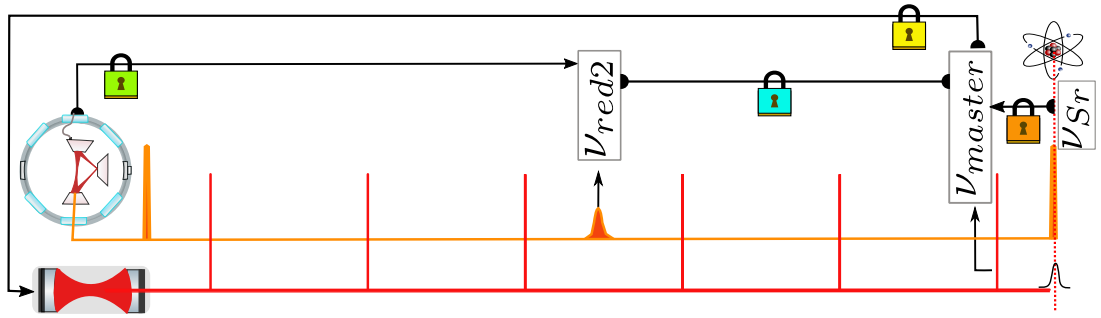

Figure 22 – Locking scheme illustrating the frequency shifts and locking points of the lasers with respect to the atomic resonance. The cavities transmissions spectra (TEM_{00}'s) quasi at scale, is also pictured. The lock chain direction is pictured as $\longmapsto$. In that way, the laser that interacts with the narrow atomic resonance is phase-locked to ($\longmapsto$) the master laser via injection lock. The master laser by its time is locked to ($\longmapsto$) the closest super cavity mode via PDH and a FALC. The ring cavity piezo follows ($\longmapsto$) the Red_2 laser through the scan module and a Digilock. The PDH modulated Laser2 can simultaneously be arbitrary (limited to frequency differences of $\Delta\nu_{\pm|\text{master}-\text{red2}|} < 6\text{GHz}$) locked to ($\longmapsto$) the stable master laser via a DPLL and a FALC.

Source: By the author.

2.2.1 Controlling the cavity length

The second laser (ν_{red2}) can be locked to the ring cavity using the PDH technique in the same way as for the stabilization of laser 1. This allows us to monitor the temporal drift of the ring cavity length by measuring the frequency of laser 2 as a function of time. Fig. 23(a) shows the time evolution of the frequency beat between laser 2 (locked to the ring cavity) and laser 1 (locked to the stable super cavity), as monitored with a spectrum analyzer. The fluctuations of several 10 MHz over minutes reflect the instability of the ring cavity, which is not mechanically nor thermally isolated.

The large frequency drifts observed for the ring cavity resonance frequency were expected and demonstrate the necessity of its stabilization. For this purpose, one of the cavity mirrors is mounted on a piezo-electric transducer (PZT) (Physik Instrumente, PICMA PL0XT0001). The piezo in the cavity is controlled via a Scan Control module from Toptica. This allows us to tune the length of the ring cavity and to stabilize it to the frequency ν_{red2} of laser 2. In practice, we achieve this stabilization by creating an error signal with PDH modulation of laser 2 at 18MHz. A proportional-integral-differential (PID) servo electronics (Toptica, DigiLock) feeds the correction function to the piezo via the back panel of the Toptica module.

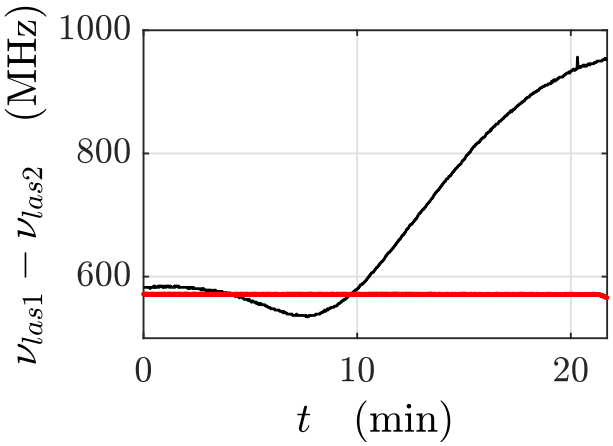

Figure 23 – Long-term characterization of the frequency drifts of the ring cavity. The black curve shows the natural drifts of the ring cavity. The red curve shows the same signal when the ring cavity was additionally locked to laser 1 via a lock-in amplifier and PID servo electronics (Toptica, DigiLock).

Source: By the author.

Laser 2, in turn, can be locked to a stable reference. The locking scheme should, however, satisfy two conditions. First of all, it is important to avoid perturbing (heating) the atomic cloud stored inside the ring cavity by the laser field. This implies that the frequency ν_{las2} of laser 2 must be tuned sufficiently far enough from the strontium resonance. Thanks to the narrowness of the inter-combination line, tuning the laser some few GHz to the red, is sufficient to avoid spontaneous scattering processes.

Second, we aim for wide tuning ranges covering the whole spectral range of the ring cavity. Both conditions are met by a Digital Phase Lock Loop (DPLL), as detailed in the next section.

2.2.2 Phase-locking of the lasers - three locks chain

In our spectrometer, exhibited in Fig. 21, we implement an offset-lock of laser 2 to laser 1 by beating both lasers on a fast photo-detector (Thorlabs, PDA8GS). The beat frequency is now divided by 32 via a digital PLL (Analog Devices evaluation board, EVAL-ADF4007) (93) and compared to the RF frequency f_{mw} provided by a stable frequency synthesizer (Rohde & Schwarz, SMB100A). The comparison generates a step signal that can be used as an error to fed into the PID-electronics (Toptica, FALC110) controlling the laser 2 (Toptica, DLpro). Varying f_{mw}, the laser frequency ν_{las2} can now be tuned with 1 Hz precision, and through it the length of the ring cavity. As illustrated in Fig. 21, the resonance frequencies of the ring cavity can be varied over wide ranges, e.g. it is possible to tune a cavity mode adjacent to the mode-locked to laser 2 across the strontium line.

We characterize the performance of the digital PLL stabilization by measuring the beat signal width. One laser (ν_{las1}) was locked to a mode of supercavity by means

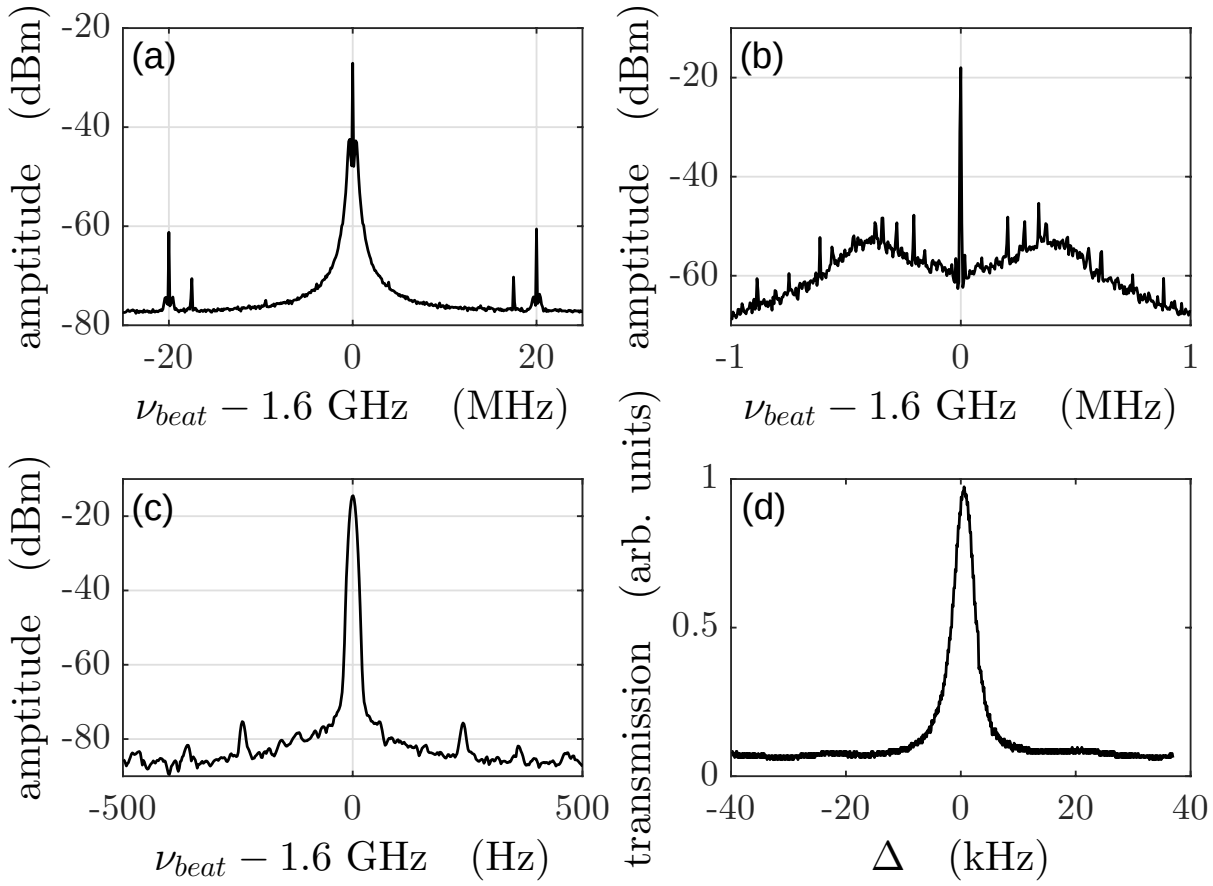

Figure 24 – (a) Beat signal of the two mutually phase-locked lasers recorded with 30 kHz resolution bandwidth of the spectrum analyzer. For this measurement, the lasers had a frequency difference of 1.6 GHz. (b) Same as (a) but with 3 kHz resolution bandwidth. (c) Same as (a) but with 10 Hz resolution bandwidth. (d) Transmission spectrum of the supercavity.

Source: By the author.

of a Pound-Drever-Hall stabilization. The other laser (ν_{las2}) was locked to the first one by means of a digital PLL, as described in Ref.(93) Fig. 24(a-c) show beat frequency measurements between the (free-running) laser 1 and laser 2 being DPLL-locked to laser 1 for various resolution bandwidths. The 10 Hz width of the peak in Fig. 24(c) is limited by the minimum resolution bandwidth of the spectrum analyzer (Agilent, N9320B) of 10 Hz. As both lasers are correlated this width gives us information of the relative de-phase among the lasers *.

An alternative way to measure the digital PLL stability is to use laser 2 to measure the decay of the supercavity. For that, we locked laser 1 to a supercavity mode via PDH

* Fig24d: Laser ν_{las1} was locked to a cavity and generated a constant transmission visible as a small offset at all detunings. Additionally, laser ν_{las2} was ramped over an adjacent supercavity mode. The measurement yields the free spectral range of the supercavity $\delta_{fsr}^{sup} = 1.445065$ GHz, and from the 5 kHz width of the spectrum, we infer a finesse of $F = 185000$

electronics, laser 2 on laser 1 via the digital PLL, and ramped the synthesizer frequency which feeds the PLL such as to tune laser 2 across an adjacent supercavity mode. The transmission spectrum of the supercavity is shown in Fig. 24(d). The center of the transmission peak allows us to extract the free spectral range of the supercavity with high precision, $\delta_{fsr}^{sup} = 1.445065$ GHz. From that, and from the width of the transmission peak ($\kappa_{SC} = 5kHz$), we obtain a finesse of the supercavity of $F = 185000$.

2.3 Characterization of the empty ring cavity

Our ring cavity consists of a plane input coupler (IC) and two curved high-reflecting (HR) mirrors (50 mm radius of curvature) (Dorotek GmbH). The two highly reflecting mirrors have measured reflectivities of $R_{hr,s} = 99.85\%$ and $R_{hr,p} = 99.71\%$ for the two polarizations under an angle of incidence of $\alpha = 22.5°$. The incoupler measured reflectivity is $R_{ic,s} = 99.69\%$ and $R_{ic,p} = 96.72\%$ for the two polarizations under an angle of incidence of $\beta = 45°$. [†]. With this, we expect a finesse of

$$F_n = \frac{\pi(R_{hr,n}^2 R_{ic,n})^{1/6}}{1 - (R_{hr,n}^2 R_{ic,n})^{1/3}} \tag{2.1}$$

with $n = s, p$, yielding $F_s = 1546$ and $F_p = 241$. We measured, however, the finesses $F_s = 1043$ and $F_p = 98.78$. The mean reflectivities are then,

$$\bar{R}_n \equiv (R_{hr,n}^2 R_{ic,n})^{1/3} \simeq 1 - \frac{\pi}{F} \tag{2.2}$$

corresponding to these finesses are $\bar{R}_s = 99.7\%$ and $\bar{R}_p = 96.82\%$.

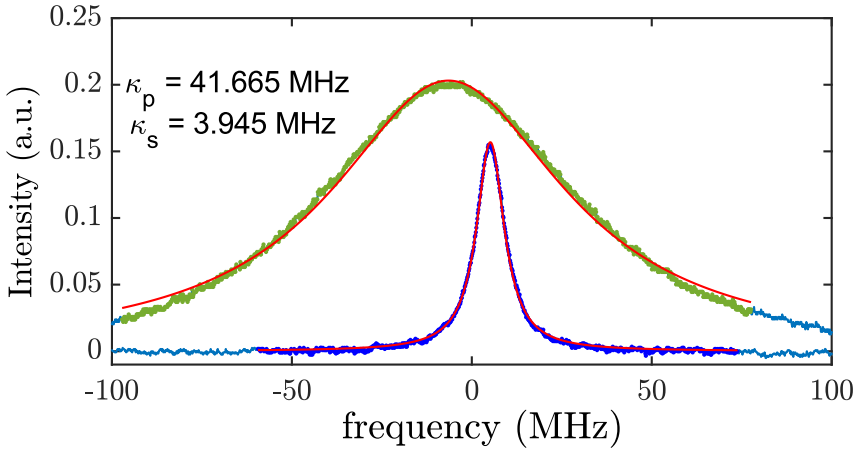

Figure 25 – Transmission line-shapes and Lorentzian fit (red) of the mode profiles for the (blue) High finesse and (green) low finesse polarization.

Source: By the author.

2.3.0.1 Finesse

The measurement of the finesse of our cavity was performed and the traces used for the calculations are presented in fig. 25. This is performed by means of the relation among the distance between two adjacent modes (measured in time, Volts of the PZT or frequency), that is the δ_{fsr} divided by the width of the mode (2κ). For the **p** polarization we measured $F_p = 99$ and $\kappa_p = 41.7$MHz. For the **s** polarization the measurement gave

[†] The reflectivities specified by the seller are much higher: $R_{hr,s} = 99.97\%$ and $R_{hr,p} = 99.92\%$ under an angle of incidence of $\alpha = 22.5°$ and $R_{ic,s} = 99.74\%$ and $R_{ic,p} = 99.74\%$ under an angle of incidence of $\beta = 45°$.

$F_s = 1043$ and $\kappa_s = 3.95$MHz. As the finesse measurements are more precise than the reflectivity measurements, we will use them in the following to recalibrate the input coupler reflectivities according to $R_{ic,n} = \bar{R}_n^3/R_{hr,n}^2$, yielding $R_{ic,s} = 99.4\%$ and $R_{ic,p} = 91.29\%$. The cavity free spectral range is now obtained as,

$$\delta_{fsr} = 2F_n * \kappa_n \tag{2.3}$$

giving, $\kappa_s/2\pi = 3.945\,\text{MHz}$ we can obtain $\delta_{fsr}/2\pi = 8.23\,\text{GHz}$. This value agrees with a measurement performed using the wavemeter which has an error of ±20MHz, the value measured with the wavemeter was 8.24 GHz. This corresponds to a round trip length on the ring cavity of:

$$L = \frac{c}{\delta_{fsr}}\ , \tag{2.4}$$

yielding $L = 3.64\,\text{cm}$. This calculation was confirmed by measuring the distances **a** and **b** and **c** (see figure 26) by using a CCD camera focused in the cavity plane and comparing the distances among the bright dots (scattering on the surface of the mirrors) that can be seen when the cavity is locked at the T_{00} mode with the size of the side of the incoupler mirror ($l = 5mm$). The result is shown in figure 26, a dotted line sketching out the path of the light inside of the cavity. We obtained a discrepancy of 2% between the calculated and measured round trip.

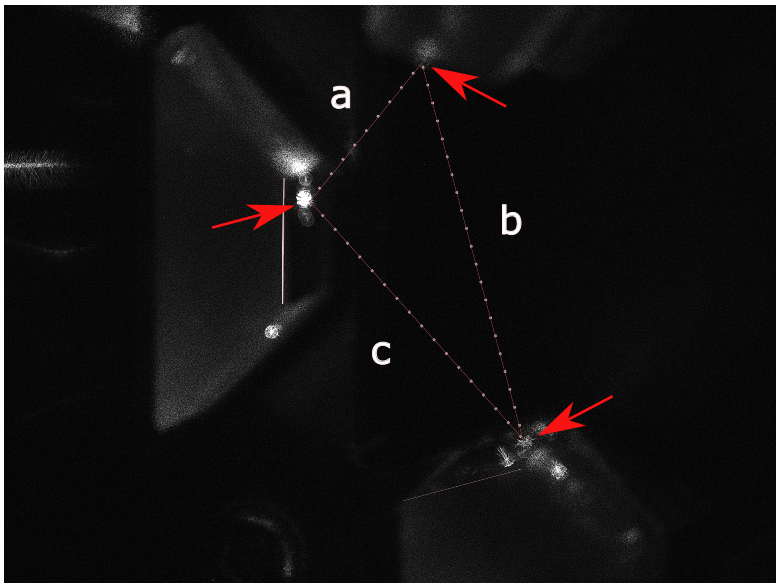

Figure 26 – Photo of cavity mirrors and the scattered light of the locked cavity used to calculate the distances between mirrors. The red arrows indicate the spots where the beam is reflected in the mirror. The side of the incoupler mirror (left) and the HR mirror (bottom and top) are used as calibration (l = 5mm).

Source: By the author.

2.3.1 Geometry of the ring cavity

The radii of curvature of the spherical highly reflecting cavity mirrors are $\rho = 50\,\text{mm}$, while the incoupler mirror is plane. Under the angle of incidence α, the mirror effective radius of curvature perpendicular to the ring cavity plane, $\rho_\perp$, and the effective radius of curvature parallel to the plane, $\rho_\parallel$, modify to,

$$\rho_\perp = \frac{\rho}{\cos\alpha} \qquad \text{respectively} \qquad \rho_\parallel = \rho\cos\alpha\ . \tag{2.5}$$

With this, we calculate the waists of the cavity mode. We denote by a the distance between the incoupling and high-reflecting mirror at the top, b the distance between each high-reflecting (HR) mirror, and c the distance between the HR mirror at the bottom and the incoupler (see fig. 26). For symmetry reasons, it is clear that there must be two waists of the cavity mode. One waist, $w_{0,m}$ $(m = \perp, \parallel)$ is in free space halfway between the high reflecting mirrors, and we calculate it with the help of the propagation matrix M for a round-trip beginning at the waist position.

$$\begin{aligned} M &= \begin{pmatrix} 1 & b/2 \\ 0 & 1 \end{pmatrix} \begin{pmatrix} 1 & 0 \\ -2/\rho_m & 1 \end{pmatrix} \begin{pmatrix} 1 & a+c \\ 0 & 1 \end{pmatrix} \begin{pmatrix} 1 & 0 \\ -2/\rho_m & 1 \end{pmatrix} \begin{pmatrix} 1 & b/2 \\ 0 & 1 \end{pmatrix} \\ w_{0m}^2 &= \left(\frac{\lambda_{689}}{\pi}\right) \frac{|M_{12}|}{\sqrt{1-\frac{1}{4}(M_{22}+M_{11})}}\ , \end{aligned} \tag{2.6}$$

Where ρ_m, the curvature radius of the HR mirror, is 0.05 m, as requested to the fabricator. Equation 2.6 yields $w_0 = 65.25\,\mu\text{m}$. Which is the waist of the cavity mode at the location of the atoms.

The other waist w_{2m} is on the incoupler plane mirror, and we calculate it with the help of the propagation matrix N for a round-trip beginning at the plane mirror,

$$\begin{aligned} N &= \begin{pmatrix} 1 & a \\ 0 & 1 \end{pmatrix} \begin{pmatrix} 1 & 0 \\ -2/\rho_m & 1 \end{pmatrix} \begin{pmatrix} 1 & b \\ 0 & 1 \end{pmatrix} \begin{pmatrix} 1 & 0 \\ -2/\rho_m & 1 \end{pmatrix} \begin{pmatrix} 1 & c \\ 0 & 1 \end{pmatrix} \\ w_{2m}^2 &= \left(\frac{\lambda_{689}}{\pi}\right) \frac{|N_{12}|}{\sqrt{1-\frac{1}{4}(N_{22}+N_{11})}}\ , \end{aligned} \tag{2.7}$$

Equation 2.7 yields $w_2 = 61.6\,\mu\text{m}$. This value also indicates the ideal waist focus of the incoming beam for best mode matching.

The mode volume of the cavity is obtained by integrating over the entire mode via the condition, $I(0)V = \int I(\mathbf{r})d^3r$,

$$V = \pi w_0^2 b\left[1+\left(\frac{\lambda_{689}b}{2\pi w_0^2}\right)^{2/3}\right] + \pi w_2^2(a+c)\left[1+\left(\frac{\lambda_{689}(a+c)}{4\pi w_2^2}\right)^{2/3}\right]\ , \tag{2.8}$$

giving $V = 0.5\,\mathrm{mm}^3$. In fact, this value is well approximated by,

$$V \simeq \pi w_0^2 L \ , \tag{2.9}$$

which is the expression we will use from now on.

2.3.1.1 Gain by resonant enhancement of the intracavity field

An interesting feature of creating light potentials with cavities is that the light can circulate several times inside the cavity before leaking out. That is translated into an intensity enhancement of the light inside of the cavity, this gain can be written in terms of the cavity finesse or more intuitively in terms of the mirrors' transmission.

To estimate the intracavity power P_{cav} we proceed as follows: (We call P_{in} the power provided to pump the cavity and begin calculating the cavity field amplitude assuming plane waves,

$$\mathcal{E}_{cav} = \mathcal{E}_{in} t_{ic} \sum_n (-r_{hr}^2 r_{ic})^n e^{\imath k(nL+x)} = \frac{\mathcal{E}_{in} t_{ic} e^{\imath k x}}{1 + r_{hr}^2 r_{ic} e^{\imath k L}} \tag{2.10}$$

which is the well-known Airy formula. From this, in resonance, $kL = \pi(2n-1)$, the enhancement factor of the cavity becomes,

$$G \equiv \frac{I_{cav}}{I_{in}} = \frac{|\mathcal{E}_{cav}|^2}{|\mathcal{E}_{in}|^2} = \frac{t_{ic}^2}{(1 - r_{hr}^2 r_{ic})^2} = \frac{T_{ic}}{\left(1 - \bar{R}^{3/2}\right)^2} \ , \tag{2.11}$$

exploiting the abbreviation 2.2, that is $\bar{R}^3 = R_{hr}^2 R_{ic}$. Noting that for the given finesses 2.1 the mean reflection $\bar{R}$ is fixed, we may also express the gain as a function of R_{hr} only,

$$G = \frac{1 - \frac{\bar{R}^3}{R_{hr}^2}}{(1 - \bar{R}^{3/2})^2} \ . \tag{2.12}$$

Inserting the reflectivities measured at the beginning 2.3, we obtain the gains $G_s = 296$ and $G_p = 39$. Similarly,

$$\mathcal{E}_{trns} = \mathcal{E}_{in} t_{ic} t_{hr} e^{\imath k a} \sum_n (-r_{hr}^2 r_{ic})^n e^{\imath n k L} = \mathcal{E}_{in} \frac{t_{ic} t_{hr} e^{\imath k a}}{1 + r_{hr}^2 r_{ic} e^{\imath k L}} \ , \tag{2.13}$$

yielding,

$$\frac{I_{trns}}{I_{in}} = \frac{|\mathcal{E}_{trns}|^2}{|\mathcal{E}_{in}|^2} = \frac{t_{ic}^2 t_{hr}^2}{(1 - r_{hr}^2 r_{ic})^2} = \frac{T_{ic} T_{hr}}{(1 - \bar{R}^{3/2})^2} = G T_{hr} \ , \tag{2.14}$$

such that,

$$\boxed{\frac{I_{trns}}{I_{cav}} = T_{hr}} \ . \tag{2.15}$$

Therefore, we may simply deduce the intracavity power from the light transmitted through a high-reflecting mirror. We just need to know the mirror transmission T_{hr}. Inserting the reflectivities given at the beginning, we obtain the power ratios, $T_{hr,s}^{-1} = 332$ and $T_{hr,p}^{-1} = 31.4$.

Table 1 – Ring cavity parameters:

cavity round trip length	L	$= 3.64\,\mathrm{cm}$		
cavity mode volume	V	$= 0.50\,\mathrm{mm}^3$		
cavity mode free space waist	w_0	$= 65.25\,\mu\mathrm{m}$		
free spectral range	δ_{fsr}	$= 8.23\,\mathrm{GHz}$		
curvature of high reflectors	ρ	$= 50\,\mathrm{mm}$		
reflection of high reflector	$R_{hr,s}$	$= 99.85\%$	$R_{hr,p}$	$= 99.71\%$
reflection of in coupler	$R_{ic,s}$	$= 99.4\%$	$R_{ic,p}$	$= 91.29\%$
finesse	F_s	$= 1043$	F_p	$= 99$
supposed resonant gains	G_s	$= 296$	G_p	$= 39$
transmission at HR mirror	$T_{hr,s}^{-1}$	$= 332$	$T_{hr,p}^{-1}$	$= 31$
cavity linewidth	$\kappa_s/2\pi$	$= 3.945\,\mathrm{MHz}$	$\kappa_p/2\pi$	$= 41.655\,\mathrm{MHz}$
transition wavelength	λ	$= 689\,\mathrm{nm}$		
transition linewidth	$\Gamma/2\pi$	$= 7.6\,\mathrm{kHz}$		

Source: By the author.

2.3.2 Ring cavity parameters

Table 1 summarizes the invariable experimental constants of our ring cavity:

2.4 Trapping atoms in an intracavity optical dipole potential

Contrary to the dissipative interaction (radiative pressure of near-resonant light) that atoms feel in a MOT, when atoms interact with a light field tuned away from the resonance the trap is conservative, and the force can be described as:

$$F_{dp} = \nabla_r \frac{-\hbar\Delta\Omega^2}{4\Delta^2 + \Gamma^2} \qquad \text{for} \qquad |\Delta| >> \Gamma \longrightarrow -\nabla_r \frac{\hbar\Omega^2}{4\Delta} \tag{2.16}$$

The dipolar gradient force can be understood as the force resulting from the interaction of the atomic transition dipole (induced by the oscillating electric field of the light) with the gradient of the electric field amplitude.

The strength of this gradient can be controlled by the intensity of the light beam interacting with the atoms ($\Omega^2 = \sigma_{opt}\Gamma I/\hbar\omega$), or by tuning the frequency difference of the light with the transition. The approximation in 2.16, is sufficiently fulfilled when $|\Delta| > 100\Gamma$. By changing the detuning below or above an atomic transition, we can control the sign of the force acting on the atom. That is, lightly tuned to the red of the resonance attracts the atom to the maximum intensity, while tuning it above resonance makes a repulsive interaction.

The dipole force is a stimulated process without energy exchange between the field and the atom. Photons are absorbed in one light mode and reappear by stimulated emission in another one. However, conservation of momentum requires that the change in the propagation direction of the scattered photons from an initial mode to a final

mode leaves the atom with a recoil. Contrary to spontaneous force, there is, in principle, no upper limit for the magnitude of the dipole force, since it is a function of the field gradient only and the detuning. Integration over the relevant spatial coordinates results in an effective potential or barrier to the atom.

The dipole force exerted by a far-detuned laser beam can be derived from the gradient of the Rabi frequency $\mathbf{F} = -\nabla(d.\mathcal{E}\ )$. Hence, it can be derived from an optical potential, which can be used for trapping. The force may be attractive (toward the intensity maximum) for red detuning, or repulsive for blue detuning (towards the intensity minima). Compared to MOTs, optical traps (far off-resonance optical trap, FORT) are tuned far away from resonances, where the population in excited states is insignificant and spontaneous forces are absent. Note from Eq. 2.16, that the potential derived from the dipolar force only decreases linearly with the detuning. The off-resonant optical density is negligible, so radiation trapping is not an issue. The most simple FORT consists of a single focused, linearly polarized Gaussian laser beam tuned far to the red of an atomic resonance. For large detunings and strong field gradients the equation for the potential become:

$$U(\mathbf{r}) \approx \frac{\hbar\omega(\mathbf{r})^2}{4\Delta} = \frac{3\pi c^2}{2\omega_0^3}\frac{\Gamma}{\Delta}I(\mathbf{r}) \qquad \text{and} \qquad \hbar\gamma_{sct}(r) \approx \sigma_A(\Delta)\frac{I(\mathbf{r})}{\omega} \tag{2.17}$$

Using the Rabi frequency:

$$\hbar\Omega = d_{12}.\mathcal{E} \tag{2.18}$$

With the dipole moment $d_{12} = \sqrt{3\pi\epsilon_0\hbar\Gamma/k^3}$, and the intensity $I = \frac{\epsilon_0}{2}c|\mathcal{E}|^2$. This shows that the potential becomes directly proportional to the light intensity and inversely proportional to the detuning. Therefore, at large detuning but very high intensity, the depth of the FORT can be maintained, although the atoms do not absorb photons.

2.4.1 Intensity in the free space focus

The light fields inside the cavity are Gaussian beams, that have an intensity distribution like:

$$I_{cav}(\rho, z) = \frac{2P_{cav}}{\pi w^2(z)}e^{-2\rho^2/w^2(z)} \tag{2.19}$$

with

$$w(z) = w_0\sqrt{1 + \left(\frac{\lambda z}{\pi w_0^2}\right)^2}\ . \tag{2.20}$$

In the case of perfect mode-matching (for nonideal mode matching the G diminish) the beam diameters at $z = 0$ just in front and just behind the incoupler are the same, such that:

$$\frac{I_{cav}(\rho, 0)}{I_{in}(\rho, 0)} = \frac{P_{cav}}{P_{in}} = G\ , \tag{2.21}$$

Replacing $P_{cav} = GP_{in}$ in Eq. 2.19. Close to the free space focus w_0, we may approximate the intensity distribution by,

$$\boxed{I_{cav}(\rho, z) = \frac{2P_{cav}}{\pi w_0^2} e^{-2\rho^2/w_0^2 - z^2/z_R^2}} \,, \tag{2.22}$$

where $z_R \equiv \pi w_0^2/\lambda$ is the Rayleigh range.

2.4.2 Dipole trap depth for one-sided pumping

With the intensity calculated in 2.22, we can now estimate the dipolar trap depth and the Rayleigh scattering rate for a given detuning:

$$V_{dip}(\rho, z) = \frac{3\pi c^2}{2\omega^3} \frac{\Gamma_{689}}{\Delta_a} I_{cav}(\rho, z) \qquad \text{and} \qquad \hbar\gamma_{sct}(\rho, z) = \frac{3\pi c^2}{2\omega^3} \frac{\Gamma_{689}^2}{\Delta_a^2} I_{cav}(\rho, z) \,. \tag{2.23}$$

We expect the dipole potential in the case of one-sided pumping:

$$V_{dip}^{\uparrow}(\mathbf{r}) = V_{0,dip}^{\uparrow} e^{(-2x^2-2y^2)/w_0^2 - z^2/z_R^2} \qquad \text{with} \qquad \boxed{V_{0,dip}^{\uparrow} = \frac{3\pi c^2}{2\omega_0^3} \frac{\Gamma_{689}}{\Delta} \frac{2P_{cav}}{\pi w_0^2}} \,, \tag{2.24}$$

yielding trap frequencies,

$$\boxed{\omega_r^{\uparrow} = \frac{2}{w_0}\sqrt{\frac{V_{0,dip}^{\uparrow}}{m}} \qquad \text{and} \qquad \omega_z^{\uparrow} = \frac{\sqrt{2}}{z_R}\sqrt{\frac{V_{0,dip}^{\uparrow}}{m}}} \,. \tag{2.25}$$

2.4.3 Dipole trap depth for double-sided pumping

In the case of two-sided pumping, the dipole potential in a ring cavity becomes,

$$V_{dip}^{\updownarrow}(\mathbf{r}) = \frac{3\pi c^2 \Gamma_{689}}{2\omega^3 \Delta_a} \left| e^{\imath kz} \sqrt{I_{+,cav}(\rho, z)} + e^{-\imath kz} \sqrt{I_{-,cav}(\rho, z)} \right|^2 \,, \tag{2.26}$$

where $\sqrt{I_{\pm}} \propto \mathcal{E}^{\pm}$ is the electric field amplitude.Rewriting 2.26

$$\begin{aligned} V_{dip}^{\updownarrow}(\mathbf{r}) &= \frac{3\pi c^2 \Gamma_{689}}{2\omega^3 \Delta_a} \frac{2}{\pi w_0^2} e^{-2\rho^2/w_0^2} \left| e^{\imath kz} \sqrt{P_{+,cav}} + e^{-\imath kz} \sqrt{P_{-,cav}} \right|^2 \\ &= \hbar U_0 e^{-2\rho^2/w_0^2} |e^{\imath kz}\alpha_+ + e^{-\imath kz}\alpha_-|^2 \\ &= \hbar U_0 e^{-2\rho^2/w_0^2} (e^{-2\imath kz}\alpha_+^*\alpha_- + e^{2\imath kz}\alpha_+\alpha_-^* + |\alpha_+|^2 + |\alpha_-|^2) \,. \end{aligned} \tag{2.27}$$

Writing $\alpha_{\pm} = |\alpha_{\pm}|e^{\pm\imath\phi}$, we get,

$$\begin{aligned} V_{dip}^{\updownarrow}(\mathbf{r}) &= \hbar U_0 e^{-2\rho^2/w_0^2} (2|\alpha_+||\alpha_-| \cos(2kz + 2\phi) + |\alpha_+|^2 + |\alpha_-|^2) \\ &\overset{\alpha_+ = \alpha_-}{\longrightarrow} 4\hbar U_0 e^{-2\rho^2/w_0^2} \cos^2(kz + \phi) \,. \end{aligned} \tag{2.28}$$

Finally,

$$V_{dip}^{\updownarrow}(\mathbf{r}) = V_{0,dip}^{\updownarrow} e^{-2\rho^2/w_0^2} \cos^2 \tfrac{kz}{2} \tag{2.29}$$

with

$$V_{0,dip}^{\updownarrow} = \frac{3\pi c^2}{2\omega_0^3}\frac{\Gamma_{689}}{\Delta}\frac{2(\sqrt{P_{cav,+}}+\sqrt{P_{cav,-}})^2}{\pi w_0^2} = \frac{3\pi c^2}{2\omega_0^3}\frac{\Gamma_{689}}{\Delta}\frac{8\sqrt{P_{cav,+}P_{cav,-}}}{\pi w_0^2 C_{sw}} \ , \tag{2.30}$$

where we introduced the standing wave contrast,

$$C_{sw} \equiv \frac{4\sqrt{P_+P_-}}{\sqrt{P_+}+\sqrt{P_-}} \ . \tag{2.31}$$

In the limit of symmetric pumping, we can simply set $P_+ = P_-$ and $C_{sw} = 1$.

Similarly to the one-sided pumping case, a harmonic approximation for the spatial intensity distribution yields the oscillation frequencies,

$$\boxed{\omega_r^{\updownarrow} = \frac{2}{w_0}\sqrt{\frac{V_{0,dip}^{\updownarrow}}{m}} \quad \text{and} \quad \omega_{lat}^{\updownarrow} = k\sqrt{\frac{V_{0,dip}^{\updownarrow}}{2m}}} \ . \tag{2.32}$$

2.4.4 Atoms trapped in the dipolar potential created by the cavity

After cooling the atoms to recoil temperatures, and after fine-tuning and control of the cavity parameters, we were ready to trap atoms in the cavity mode. Normally, experiments on cold atoms that confine them in a dipolar potential, use a high-power laser and control the mode matching between the atomic cloud and the trap by just adjusting the dipolar beam's position. That implies that the cloud is formed in a specific position and the beam path is superimposed on the cloud's location by just mechanical control of the optics that define the path.

Our setup, on the other hand, uses a cavity to create the trap. This limits the spatial interaction to the mode volume, which can be located at any distance ($\Delta\hat{x}$ or $\Delta\hat{y}$) from the Red-MOT final position. Remembering that the waist of our cavity mode is $w_{cav} = 60\mu$m and the size of our red cloud is $\sigma_x \approx 50\mu$m, which makes the overlap quite sensitive.

2.4.5 Coils to move the atomic cloud position.

In order to overcome this situation we modified our setup by adding offset coils in the $\hat{\mathbf{x}}$ and $\hat{\mathbf{y}}$ directions. Specifically, we implemented this as an offset of the Red-MOT magnetic gradient, and in that way, we were able to move the position of the atoms to match the cavity mode. The magnetic field component introduced for the offset coils is related to the cloud minimum for:

$$\Delta_x = \frac{B_0}{\partial B/\partial x} \tag{2.33}$$

Where B_0 is the value of the magnetic field produced by the coil.

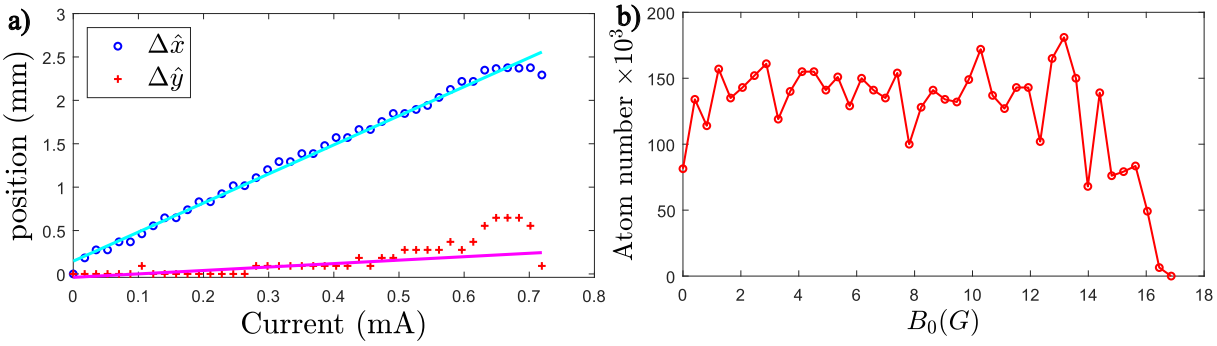

Figure 27 – Characterizations of the displacement coils on the $\hat{x}$ direction. a) While we increase the current of the coils the red cloud displaces linearly, correspondingly with the red MOT gradient. b) The number of atoms measured from the cloud decreases drastically when the position changes further than the beam's waist/2.

Source: By the author.

A calibration of the distance at which the trap forms as a function of the magnetic field in the $\hat{\mathbf{x}}$ coils is presented in 27 (a), together with the displacement measured for the $\hat{\mathbf{y}}$ axes as seen from the camera.

By measuring the displacement of the cloud at different values of current circulating through the coils and comparing this with the gradient necessary for the red MOT ($\partial B_{red} = 7$ G/cm) we could calibrate the linearity of the movement performed by means of the coils. Figure 27 (b) shows how the atom number in the trap diminishes when the displacement goes beyond the trapping region created by the retro-reflected beams of the MOT. 27 (b) the cloud displacement is visible, together with a diminish in contrast on the cloud due to the lowering in the number of atoms across the scan. In that way, we managed to scan the $\hat{\mathbf{x}}$ axis, and by changing the direction of the current passing through the coils we could also scan in the opposite direction. A second coil to perform movement of the cloud in the $\hat{\mathbf{z}}$ axis was also necessary. Characterizations and linearity of the $\hat{\mathbf{z}}$ coil will not be presented since the behavior is similar to the $\hat{\mathbf{x}}$ setup. Nonetheless, it is important to notice that after dynamically optimizing the alignment of the MOT beams and scanning the $\hat{\mathbf{x}}$ and $\hat{\mathbf{z}}$ magnetic field offsets we were able to see the interaction of the atomic cloud with the trap. That means, we saw atoms entering the cavity mode. [‡]

From here on the sequence used to perform the trapping of the atoms in the cavity includes the ramping of the $\hat{\mathbf{x}}$ magnetic field offset as a means to introduce the red-MOT into the cavity trap, see fig.28.

Finally, we were able to capture atoms in the mode, by pumping both sides of the cavity at a specific Intensity on each side. This was achieved by varying the amplitude

‡ The first signal observed of the atom-cavity interaction was performed using a $\Delta = -1000$ MHz and a trap depth of $V_{dip}^{\uparrow} = 1$ mK in the one side pumping geometry.

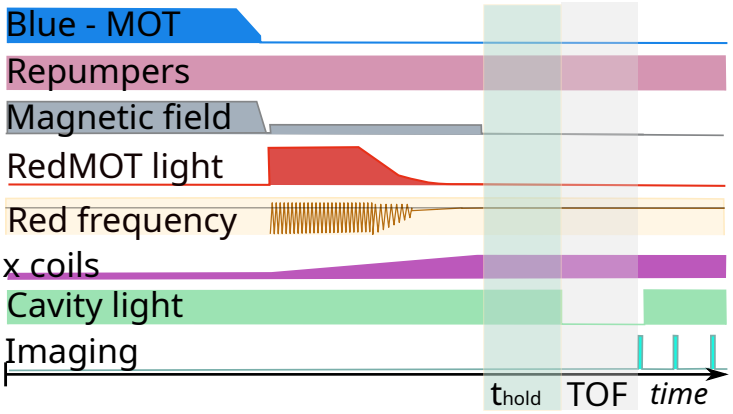

Figure 28 – Time sequence for introducing the red cloud inside of the Cavity mode. Analogous to the scheme already presented for the blue cloud the time is not at scale, further details can be found in the main text.

Source: By the author.

of the radio frequencies that feed the AOMs shown in 29(c) independently. Nonetheless, only one of the arms intensity effectively varies since the light of the other arm that feeds the cavity is used to create the locking signal to control the cavity length. Turning off the cavity locking light for a time longer than 5 ms implies a loss of the cavity locking signal[§].

Figure 29 shows the difference in the trapping potential when we use the cavity through (a) one-sided pumping or (b) two-sided pumping. A schematic of the setup followed for this measurement can be seen in 29(c). The two-side pumping configuration has the behavior of a lattice for the atoms in the $\hat{\mathbf{y}}$ direction, since holds them in the lattice sites at the position at which the cloud entered, avoiding them to fall due to gravity. It is possible to appreciate in Fig. 29(a) how the atoms that enter into the potential fall through the tube, the angle formed by the cavity mode can be compared with the direction of gravity (the g direction is measured by letting the Red-MOT fall for gravity with different TOF). With the help of these images, we were able to determine the angle of the tilting with respect to gravity in our cavity. The result gave us $\alpha = 12.3°$. In order to make our calculations easier and avoid misinterpretation of the data measured through absorption imaging, we implemented a rotation of the camera. The new images extracted from the camera now have a 12.3° difference in the vertical direction (The camera is aligned with the cavity mode and not with gravity).

This change in the system, see figure 30, allow us to analyze properly the cloud behavior in the cavity. The descriptions of our red cloud (outside of the cavity) are not affected. Figure 31 shows step-by-step the introduction of the red MOT into the cavity mode, with the new camera configuration. From left to right we change the magnetic offset created by the displacement coils to the center of the red MOT. Subfigure: a) The

§ We solved this issue by using a circuit of *sample and hold* developed using a LN398N operational amplifier.

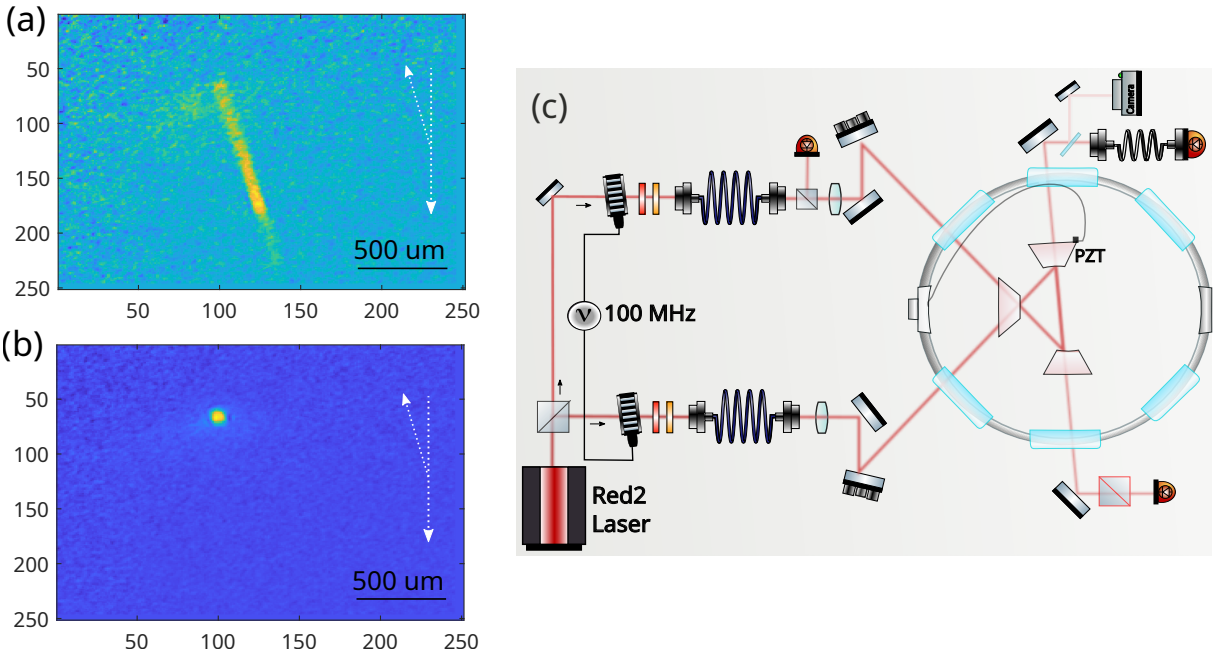

Figure 29 – Absorption images of the atoms entering in the dipolar trap a) One-sided pumping trap, b) Both-sided pumping trap. The white arrows represent the cavity mode direction and gravity. c) Experimental setup used to perform the measurements shown in this chapter

Source: By the author.

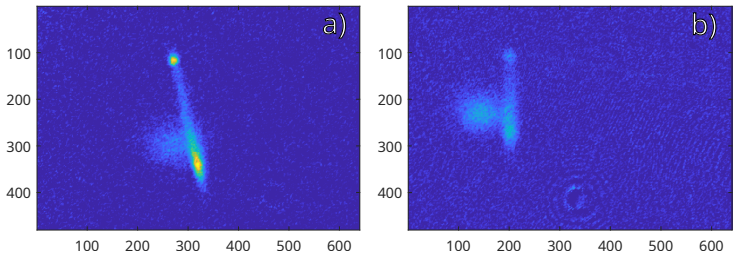

Figure 30 – Comparison between the absorption images taken with the camera a) aligned with the gravity and b) aligned with the cavity mode direction.

Source: By the author.

red MOT. b[¶], c[‖], d) The red cloud entering the unidirectionally pumped cavity e) Cavity cloud trapped in the bidirectionally pumped cavity, the atoms that didn't enter the cavity trap fall for gravity (directed at 12° of the cavity mode) due to the turn off of the red MOT field and beams.

The atoms inside of this conservative trap can now be studied as a function of the trap parameters, that is I and Δ.

¶ "Life imitates art far more than art imitates life ", Oscar Wilde

‖ Dali's art, that resembles 'La persistencia de la memoria' from Salvador Dalí

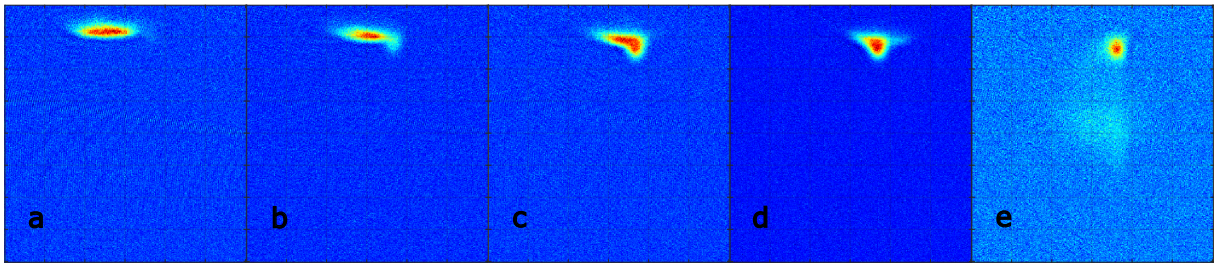

Figure 31 – Step by step of the Red cloud entering the cavity trap for decreasing the current in the displacement coils. a) The red cloud at TOF= 2 ms; b,c,d) unidirectional pumping of the cavity light. e) bidirectional pumping, creating a standing wave that avoids the cloud from falling for gravity, TOF= 2 ms, T_{hold} = 4 ms, corresponding TOF of the atoms that didn't enter the trap TOF_{redMOT} = 6 ms.

Source: By the author.

2.5 The cavity trap characterization

2.5.0.1 The lifetime of the atoms inside of the cavity trap

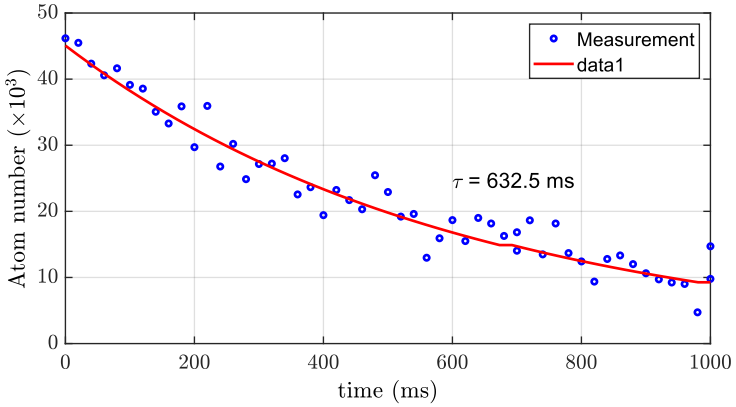

Figure 32 – Lifetime measurement of the atoms inside of the dipolar trap created in the cavity mode. The red line on top of the experimental data is an exponential fit used to extract the time constant.

Source: By the author.

Figure 32 shows the atoms number in the trap as a function of the trapping time (t_{hold}) for a trap realized with both side pumping schemes. The potential height of the trap for this measurement was $V_{dip}^{\updownarrow} = 425\ \mu$K and the detuning from the resonance was $\Delta = -3.8$ GHz.

2.5.0.2 Trap vs Frequency

Figure 33 shows the behavior of the cloud for different potential depths, as the parameter varying was the detuning of the trap. The measurements were carried out by fixing I and varying the frequency value at which cavity trap is stabilized to the red of

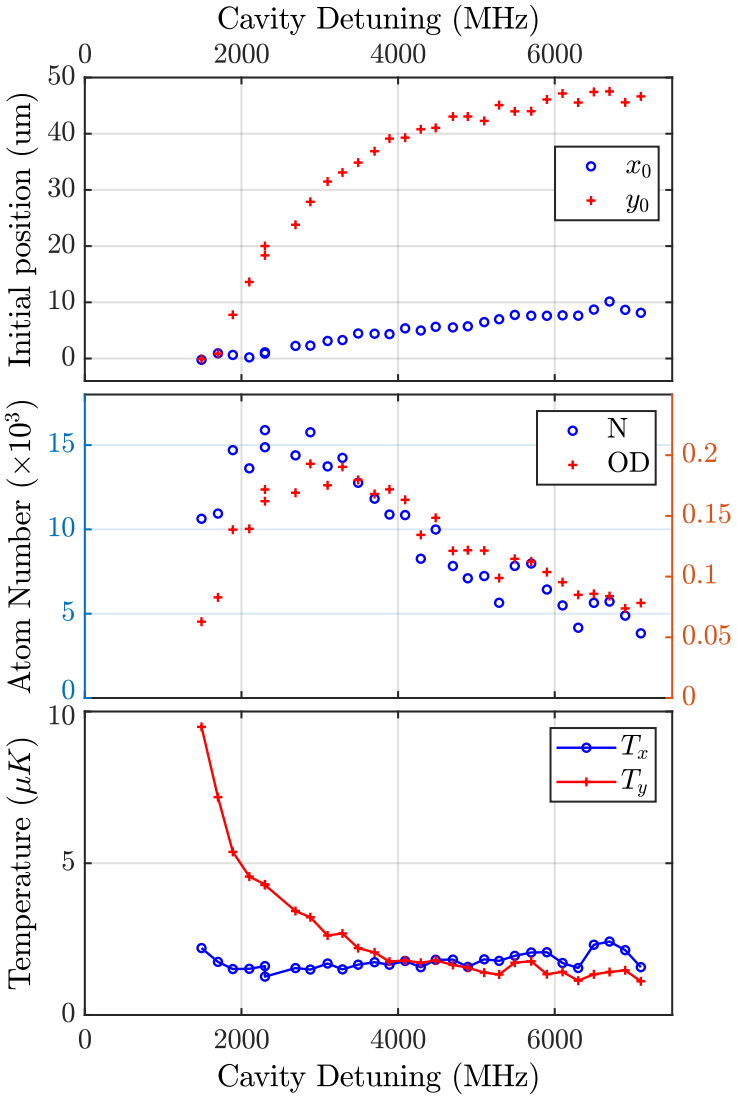

Figure 33 – Studies of the trapping of atoms as a function of the detuning for both sides pumped at fixed I. (a) The position of the atoms, as extracted from the fitting of our absorption imaging. (b) The atom number and the analogously the optical density dependence. (c) The temperature, measured at each fitting direction, as a function of the detuning of the cavity from the resonance.

Source: By the author.

the atomic transition. This is translated to a variation of $V_{dip}^{\updownarrow} = 315\mu\text{K} \longrightarrow 50\mu\text{K}$ for $\Delta = -1500\text{MHz} \longrightarrow -7200\text{MHz}$

In Subfigure (a) The position change suggests an intensity imbalance between the trap beams below 2500 MHz, above this value, the position of formation of the cold cloud stabilize, to the same position of the red cloud before entering the trap. We have seen shot to shot variations of the position of less than 2 pixels (3.7μm), for monitoring the evolution of the cloud position as a function of the trap holding time.

The diminishing of the atom number in sub-figure (b), for detuning lower than 2500 MHz, implies a heating process, since the atoms are kicked out of the potential.

This also suggests an imbalance in the intensity of the beams. After 4000 MHz the atom number starts to diminish, and this is related to the hot atoms now escaping the trap because the trap is shallower.

Fig 33c shows the temperature measured for the cloud as a function of the potential height. We see two curves, denoted as T_x and T_y that refer to the temperature measured in the $\hat{x}$ or $\hat{y}$ axes of our imaging system, respectively. The temperature is measured by the spread of the cloud for a certain TOF (TOF = 5 ms).

Before entering the trap our cloud has temperatures of ≈ 1 nK. We see that this value changes dramatically after entering the trap, nonetheless, we can retrieve some interesting information from this behavior. First, we have to discuss the difference between the temperatures in the x and y directions, that for a harmonic trap inthermal equilibrium must be the same. The anharmonicity of the trap is sufficient to redistribute the atomic velocities across the dimensions via an-harmonic mixing, especially for values below $\Delta = 4000$ MHz. The observed large width in the y-direction cannot be interpreted as a temperature. For values of detuning higher than $\Delta = 4000$ MHz, the reliability of our measurement is reestablished since the trap becomes shallow. Nonetheless, we can have a good approximation of the cloud's velocity distributions by looking at the values measured within the x direction. The frequencies of the trap are lower for higher detuning. When looking at the temperature we also see that the atoms that remain after $\Delta > 5000$MHz already have a plateau behavior. The temperature diminishes for the shallow trap behavior, also confirmed by the atoms decrease, this means that for higher detuning the only atoms that remain in the trap will have a lower temperature because they couldn't escape the trap for Doppler shift or too many recoils. Suggesting to work** at these frequencies or further.

It's important to notice that the temperature of the cavity cloud at larger detuning ($T_{\Delta=6GHz} = 1.2\ \mu$K) is hotter than the temperature of the cloud in the red MOT($T_{redMOT} = 800$ nK). Therefore, even though the hotter atoms escape the trap for longer times (like evaporation), the trap itself is still too tight in the radial direction, and therefore the atoms oscillate as can also be confirmed by the periodic variation of the number of atoms with time.

2.6 Preliminary conclusions

This section resumed the description and stabilization of the cavity light modes as a far-detuned trap for the atoms.

- Stable control of the light to interact with the atoms inside of the cavity mode using a stabilization system with a DPLL lock scheme that can be tuned to ±6 GHz.

** search for Bloch oscillation.

- Accurate control and characterization of the bare cavity parameters
- Trap of atoms in a dipolar trap, on both side pumping scheme, meaning a 1D periodical lattice, as necessary to perform Bloch oscillations.
- Dipolar trapping of strontium atoms with a far-detuned laser from a narrow transition.

3 OBSERVATION OF BI-STABILITY IN A STRONGLY COUPLED ATOM-CAVITY SYSTEM

The previous chapter showed that our cavity can interact with the atoms by creating a dipolar potential at which the atoms are trapped. We want to describe in the following sections a more detailed understanding of the atom-cavity system, which is a great playground for studies of atom-light interactions. This chapter will pursue the signatures of the coupling among the Strontium atoms interacting with the modes of a ring cavity.

The interaction strength of an atom with a light field is measured by the atom-field coupling constant, which is precisely half the single photon Rabi frequency. The coupling strength is :

$$g \equiv \frac{d\mathcal{E}^{\rightarrow}(0)}{\hbar} = \sqrt{\frac{\mu^2\omega_c}{2\hbar\epsilon_0 V_m}} = \sqrt{\frac{3\pi\delta_{fsr}}{k^2 w^2}} \tag{3.1}$$

where $\mathcal{E}_1(0)$ is the electric field produced by a single photon inside the cavity mode volume V_m. An analogous version can be understood in terms of μ, the dipole matrix element of the transition*, ω_c the cavity detuning, and ϵ_0 the permeability constant. And analogously this can also be written in terms of the wavevector of the light inside the cavity k, the free spectral range δ_{fsr}, and the waist w of the cavity mode. This parameter can be understood as the strength of the synchronization between the atomic dipole oscillation and the cavity Rabi frequency. In other words, g represents the coupling of the atoms to the cavity field (solid angle of the cavity) instead of the free space.

Let's now introduce an important quantity that will allow us to measure the degree of correlation of the system. The cooperativity Υ is also known as the Purcell factor.

$$\Upsilon = \frac{2g^2}{\Gamma\kappa} \tag{3.2}$$

The cooperativity parameter of a cavity is defined as the rate at which an atom emits into the volume of a cavity mode normalized to the rate at which it would scatter into free space.

Collective cooperativity: The strong coupling regime of the CQED requires $\Upsilon > 1$ with a single atom, collective cooperativity is reached with N atoms if $\Upsilon > 1$. In this case, the atomic ensemble couples to the mode like a single 'super-atom', and the coupling strength is magnified to $g_N = g\sqrt{N}$

* the dipole matrix element is given by $\langle Fm_F| e\mathbf{r} |F'm'_F\rangle$, as a function of the hyperfine sublevels under interrogation. A simplified expression is given by the lifetime of the transition addressed as:

$$\frac{1}{\tau} = \frac{\omega_0^3}{3\pi\epsilon\hbar c^3}\frac{2J+1}{2J'+1}|\langle J| e(r) |J'\rangle|$$

With e the electronic charge and r the position operator.

3.1 Theoretical description

The starting point for the description of the atom-cavity light interaction is the open system Dicke Hamiltonian for N atoms interacting with two modes of an optical cavity. For two counter-propagating modes of a ring cavity it reads (the rotating wave approximation having been made),

$$\hat{H} = \hat{H}_{field} + \hat{H}_{pump} + \sum_{j=1}^{N}(\hat{H}_{atom} + \hat{H}_{atom:field}) \ , \tag{3.3}$$

with

$$\hat{H}_{atom}^{(j)} = -\Delta_a \hat{\sigma}_j^+ \hat{\sigma}_j^- = -\tfrac{\Delta_a}{2}(\mathbb{I}_2 - \hat{\sigma}_j^z) \tag{3.4}$$

$$\hat{H}_{field} = -\sum\nolimits_{\pm} \Delta_c \hat{a}_{\pm}^{\dagger}\hat{a}_{\pm}$$

$$\hat{H}_{pump} = -\sum\nolimits_{\pm} \imath\eta_{\pm}(\hat{a}_{\pm} - \hat{a}_{\pm}^{\dagger})$$

$$\hat{H}_{atom:field}^{(j)} = g\sum\nolimits_{\pm}(\hat{a}_{\pm}\hat{\sigma}_j^+ e^{\pm\imath k z_j} + \hat{a}_{\pm}^{\dagger}\hat{\sigma}_j^- e^{\mp\imath k z_j}) \ . \tag{3.5}$$

Here, $\Delta_a \equiv \omega - \omega_a$ with $\omega_a = c/\lambda_a$ being the atomic resonance frequency, and $\Delta_c \equiv \omega - \omega_c$ with $\omega_c = n\delta_{fsr}$ being a cavity resonance frequency. δ_{fsr} is the cavity's free spectral range and $n \in \mathbb{N}$. $\eta_{\pm}$ are the pump rates of the two counter-propagating modes, g the atom-field coupling strength (or single-photon Rabi frequency), and $g_N = g\sqrt{N}$ is the collective coupling strength. $\hat{\sigma}_j^+$, $\hat{\sigma}_j^-$, $\hat{\sigma}_j^z$ are the usual Pauli matrices applied to the j-th atom. We exclude *a priori* inter-atomic correlations, such as spin-squeezing. Finally, $\hat{a}_{\pm}$, $\hat{a}_{\pm}^{\dagger}$ are the usual photonic field operators for the counter-propagating modes.

The one-dimensional Hamiltonian 3.5 only contains the atomic location modulo the lattice constant k^{-1}, which excludes effects arising from periodic structures (such as optical lattices). Such effects may be taken into account in extended models, such as the coupled dipoles model or the transfer matrix model.(94–96)

Note also, that here, we do not treat the recoil $e^{\mp\imath k z}$ as a degree of freedom, but just as a parameter depending on the location of the atom. Decay processes can be considered in a master or in Heisenberg equations via jump operators, $\hat{L} = \hat{\sigma}^-$, $\hat{a}_+$, $\hat{a}_-$, describing decay processes occurring, respectively, at rates $\gamma_k = \Gamma,\ 2\kappa,\ 2\kappa$.Where we introduced the light-shift produced by a single off-resonant photon (U_0) and the Rayleigh scattering rate produced by a single photon,

$$U_0 \approx \frac{g^2}{\Delta_a} \qquad \text{and} \qquad \gamma_0 \approx \frac{g^2\Gamma}{\Delta_a^2} \tag{3.6}$$

An approximate analytic steady-state solution can be derived starting from the Heisenberg equations using the Hamiltonian 3.3 and the jump operators $\hat{L}$ neglecting all correlations. Using the abbreviations,

$$U_\gamma \equiv U_0 - \imath\gamma_0 \equiv \frac{g^2(\Delta_a + \imath\Gamma)}{\Gamma^2 + \Delta_a^2} \ , \tag{3.7}$$

and $\Delta_\kappa \equiv \Delta_c + \imath\kappa$, the result of the calculation, is,

$$\sum_j \frac{U_\gamma(\alpha_\pm + e^{\mp 2\imath k z_j})\alpha_\mp}{1 + 2(|U_\gamma|/g)^2|e^{\imath k z_j}\alpha_+ + e^{-\imath k z_j}\alpha_-|^2} = \Delta_\kappa \alpha_\pm - \imath\eta_\pm \ . \tag{3.8}$$

The expression 3.8 is the most general formula discussed here in the context of normal-mode splitting.

Let us now define the bunching parameter (b):

$$b_\pm \equiv \tfrac{1}{N}\sum_j e^{\pm 2\imath k z_j} \ . \tag{3.9}$$

That can be considered as the order parameter of the system, describing the coherence in the emission process. In the beginning, the phases (kz_j) are distributed randomly and $b \approx 0$ (more precisely, the RMS value of b is $1/\sqrt{N}$). When the atoms are grouped within an optical wavelength, the atoms' phases become correlated, and $|b|$ becomes close to unity(97), equivalent to an atomic density grating.

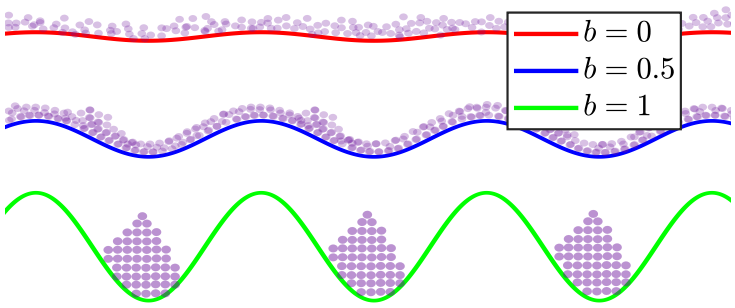

Figure 34 – Schematics illustrating redistribution of atoms (purple dots) from the initial random distribution to a periodic density grating. The density grating is ($b = 0$) initially shallow, but becomes deeper ($b = 1$) as a consequence of the interference between the laser beam and the backscattered light.

Source: By the author.

Now equation 3.8 can be simplified when we assume perfect bunching, that is: the atoms have already pre-organized in the bottom of the vibrational potential created by the cavity, $|b| = 1$ (see Fig 34).

$$\frac{NU_\gamma(\alpha_\pm + e^{\mp 2\imath k z}\alpha_\mp)}{1 + 2(|U_\gamma|/g)^2|\alpha_+ + e^{-2\imath k z}\alpha_-|^2} = \Delta_\kappa \alpha_\pm - \imath\eta_\pm \ . \tag{3.10}$$

The expression 3.8 can not be solved analytically except in some particular limits.

3.1.0.1 Weak excitation:

In the following, we will focus on the study of the case of strong excitation. We eill present in Sec. 3.1.1 the case of no bunching and arbitrary excitation.

On the other hand, for arbitrary bunching but in the limit of weak excitation, $U_\gamma|\alpha_\pm| \ll g$, we obtain,

$$(NU_\gamma - \Delta_\kappa)\alpha_\pm + Nb_\mp\alpha_\mp = -\imath\eta_\pm \ . \tag{3.11}$$

In that case, the field amplitudes can be decoupled,

$$\alpha_\pm \simeq -\imath\frac{\eta_\pm(NU_\gamma - \Delta_\kappa) - \eta_\mp NU_\gamma b_\mp}{(NU_\gamma - \Delta_\kappa)^2 - (NU_\gamma|b_\mp|)^2} \ , \tag{3.12}$$

Interestingly, in this regime, i.e. below saturation, the impact of (ordered or disordered) atomic distribution along the optical axis is entirely included in a single quantity, which is the bunching parameter $b_\pm$. Details of the atomic distribution only matter above saturation, where the exact formula 3.8 must be used.

From the field strengths 3.12 we can determine the transmissions of the probe light T_+ and of the backscattered light T_-,

$$T_\pm = \left|\frac{\kappa\alpha_\pm}{\eta_+}\right|^2 \ . \tag{3.13}$$

3.1.1 Strong excitation, the role of saturation

The validity of the analytic formula 3.12 is conditioned to weak excitation (below saturation) $g|\alpha_\pm| \ll |\Delta_a|, \Gamma$. Above this limit, we have to resort to numerical simulations. Now, our experiment is characterized by $g \gtrsim \Gamma$, that is, a single photon saturates the transition. Thus, approximating the cavity field by its steady-state value without atoms, $\alpha_\pm = \eta_\pm/\kappa$, we find for our experimental parameters,

$$\eta_\pm/\kappa \ll \frac{\Gamma}{g} \simeq 0.87 \ . \tag{3.14}$$

In our experiment this corresponds (with $\delta_{fsr} = 8.23\,\mathrm{GHz}$) to an intracavity power of,

$$P_\pm = \hbar\omega\delta_{fsr} \simeq 0.2\,\mathrm{nW} \ . \tag{3.15}$$

In our experiment, we typically measure transmitted light powers for the probe light of $P_{tr+} \approx 4\,\mathrm{nW}$. This is equivalent to intracavity light powers of $P_{cav+} \approx 13.82\mu\mathrm{W}$, or $P_{tr+}/(1 - R_{hr})$ with $R_{hr} = 0.9995$. For this power, with $\frac{2P_+}{\pi w_0^2}$, $I_s = \frac{g_1}{g_2}\frac{2\pi^2 c\hbar}{3\lambda^3}\Gamma$, $g = \frac{1}{\hbar}\mathcal{E}_1 d = \sqrt{\frac{3\Gamma\delta_{fsr}}{k^2 w_0^2}}$, and the parameters listed in Table 1, we estimate a saturation parameter of,

$$s = \frac{I_+}{I_s} = \frac{2(2g)^2|\alpha_+|^2}{\Gamma^2} \approx 250 \ . \tag{3.16}$$

3.1.1.1 Saturation-induced bistability

The steady-state expression 3.8 will generate bistable behavior. With the aim of deriving an analytic solution accounting for our experimental situation we study in the following two cases.

We solve the equation for the case of perfect disorder, see 3.1.2, which is the case when the atoms form a homogeneous cloud within cavity's mode volume. As it happens for example when a cloud is introduced in the cavity volume while pumped by only one direction.

We solved Eq. 3.8 for the case of perfect bunching, $b_\pm = 1$, which is the case when the atoms are arranged in an optical lattice. In both cases, we observe the bistable behavior of the solutions. And we verified that the perfect bunching leads to analogous conclusions of the homogeneous cloud with a modified atom number

3.1.2 Bistability for our case, the homogeneous clouds

In the case of a homogeneous cloud (no bunching $b_\pm = 0$) we may neglect backscattered light alltogether, $\alpha_- = 0$, and Eq. 3.8 simplifies to,

$$\frac{N\tilde{U}_\gamma \alpha_+}{1 + 2|\tilde{U}_\gamma|^2|\alpha_+|^2} = \tilde{\Delta}_\kappa \alpha_+ - \imath\tilde{\eta}_+ \ . \tag{3.17}$$

Resolving for α_+,

$$\boxed{\alpha_+ = \frac{\imath\tilde{\eta}_+}{\tilde{\Delta}_\kappa - \frac{N\tilde{U}_\gamma}{1+2|\tilde{U}_\gamma|^2 n}}} \ , \tag{3.18}$$

with $n \equiv |\alpha_+|^2$ yielding,

$$n = \frac{\tilde{\eta}_+^2(1 + 2|\tilde{U}_\gamma|^2 n)^2}{|\tilde{\Delta}_\kappa|^2(1 + 2|\tilde{U}_\gamma|^2 n)^2 - N(\tilde{U}_\gamma\tilde{\Delta}_\kappa^* + \tilde{U}_\gamma^*\tilde{\Delta}_\kappa)(1 + 2|\tilde{U}_\gamma|^2 n) + |N\tilde{U}_\gamma|^2} \ . \tag{3.19}$$

This expression can be written in terms of a third order polynomial,

$$0 = An^3 + Bn^2 + Cn + D \ , \tag{3.20}$$

with the coefficients,

$$A = 4|\tilde{\Delta}_\kappa|^2|\tilde{U}_\gamma|^4 \tag{3.21}$$

$$B = 4|\tilde{U}_\gamma|^2\left(|\tilde{\Delta}_\kappa|^2 - \tfrac{1}{2}N(\tilde{U}_\gamma\tilde{\Delta}_\kappa^* + \tilde{U}_\gamma^*\tilde{\Delta}_\kappa) - |\tilde{U}_\gamma|^2\tilde{\eta}_+^2\right) \tag{3.22}$$

$$C = |\tilde{\Delta}_\kappa|^2 - N(\tilde{U}_\gamma\tilde{\Delta}_\kappa^* + \tilde{U}_\gamma^*\tilde{\Delta}_\kappa) + |N\tilde{U}_\gamma|^2 - 4|\tilde{U}_\gamma|^2\tilde{\eta}_+^2 \tag{3.23}$$

$$D = -\tilde{\eta}_+^2 \ . \tag{3.24}$$

The roots of the cubic equation are given by,

$$R \equiv \sqrt[3]{36CBA - 108DA^2 - 8B^3 + 12\sqrt{3}A\sqrt{4C^3A - C^2B^2 - 18CBAD + 27D^2A^2 + 4DB^3}} \tag{3.25}$$

and

$$X_\pm \equiv \frac{R}{6A} \pm \frac{6AC - 2B^2}{3AR} \tag{3.26}$$

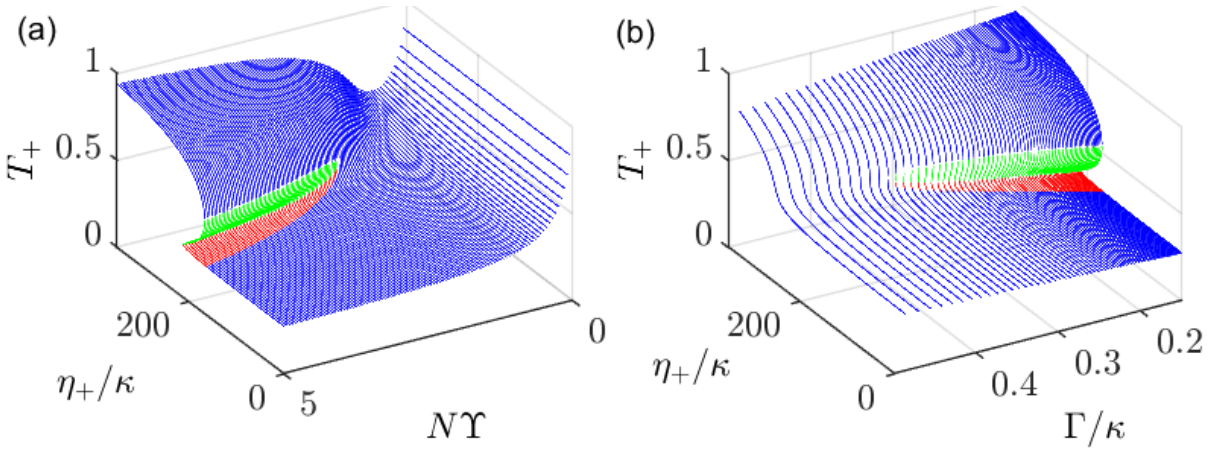

Figure 35 – Bistability induced by saturation as a function of η_+ and (a) varying the collective cooperativity $N\Upsilon$ and (b) the atomic transition linewidth $\Gamma' \equiv 4g^2/(N\Upsilon\kappa)$. The different colors denote three different transmissions $T_\pm$ obtained from the analytical solution of Eq. 3.8.

Source: By the author.

so that,

$$n_0 = X_- - \frac{B}{3A} \quad , \quad n_\pm = -\frac{1}{2}X_- - \frac{B}{3A} \pm \frac{\imath\sqrt{3}}{2}X_+ \ , \tag{3.27}$$

from which we obtain the roots $n = |\alpha_+|^2$ and the field amplitude from 3.18.

Discarding all solution $n \notin \mathbb{R}$ we obtain the diagram shown in Fig. 35.

3.1.2.1 Critical pump rate on resonance for homogeneous clouds and one-sided pumping

Let us now discuss the resonant case, $\Delta_c = 0 = \Delta_a$, that is, $\tilde{\Delta}_\kappa = \imath\kappa/g$ and $\tilde{U}_\gamma = -2\imath g/\Gamma$, with one-sided probing, $\eta_- = 0$. Using the definitions of the cooperativity and the single-photon saturation parameters,

$$\Upsilon \equiv \frac{4g^2}{\Gamma\kappa} \qquad \text{and} \qquad s_1 \equiv \frac{2\Omega_1}{\Gamma} = \frac{8g^2}{\Gamma^2} \ , \tag{3.28}$$

Eq. 3.18 becomes,

$$\alpha_+ \simeq \frac{\eta_+}{\kappa}\frac{ns_1 + 1}{\frac{1}{2}N\Upsilon + ns_1 + 1} \ . \tag{3.29}$$

From this formula we can easily evaluate the relative importance of collective cooperativity and saturation. Since $N\Upsilon \gg 1$, we get below saturation,

$$\alpha_+ \xrightarrow{n\to 0} \frac{2\eta_+}{\kappa}\frac{1}{N\Upsilon} \ , \tag{3.30}$$

that is, the excitation of the cavity field is heavily suppressed by the normal-mode splitting. At high saturation,

$$\alpha_+ \xrightarrow{n\to\infty} \frac{\eta_+}{\kappa} \ , \tag{3.31}$$

the cavity becomes fully transparent.

For intermediate saturation in the large collective cooperativity limit we evaluate the coefficients 3.24 of the cubic equation,

$$A = \frac{16\kappa^3}{\Gamma^3}\Upsilon \tag{3.32}$$

$$B = \frac{4\kappa^2}{\Gamma^2}(1 + 2N\Upsilon - \Upsilon^2\tilde{\eta}_+^2) \simeq \frac{4\kappa^2}{\Gamma^2}\Upsilon(2N - \Upsilon\tilde{\eta}_+^2) \tag{3.33}$$

$$C = \frac{\kappa^2}{g^2}\left[1 + N\Upsilon + (\tfrac{1}{4}N^2 - \tilde{\eta}_+^2)\Upsilon^2\right] \simeq \frac{\kappa}{\Gamma}\Upsilon(N^2 - 4\tilde{\eta}_+^2) \tag{3.34}$$

$$D = -\tilde{\eta}_+^2 \ . \tag{3.35}$$

The cubic equation 3.20 has only one solution if for some coefficient E,

$$n^3 + \tfrac{B}{A}n^2 + \tfrac{C}{A}n + \tfrac{D}{A} = (n - E)^3 \ . \tag{3.36}$$

In other words,

$$\tfrac{B}{A} = -3E \quad , \quad \tfrac{C}{A} = 3E^2 \quad , \quad \tfrac{D}{A} = -E^3 \ . \tag{3.37}$$

That is, we have the triple root $n = E = -\frac{B}{3A}$ provided that,

$$BC = 9AD \qquad \text{and} \qquad B^2 = 3AC \ . \tag{3.38}$$

Inserting the coefficients into the first expression yields,

$$0 = \tilde{\eta}_+^4 + \left(\frac{9}{\Upsilon^2} - \frac{2N}{\Upsilon} - \frac{N^2}{4}\right)\tilde{\eta}_+^2 + \frac{N^3}{2\Upsilon} \tag{3.39}$$

$$\simeq \tilde{\eta}_+^4 - \frac{N^2}{4}\tilde{\eta}_+^2 + \frac{N^3}{2\Upsilon} \tag{3.40}$$

$$\Longrightarrow \qquad \tilde{\eta}_+^2 \simeq \frac{N^2}{8} \pm \frac{N^2}{8}\sqrt{1 - \frac{2}{N\Upsilon}} \simeq \frac{N^2}{4} \tag{3.41}$$

and into the second expression,

$$0 = \tilde{\eta}_+^4 + \left(\frac{12}{\Upsilon^2} - \frac{4N}{\Upsilon}\right)\tilde{\eta}_+^2 + \frac{N^2}{\Upsilon^2} \tag{3.42}$$

$$\simeq \tilde{\eta}_+^4 - \frac{4N}{\Upsilon}\tilde{\eta}_+^2 + \frac{N^2}{\Upsilon^2} \tag{3.43}$$

$$\Longrightarrow \qquad \tilde{\eta}_+^2 \simeq \frac{N}{\Upsilon}(2 \pm \sqrt{3}) \ . \tag{3.44}$$

This means, that for low cooperativity but high collective cooperativity the instability occurs when the pump rate and the collective cooperativity satisfy,

$$2\eta_+ < Ng \qquad \text{and} \qquad N\Upsilon > 8 + 4\sqrt{3} \ . \tag{3.45}$$

For our cavity, with $g = (2\pi)\ 9.1\,\text{kHz}$ and $N = 10^5$, this means, $\eta_+ \approx 268\kappa$. The cooperativity satisfies the above condition provided that $\Gamma < 0.251\kappa$, which is satisfied for

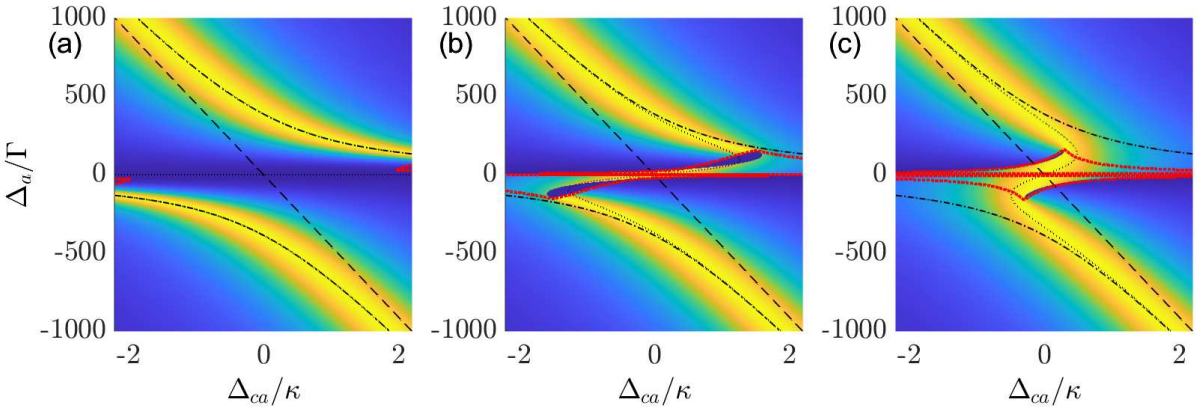

Figure 36 – Normal-mode spectra $T_\pm$ calculated using Eq. 3.29 for various pump rates (d) $\eta_+ = 1\Gamma$, (e) 160Γ, and (f) 250Γ and all other experimental parameters as specified in the text. The anti-diagonal black dashed lines show the mode of an empty cavity ($N = 0$). The dash-dotted black lines are calculated from 3.9, and the dotted black lines from 3.10 using a saturation broadening estimated from $\Omega_\eta = 2g\eta_+/\kappa$. The bistable region is delimited by a red dotted line.

Source: By the author.

our intercombination transition. Alternatively, for a given decay rate of $\Gamma = (2\pi)\ 7.6\,\mathrm{kHz}$ the atom-field coupling strength should be higher than $g > 0.0002\kappa$, which is the case for our cavity.

The results obtained for the perfect and the zero bunching case are similar. Interestingly the cubic equations for the zero bunching case can be obtained from the perfect bunching case by simply substituting $N \longrightarrow \frac{N}{2}$.

3.1.2.2 Hand-waved equation for describing our experimental results

In the following, we will propose and discuss a simplified approach, whose theoretical foundation is questionable, but which nevertheless seems to be capable of explaining experimental observations, and it relies not far from the exact solution result presented in the previous section. The approach consists in applying the adiabatic elimination procedure of the atomic degrees of freedom, as successfully done in the low saturation regime. That is, we accept the validity of the steady-state solution 3.12 also in the high saturation regime with the only amendment that atomic polarizability is saturation-broadened. That is, we simply generalize the Lorentzian 3.8 such as to include saturation, analogous to a light power that would be in an empty resonantly driven cavity ($N = 0$, $\Delta_c = 0$),

$$U_\gamma \equiv U_0 - \imath\gamma_0 \equiv \frac{g^2(\Delta_a + \imath\frac{\Gamma}{2})}{\Delta_a^2 + \frac{\Omega^2}{2} + \frac{\Gamma^2}{4}} \quad \text{with} \quad \Omega_\eta = \frac{2g\eta_+}{\kappa}\ . \tag{3.46}$$

The central result emanating from this ansatz is transmission profiles $T_+(\Delta_{ca}, \Delta_a)$ such as the one shown in Fig. 37(d). It reveals many interesting features, which we will

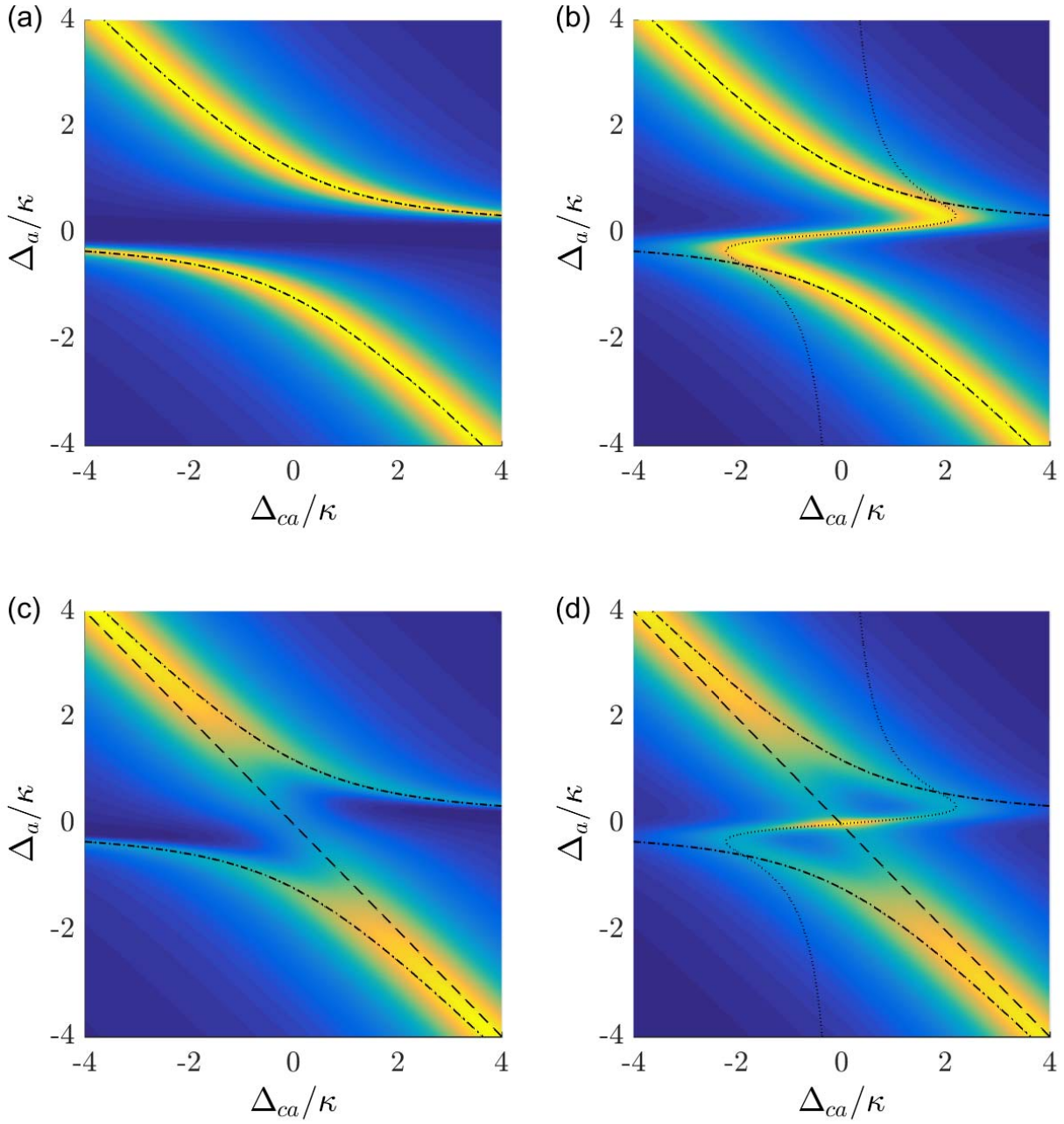

Figure 37 – Normal-mode splitting $T_\pm$ calculated using Eq. 3.12 with $\Gamma = 0.0022\kappa$, $g = 0.0027\kappa$, $N = 100000$, and $b_\pm = 1$. Furthermore, for (a) $\Omega = 0$, $\eta_- = \eta_+$; the dashed line is calculated from 3.48. (b) $\Omega = 200\Gamma$, $\eta_- = \eta_+$; the dispersive dashed line is calculated from 3.49. (c) $\Omega = 0$, $\eta_- = 0$; the anti-diagonal dashed line is calculated from 3.50, and (d) $\Omega = 200\Gamma$, $\eta_- = 0$.

Source: By the author.

try to understand in the following.

(i) We observe an 'avoided crossing' as it is known from standard atom-cavity experiments. In order to isolate this feature, we calculate from Eq. 3.12 the transmission

profile T_+ for low saturation $\Omega \approx 0$ and symmetric pumping $\eta_- = \eta_+$,

$$\alpha_\pm = \frac{\imath\eta_\pm}{2NU_0 - \Delta_c - \imath\kappa} \ , \tag{3.47}$$

and plot it in Fig. 37(a). The ridge for the normal-mode splitting simply follows from $0 = \frac{d}{d\Delta_a}\left|\frac{\alpha_\pm}{\eta_\pm}\right|^2$ and yields,

$$\Delta_a = -\tfrac{1}{2}\Delta_{ca} \pm \sqrt{\tfrac{1}{4}\Delta_{ca}^2 + 2Ng^2} \ . \tag{3.48}$$

(ii) The same calculation but for high saturation, $\Omega \approx 200\Gamma$, generates the dispersive profile shown in Fig. 37(b). Near resonance, $|\Delta_a| < \Gamma$, this profile can physically be understood as the Stark-shift generated by atom-light interaction at a given detuning Δ_a. The role of the cavity is reduced to filtering the resonant light so that resonance is observed at $\omega_c = \omega_a - U_0$, i.e. the ridge is well described by,

$$\Delta_{ca} = \frac{g^2\Delta_a}{\Delta_a^2 + \frac{\Omega^2}{2} + \frac{\Gamma^2}{4}} \ . \tag{3.49}$$

(iii) In the absence of atoms the cavity's resonance frequency obviously appears at $\omega = \omega_c$, i.e.,

$$\Delta_{ca} = -\Delta_a \ . \tag{3.50}$$

In Eq. 3.12 this branch can be isolated for one-sided pumping ($\eta_- = 0$) by simply setting the collective coupling strength $g\sqrt{N} \approx 0$. The corresponding profile is an anti-diagonal straight line dimly visible in Fig. 37(c). For stronger coupling strength ($g\sqrt{N} \gtrsim \kappa$), we recover the three-modal normal mode splitting. The anti-diagonal ridge appears only, when the ring cavity is pumped in one direction (the normal-mode spectrum taken as a vertical cut, e.g. along $\Delta_{ca} = 0$, shows three peaks).

In summary, the 'highway crossing' shaped profile observed in Fig. 37(d) is understood as the intersection of the above three branches. Also note, that the horizontal branch of the dispersive ridge corresponds to enhanced spontaneous emission. Furthermore, the width of the central feature along the Δ_{ca} axis is given by κ, the width along the Δ_a-axis by Ω.

3.2 Normal mode splitting Measurement

Fig. 36 shows an avoided crossing upon varying both: laser and cavity. To calculate the transmission spectrum observed, we ramp the pump laser while monitoring the light power leaking through one of the high reflectors, for different values of the cavity resonance.

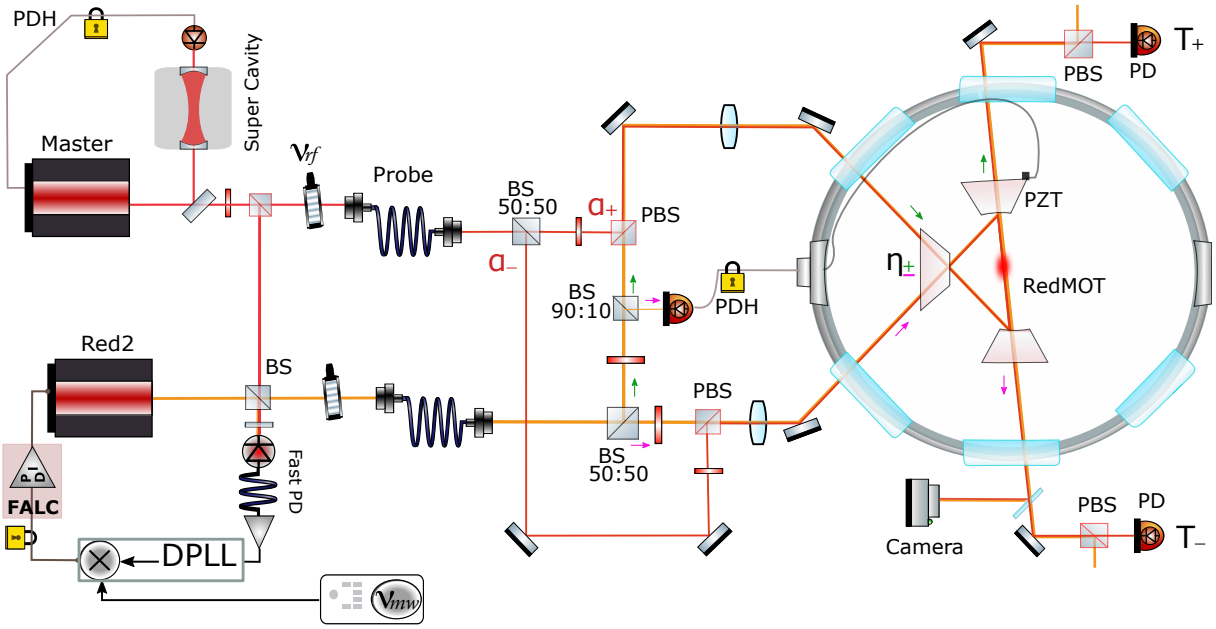

Figure 38 – Scheme of the lasers controlling the atom-cavity interaction. Laser 1, which is tightly locked to a reference cavity via a Pound-Drever-Hall servo (PDH), is tuned close to the narrow atomic resonance (Δ_a). It serves for cooling the atomic cloud (red MOT) and for driving one or two of the counter-propagating modes ($\alpha_\pm$) of the ring cavity formed by three mirrors, the input coupler (IC), and two high reflectors (HR). The transmission through the high reflectors ($T_\pm$) is recorded. A second laser (laser 2) is phase-locked (DPLL) to laser 1 at 4 GHz below the atomic resonance. In contrast to laser 1, its intensity is high. Overlapped with laser 1 and also coupled into one or two counter-propagating modes of the ring cavity it generates an optical dipole potential for the atoms. Transmission spectra showing normal mode splitting are obtained by ramping ν_{rf} and/or ν_{mw}.

Source: By the author.

3.2.1 Optical setup and sequence

In order to measure the atoms-cavity interaction we perform trials with the experimental setup shown in figure 38 and we measure the transmission of the cavity probe. Notice how the experimental scheme of figure 38 differs from the one shown in the previous chapter since this new setup offers more stability for the standing wave inside the cavity[†] This setup also allows us to inject light from the probe by using the other polarization mode of the cavity.

[†] Since each mode of the cavity is pumped by individual paths the phase difference of the light modes can be measured as the temporal evolution of the interference of the transmitted light. Differences in the phase can be attributed to thermal and mechanical noise introduced via the devices that supply the laser light to enter the cavity. The setup shown in fig. 38 ensures a shorter laser path difference between pumps by separating the beams right before entering the cavity.

In short, the cold cloud of Sr with about 10^6 atoms is cooled to temperatures around $1\,\mu$K and transferred into the mode volume of a ring cavity. The atomic cloud is confined to the mode volume by optical dipole potential formed by two laser beams coupled into counter-propagating TEM_{00} modes of the ring cavity (laser 2 in Fig. 38) under p-polarization, where the finesse of the cavity is low ($F \approx 100$). The length of the ring cavity is stabilized to this laser 2 via a Pound-Drever-Hall servo electronics. Laser 2, which is tuned 4 GHz to the red of the strontium resonance is, in turn, locked via a digital phase-locked loop (DPLL) to a second laser (laser 1 in Fig. 38), which itself is stabilized to a stable super cavity and operated near the strontium resonance.

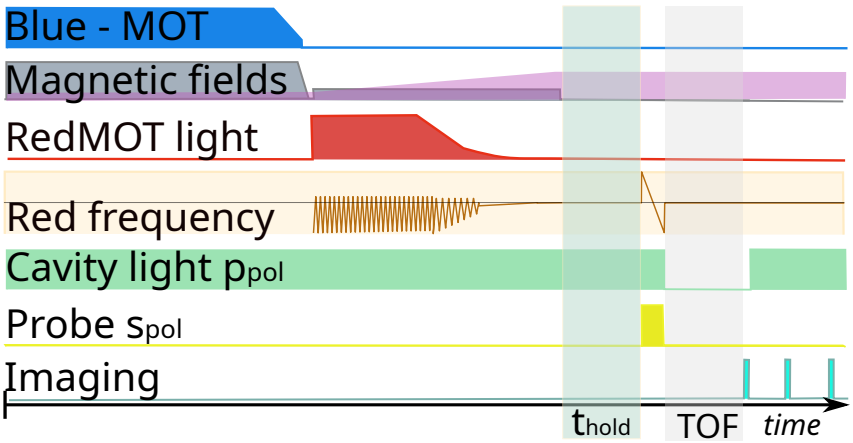

Figure 39 – Time sequence for probing the normal mode splitting. Analogous to the schemes already presented, the time is not at scale, further details can be found in the main text.

Source: By the author.

Laser 1 serves for the last cooling stage (red MOT) and also as a probe for the atom-cavity interaction. In this latter role, the light of laser 1 is passed through AOMs, driven by tunable radio-frequencies ν_{rf} and permitting to ramp the laser frequency ω with respect to the atomic resonance, $\omega = \omega_a + \Delta_a$, and with respect to the cavity resonance, $\omega = \omega_c + \Delta_c$. On the other hand, we can control the detuning between the cavity and the atomic resonance, $\Delta_a - \Delta_c$, via the microwave-frequency ν_{mw} of the DPLL.(8) The near-resonant probe light is matched to the beams of laser 2 and coupled from one (η_+) or from both (η_-) counter-propagating directions under s-polarization, where the finesse of the cavity is high ($F \approx 1500$) into a TEM_{00} mode of the ring cavity. The probe light transmitted from both modes through the high-reflecting mirrors (HR) is filtered by a polarizing beam splitter, coupled into optical fibers, and monitored. A typical transmission spectrum in the one-side pumping configuration ($\eta_- = 0$) is exhibited in Fig. 40. In practice, the sequence used to measure a spectrum is like the one shown in figure 39. Notice that the frequency of the probe is scanned with the same tool that creates the red MOT modulation.

3.2.2 Experimental observations

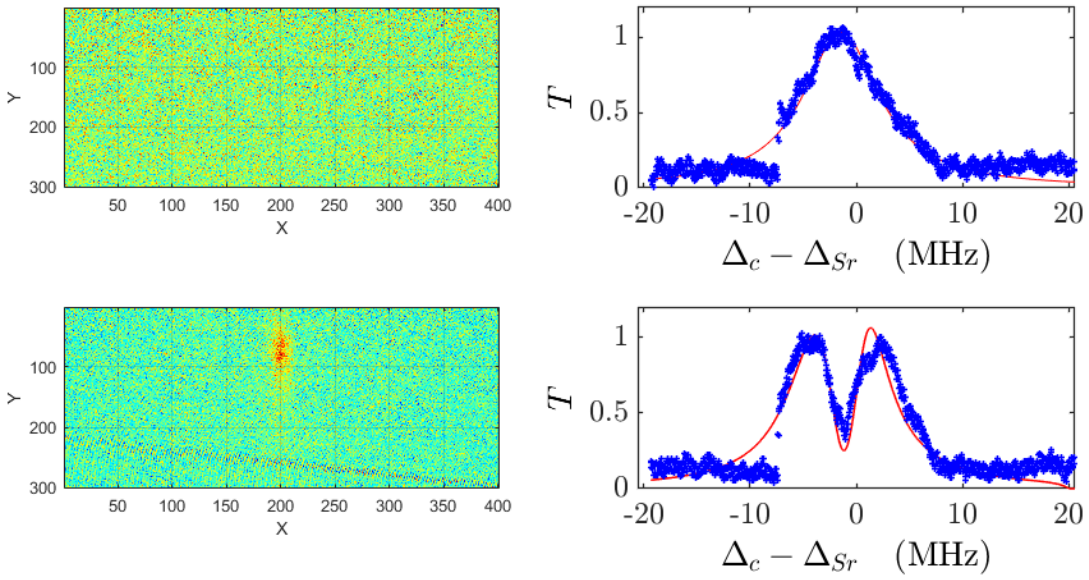

Figure 40 – Measured transmission spectra (blue crosses) of the ring cavity T_+ (b) without and (d) with atoms. The curve in (d) shows a typical normal-mode splitting. The red lines are fits using (a) a Lorentzian profile and (b) the normal mode expression 3.12

Source: By the author.

The different spectra shown in figure 40 were taken with the empty cavity (b) and with the cavity loaded with $N \approx 80000$ atoms (d). Figure 40 (a) and (c) are the respective TOF images after the measurement was performed. As predicted from our calculations the third peak of the NMS has been observed [‡], see Fig.41, notice that out third peak is described in the context of the saturated regime.

3.2.3 Discussion

When a full scan of the cavity length is performed, i.e. varying the DPLL frequency around the cavity resonance parallel to the atomic transition (Δ_c), an 'avoided crossing' map can give us analogous information to the simulations presented in the previous sections.

In figure 41, we present experimental measurements of the NMS of our ring cavity performed with the cavity loaded with $N = 120000$ atoms.

[‡] The experimental observation of the three peaks' normal mode splitting was previous to the theoretical analysis and the simulations developed to explain this phenomenon. Fun fact, we expend a significant amount of time improving the stabilization of our lasers and cavity to rule out the occurrence of the third peak due to experimental imperfections or technical errors.

(dot-line . − .−) The normal-mode splitting ad descrived by equation 3.48

(traced line − − −) is the cavity's resonance frequency shifted by an amount Δ_{strk} corresponding to the Stark shift experienced by the atoms.

(dotted line ....) the corresponding ridge calculated by equation 3.49 with the Rabi frequency extracted from our fit of the spectra.

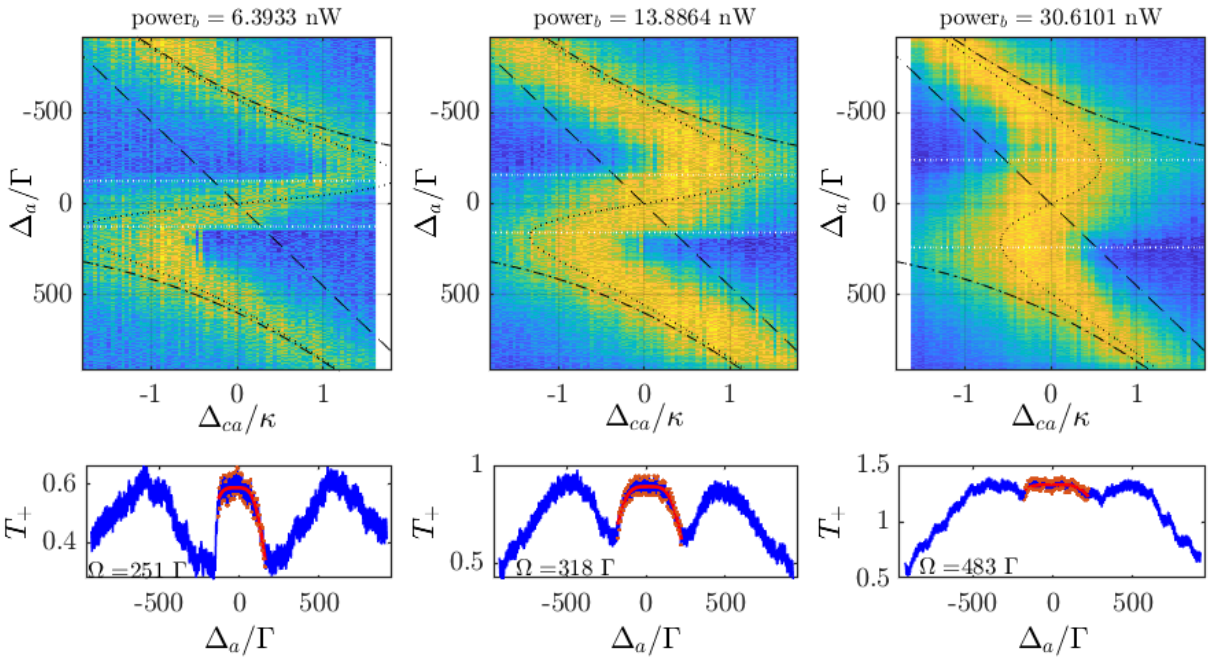

Figure 41 – (top) Avoided Crossing maps and (bottom) Normal-mode spectra ($\Delta_{ca} = 0$) $T_\pm$ Measured for different values of probe intensity. The dash-dotted line describing avoided crossing is calculated from 3.9, the anti-diagonal dashed line is calculated from 3.50, and the dispersive dotted line is calculated from 3.12 using as Rabi frequency the value extracted from the fit of the experimental measurement.

Source: By the author.

The subfigures a the bottom of each map show the spectra corresponding to $\Delta_{ca} = 0$. The fit performed to the central peak of the spectra is a flattop function, better understood as a convolution between a Gaussian and a rectangle function. As follows:

$$y = A \exp\left\{ -\left(\frac{x - x_0}{\sigma} \right)^{\beta} \right\} \tag{3.51}$$

with $\beta = 4$, since this exponent collapse again to a Gaussian function for $\beta = 2$. Therefore the linewidth is given by fwhm $= \sqrt{2log(2)}\sigma$. After the analysis, we obtained values that correspond with the equivalent Rabi frequency calculated from the measured transmitted light power used. This value is also pictured in the avoided crossing maps of the figure 41(top) as a white-dotted constant line at $\Delta_a/\Gamma = \pm\Omega/2$.

It is interesting to notice that in the avoided crossing maps, this value ($\Omega_{fit}/2$) reinforces a heightened asset, visible as a change in the shadow of the blue background corresponding to transmission intensities $T_+ < 0.1$, present on the spectra. We interpret this step in the spectra as a signature of the bistable regions as shown in section 3.1.2. Further studies of this region, its implications, and possible anomalies will be better analyzed in future works of our laboratory.

Nonetheless, a signature of the bistable regions can be seen by just comparing qualitatively the spectra simulated with equation 3.29 in figure 36 with the ones presented for our experimental observations in figure 41.

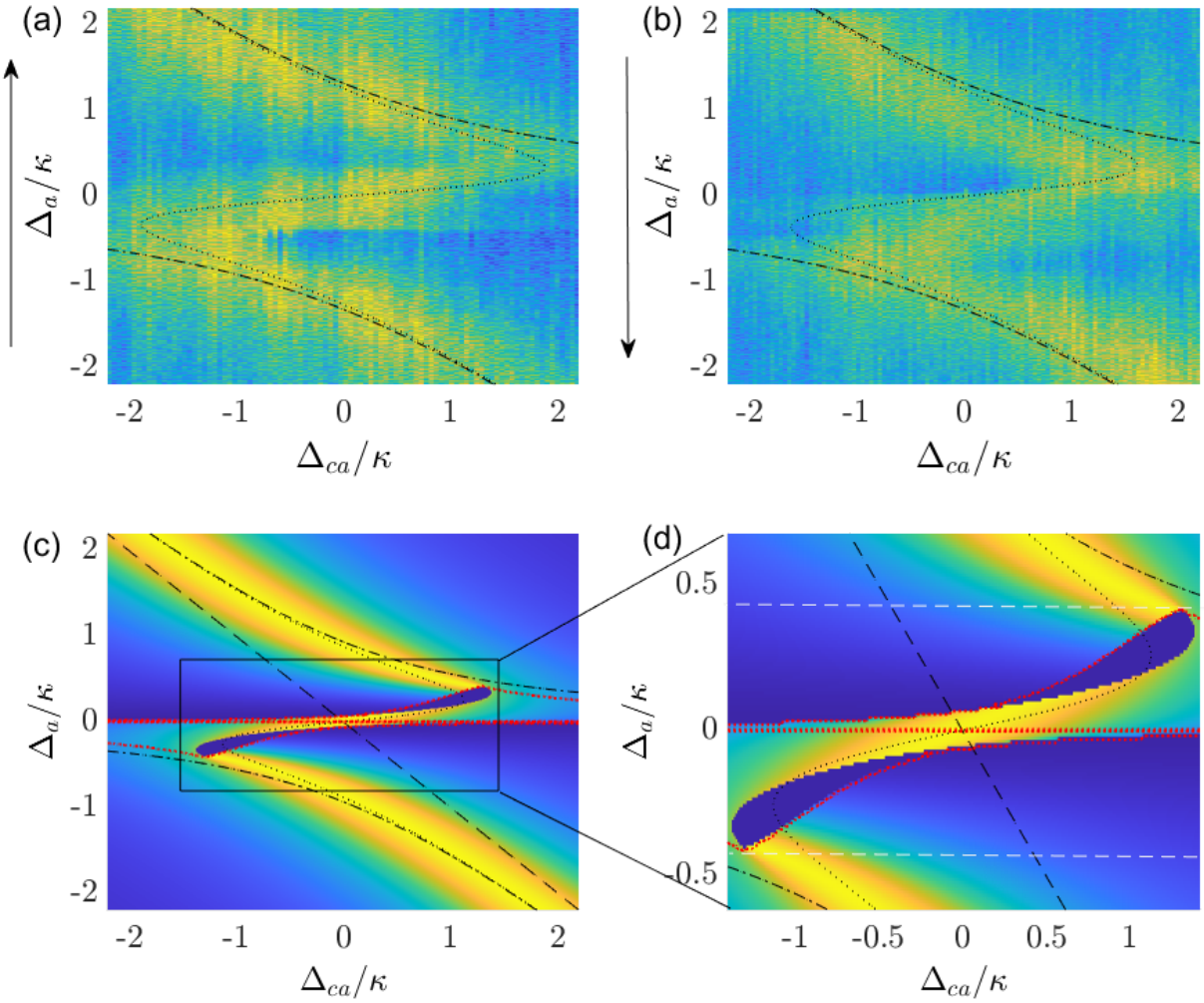

Figure 42 – (top) Avoided crossing of the normal-mode spectra $T_\pm$ Measured with different scan directions of the probe laser.(a) from $-2 \rightarrow 2$, (b) from $-2 \leftarrow 2$. As pictured with an arrow at the left of the scanned parameter. (bottom) Avoided Crossing maps using as Rabi frequency the value extracted from the fit of the experimental measurement presented in (a); (c) $\eta_+ = 115\Gamma$ (d) Zoom of the bistable region.

Source: By the author.

For better visualization of the bistable behavior, we performed a measurement, but instead we varied the scan direction of the probe. The results are shown in figure 42, and analogous to what we have presented, the Rabi frequency was extracted from the spectra at $\Delta_{ca} = 0$ and used to fit the ridges of equations 3.9, 3.50 and 3.12. In sub-figure (c) the numeric simulations of 3.8, together with a contoured area in red that highlights the bistable region is shown. It is possible to notice in subfigure (a) at $\Delta_a = -0.4\kappa \approx -115\Gamma/2$ an abrupt asset, that extents through several measurements. When we look at the scan performed in the opposite direction the abrupt asset appears instead at $\Delta_a = 0\kappa \approx 0\Gamma$. This behavior is understood when we look at the bistability regions, as presented with zoom in subfigure (d). If the scan is performed from bottom to top, the first bistable region will be found at $\Delta_a = -115\Gamma/2$, while the opposite action will bring us to the resonance before entering the bistable region.

The measurements presented so far were realized in a unique scan, that means that each trace was measured one time for experiment, therefore the spectra may present asymmetries as:

(a) Heating of the atoms during the scan can remove atoms from the cavity mode volume thus changing the number of atoms interacting with the cavity.

(b) The thermal cloud trapped in the dipolar potential occupies a finite region of space which leads to an inhomogeneous Stark shift which, in the spectrum, can be accounted for via convolution with a Boltzmann distribution.

(c) Intensity fluctuations in the probe light, accounting for lock stability and phase difference between the cavity locking laser and the probe laser.

As seen in Eq. 3.12, the saturation criterion applies to individual atoms and is NOT collective. Below saturation, the dynamics are described by single-atom physics, since it depends on the collective coupling strength $g_N = g\sqrt{N}$, but not on N or g separately. Below saturation, the excitation is intrinsically collective.

A summary of the main experimental parameters and other constants of the atom-cavity are presented in table 2.

Table 2 – Summary of parameters characterizing the ring cavity under s-polarization (except where stated otherwise), the atomic cloud trapped within the lowest-order Gaussian cavity mode, and the interaction between the atoms and light close to resonance with the $^1S_0 \leftrightarrow {}^3P_1$ transition. Details in the main text.

forbidden transition	λ_{689}	$= 689.449098\,\text{nm}$
decay rate of forbidden trans.	γ_{689}	$= 7.6\,\text{kHz}$
cavity round trip length	L	$= 3.64\,\text{cm}$
cavity mode volume	V	$= 0.5\,\text{mm}^3$
mode waist at atomic location	w	$= 68.5\,\mu\text{m}$
free spectral range	δ_{fsr}	$= 8.23\,\text{GHz}$
finesse under s-polarization	F_s	≈ 1000
finesse under p-polarization	F_p	≈ 100
cavity field decay rate	κ_s	$= (2\pi)3.9\,\text{MHz}$
cavity field decay rate	κ_p	$= (2\pi)41\,\text{MHz}$
recoil shift	ω_{rec}	$= (2\pi)4.78\,\text{kHz}$
coupling strength	g_1	$= (2\pi)9.1\,\text{kHz}$
number of trapped atoms	N	$= 120000$
temperature	T	$= 1\,\mu\text{K}$
Doppler width	$k\bar{v}$	$= (2\pi)14.1\,\text{kHz}$
cooperativity	C	$= 0.013$
collective cooperativity	C	> 1300
1-photon saturation	s	$= 1.4$
1-photon light shift	U_0	$= -(2\pi)0.42\,\text{Hz}$
1-photon scattering per atom	γ_0	$= (2\pi)0.016\,\text{mHz}$
collective coupling	NU_0/κ_s	$= -0.011$

Source: By the author.

3.3 Preliminary conclusions

This chapter showed for the first time in literature a normal mode splitting with three peaks. The observed normal-mode splitting is well understood with a model which disregards all interatomic correlations. However, above saturation within a certain pumping rate regime, a bistability regime is observed when the laser and the cavity are tuned to resonance with the atomic transition.

- Atomic bunching and saturation effects were studied via numerical simulations, with a model which disregards all inter-atomic correlations. We found a good agreement with the experimental results. Ultimately a model which inserts saturation in the adiabatically aproximated equation also show a good approximation with the observed effects.

- We report for the first time in literature a measurement of the three-peak normal mode splitting, where the central peak is induced by saturation. As predicted for Gripp *et al.* (65), the peak should emerge when the cavity and the pump laser frequencies are tuned to resonance.

- Atom-cavity interactions confirmed and characterized by normal mode splitting in the narrow transition.
- Preliminary observation of signatures of bistability in a strongly driven resonant atom-cavity system.

3.3.1 Remarks and prospects

Although the observations were done with an homogeneous density distribution of atoms inside a ring cavity pumped unidirectionally, the results apply as well to atoms organized in an optical lattice. Which experimental realizations are achievable in our machine.

Since we are able to work in the bistable regime, which is the starting point for collective effects, and since our cavity is in the 'bad cavity' limit, we reach also the requirements to observe optical correlations. That is, the photons emitted from one atom can stay inside the cavity and interact with other atoms. Our high CQED parameter, $g \gg \Gamma$, facilitates saturation without being afflicted with spontaneous emission, which means high collective cooperativity, $Ng^2/\Gamma \gg \kappa$, as necessary for correlating atoms (44).

4 SEARCH FOR BLOCH OSCILLATIONS

In 1929 Felix Bloch (14) wrote a theoretical proposal, that together with Zener (15) in 1934 set the bases of the formalism that predicts the behavior of electrons in a periodic potential and under the action of an electric field. This was made in an attempt to derive and explain the physics of conductivity in crystalline structures. This formalism predicts that under these conditions, the electrons will undergo an oscillatory behavior at a frequency proportional to the strength of the force.

We refer to a matter-wave of Sr atoms with its momentum distribution below the recoil limit, we can build a periodic potential with a standing wave created with a far-detuned laser (in comparison with the resonance of the atom), with a lattice constant parameter $a = \lambda/2$. With the geometry of the experimental setup chosen properly, then gravity ($F = mg$) can act as the constant force that will modify the periodic potential.

Periodic potentials for quantum particles can be realized artificially. A prominent example is optical lattices formed by the interference patterns of intersecting laser beams. Tuned sufficiently far away from atomic resonances the periodically structured light field exerts optical forces on the atoms which can be derived from potentials being proportional to the local light intensity. As these forces are relatively weak, the kinetic energy of the atoms must be very low to allow for their impact to be relevant. In many cases, the depth of the optical lattice only allows for a small number of localized quantum states, so the quantum nature of the atomic motion becomes highly relevant.

In this section, the description of the dynamics will be unfolded. A description of the formalism for an atom in the presence of a periodic potential will guide us to the dynamics of the atom performing Bloch Oscillations. Simulations of the dynamics will be presented in order to understand better what to expect from the experiment. We will impose a known periodic potential to a cold atomic cloud and study the atomic motion as well as the fields of the cavity.

4.0.1 1D Periodic potential

As already pointed out, a periodic optical potential can be generated by two counterpropagating plane wave laser beams, $e^{\pm \imath k_l z}$, with wavevectors k_l and $-k_l$ and tuned to the red side of an atomic transition. In this situation, the atoms are attracted to the maxima of the light intensity, the antinodes,

$$V(z) = \frac{V_0}{4}|e^{\imath k_l z} + e^{-\imath k_l z}|^2 = \frac{V_0}{2}[1 + \cos(2k_l z)] \ . \tag{4.1}$$

Neutral atoms in a vertical optical lattice are accelerated by gravity, and this

accelerated motion leads to Bloch oscillations.(98, 99)

Let us formulate the problem by extending the Hamiltonian by the gravitational potential.

$$\hat{H} = -\frac{\hbar^2}{2m}\frac{\partial^2}{\partial z^2} + \frac{V_0}{2}\cos 2k\hat{z} + mg\hat{z} \ . \tag{4.2}$$

We define the transformation $U \equiv e^{-\imath mg\hat{z}t/\hbar}$ and find that the Hamiltonian in the accelerated frame,

$$\tilde{H} = U^\dagger \hat{H} U + \imath\hbar \dot{U}^\dagger U = \frac{\tilde{p}^2}{2m} + \frac{V_0}{4}\left(e^{2\imath k\hat{z}} + e^{-2\imath k\hat{z}}\right) \ . \tag{4.3}$$

with

$$\tilde{p} \equiv \hat{p} - mgt = U^\dagger \hat{p} U \ . \tag{4.4}$$

Now, we expand the operators using the rules of transformation.

$$\begin{aligned} \tilde{p} &= \int p|p\rangle\langle p|dp \longrightarrow \sum_n (p + 2n\hbar k)|p + 2n\hbar k\rangle\langle p + 2n\hbar k| \\ e^{2\imath k\hat{z}} &= \int |p + 2\hbar k\rangle\langle p|dp \longrightarrow \sum_n |p + 2(n+1)\hbar k\rangle\langle p + 2n\hbar k| \ , \end{aligned} \tag{4.5}$$

based on the assumption that every atom can only exist in a superposition of discrete momentum states separated by $2\hbar k$, but can have an 'offset' momentum $p = mv$, e.g. due to thermal motion. Disregarding thermal motion, we may set in the accelerated frame $p = 0$. Then,

$$\tilde{p} = \sum_n 2n\hbar k|2n\hbar k\rangle\langle 2n\hbar k| \qquad \text{and} \qquad e^{2\imath k\hat{z}} = \sum_n |2n\hbar k + 2\hbar k\rangle\langle 2n\hbar k| \ , \tag{4.6}$$

such that,

$$\tilde{H} = \sum_n 4n^2\hbar\omega_{rec}|2n\hbar k\rangle\langle 2n\hbar k| + \tfrac{V_0}{4}\sum_n \left(|2n\hbar k + 2\hbar k\rangle\langle 2n\hbar k| + |2n\hbar k\rangle\langle 2n\hbar k + 2\hbar k|\right) \ . \tag{4.7}$$

With the expansion of the wavefunction $|\tilde{\psi}\rangle = \sum_n c_n|2n\hbar k\rangle$ the Schrödinger equation becomes (6, 7),

$$\begin{aligned} \imath\hbar\frac{d}{dt}|\tilde{\psi}\rangle &= \imath\hbar\sum_n \dot{c}_n|2n\hbar k\rangle \\ &= \sum_n \left(4n^2\hbar\omega_{rec}c_n + \tfrac{V_0}{4}(c_{n-1} + c_{n+1})\right)|2n\hbar k\rangle = \tilde{H}|\tilde{\psi}\rangle \ , \end{aligned} \tag{4.8}$$

that is,

$$\dot{c}_n = -4\imath n^2\omega_{rec}c_n + \frac{V_0}{4\imath\hbar}(c_{n-1} + c_{n+1}) \ . \tag{4.9}$$

In the lab frame, the wavefunction reads,

$$\begin{aligned} |\psi\rangle = U|\tilde{\psi}\rangle &= e^{-\imath mg\hat{z}t/\hbar}\sum_n c_n|2n\hbar k\rangle \\ &= \sum_n c_n|2n\hbar k - mgt\rangle = \sum_n c_n|2\hbar k(n - \nu_{blo}t)\rangle \ , \end{aligned} \tag{4.10}$$

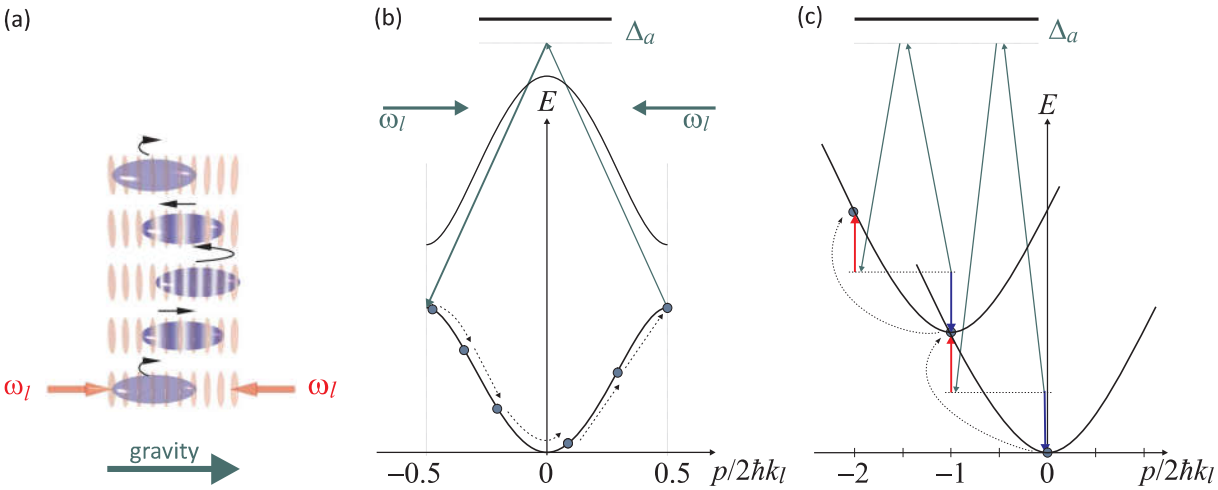

Figure 43 – Illustration of Bloch oscillations of a matter wave inside of an optical potential seen in (a) real space, (b) momentum space, and in (c) the moving frame.

Source: Adapted from COURTEILLE.(77)

where we introduced the ,

$$\boxed{\nu_{blo} = \frac{mg}{2\hbar k}} \,. \tag{4.11}$$

Finally,

$$\boxed{\dot{c}_n = -4\imath(n - \nu_{blo}t)^2\omega_{rec}c_n + \frac{V_0}{4\imath\hbar}(c_{n-1} + c_{n+1})} \,. \tag{4.12}$$

The center-of-the-mass momentum of the atomic matter wave is,

$$\frac{\langle p\rangle_{lab}}{\hbar k_l} = \sum_n n|c_n(t)|^2 + \nu_{blo}t \,. \tag{4.13}$$

Bloch oscillations can be seen as Bragg reflections at the edges of the Brillouin zone, these passages correspond to Raman transitions between the movement states $+k_l$ and $-k_l$ induced by the absorption of a photon from the counter-propagating laser beam and the re-emission of a photon within the co-propagating beam. This Raman scattering transfers twice the photonic recoil to the atom. In other words, as pictured in Fig. 43b, the matter wave is accelerated through the Brillouin zone and when reaches the edge is Bragg-reflected to the opposite edge. In the Bloch picture, the dispersion relation of a free particle is distorted due to the periodicity of the potential generated by the standing light wave such as to open a forbidden energy band. As a consequence, instead of being accelerated without limits, the atom enters the second Brillouin zone, which is to say that it is reflected on the other side of the first Brillouin zone.

The Bloch oscillations can be understood in various pictures. The first one, illustrated in 43(a), is based on : A resting atom has an infinite de Broglie wavelength. Being constantly accelerated by gravity, the matter wave reduces its de Broglie wavelength from

∞ to a value, where it becomes commensurate with the periodicity of the standing light wave potential. At this moment Bragg scattering comes into play, reflecting the atomic motion back into an upward direction, and the process starts over again. The atoms evolve like jumping on a trampoline with a frequency given by ν_{blo}.

A second picture of the phenomena can be addressed if we ask: In which way the matter wave interacts with the standing light wave? It is sufficient to know that the atom must have an internal transition capable of scattering photons from the light beams. As any absorption and emission process transfers a recoil momentum of $\hbar k_l$ to the atom, we can understand it as a Bragg scattering process. A photon of the laser beam generating the optical lattice coming from the left is absorbed and re-emitted to the left. This is best illustrated in the momentum domain sketched in Fig. 43(b). This Bragg scattering transfers twice the photonic recoil to the atom. The requirement for commensurability of the Broglie wavelength and wavelength of the standing light wave is equivalent to saying that the matter wave momentum is equal to the recoil of a single photon. In other words, the matter wave is always Bragg-reflected at the edge of a Brillouin zone.

$$\Delta p_{dB} = \omega_{rec} \qquad \lambda_{dB} = \frac{4\pi}{k} = a \tag{4.14}$$

Finally, in the Bloch state, the dispersion relation of a free particle is distorted due to the periodicity of the potential generated by the standing light wave such as to open a forbidden band. As a consequence, instead of being accelerated without limits, the atom enters the second Brillouin zone, which is to say that it is reflected on the other side of the first Brillouin zone.

The additional term, which contains the frequency of the Bloch oscillation ν_{blo}, increases linearly over time. As time goes by, a resonance is crossed when $t = -n\tau_{blo}$, and the crossing is periodically repeated at every $n = -1, -2, 0, ...$ Tracing the matter wave evolution in the laboratory system, we see that whenever the resonance is crossed, the momentum undergoes a change of sign corresponding to a reflection of its motion.

There are some conditions that need to be met to observe Bloch's oscillations. The transfer of momentum is efficient only in the rapid adiabatic passage (ARP) (99) regime characterized by the conditions $2(\nu_{blo}/\omega_{rec}) \ll (W_0/4\omega_{rec})^2 \ll 16$. The first condition requires that the force that drives the atoms to perform the Bloch oscillations must be weak enough to avoid transitions between Bloch bands, which guarantees the adiabaticity of the process. The other condition requires that the optical lattice be weak enough so that the dynamics involve only two adjacent momentum states at the same time and the transfer between the two is successful.

We run simulations of the dynamics* of eq 4.13. A relevant result of the simulations is pictured in Fig. 44

* See section 4.1 for a detailed description

4.1 Bloch dynamics simulation

In the limit where Bloch oscillations can be modeled by a two-level system (7) we may try a representation within the Dicke model and illustrate the dynamics on a Bloch sphere. The gravitational acceleration corresponds to a modification of kinetic energy without modification of the momentum state populations and without excitation of quantum coherences between them. Since the kinetic energy is represented by the vertical axis of the Bloch sphere, we may visualize acceleration via a rotation of the Bloch sphere, e.g. about the y-axis. The interpretation of the rotated Bloch sphere remains the same: the xy-plane shows the coherences and the z-axis the populations. Once this works, we can treat the thermal atomic cloud as a coherent spin state, e.g. squeeze it (35) or simulate the trajectory of individual atoms inhomogeneously (100) [†]. Assuming that, at any time, at most two discrete momentum states n and $n+1$ are coupled, the Hamiltonian 4.6 becomes,

$$\tilde{H} = 4\hbar\omega_{rec}n^2|2n\hbar k\rangle\langle 2n\hbar k| + 4\hbar\omega_{rec}(n+1)^2|2(n+1)\hbar k\rangle\langle 2(n+1)\hbar k| \tag{4.15}$$

$$+ \tfrac{V_0}{4}\left(|2(n+1)\hbar k\rangle\langle 2n\hbar k| + |2n\hbar k\rangle\langle 2(n+1)\hbar k|\right) \ . \tag{4.16}$$

Simulations of Bloch oscillations of atoms in an optical lattice for $W_0 = 0.4\omega_{rec}$ and $0.8\omega_{rec}$ produce the dynamics exhibited in Fig. 44.

(a-b) If the lattice is too shallow ($W_0 = 0.4\omega_{rec}$), the band gap is too narrow. The atom is then likely to tunnel into the next Bloch band staying inside its actual accelerated momentum state. I.e. stationary populations pile up in every c_n. Because the atom is not completely reflected at the edge of the Brillouin zone, its center of mass begins to drift.
(e-f) If the lattice is too deep ($W_0 = 1.6\omega_{rec}$), the atom does not even reach the band gap. It stays confined to the standing wave potential oscillating like in a harmonic potential.
(c-d) If the lattice is just right ($W_0 = 0.8\omega_{rec}$), the atom is almost completely reflected. Fast initial oscillations damp out because only the fastest atoms undergo Landau-Zener transitions confining them to the first momentum state c_0.
Approximating the lattice by a harmonic oscillator potential,

$$U_{dip}(z) = -\tfrac{\hbar W_0}{2}\cos 2kz \simeq -\tfrac{\hbar W_0}{2}(1+k^2z^2) \equiv \tfrac{m}{2}\omega_{ho}^2 z^2 \ , \tag{4.17}$$

we expect the vibration frequency, $\omega_{ho} = \sqrt{2W_0\omega_{rec}}$. Using this formula it is possible to check that the fast vibrations observed in Fig. 44 have frequencies that correspond to $\omega_{ho}/2$.

The relative strength of the Bloch oscillations is characterized by the depth of the potential

[†] Note that, In order to simulate a series of Bloch oscillations, we must change the basis by hand after each Bragg reflection.

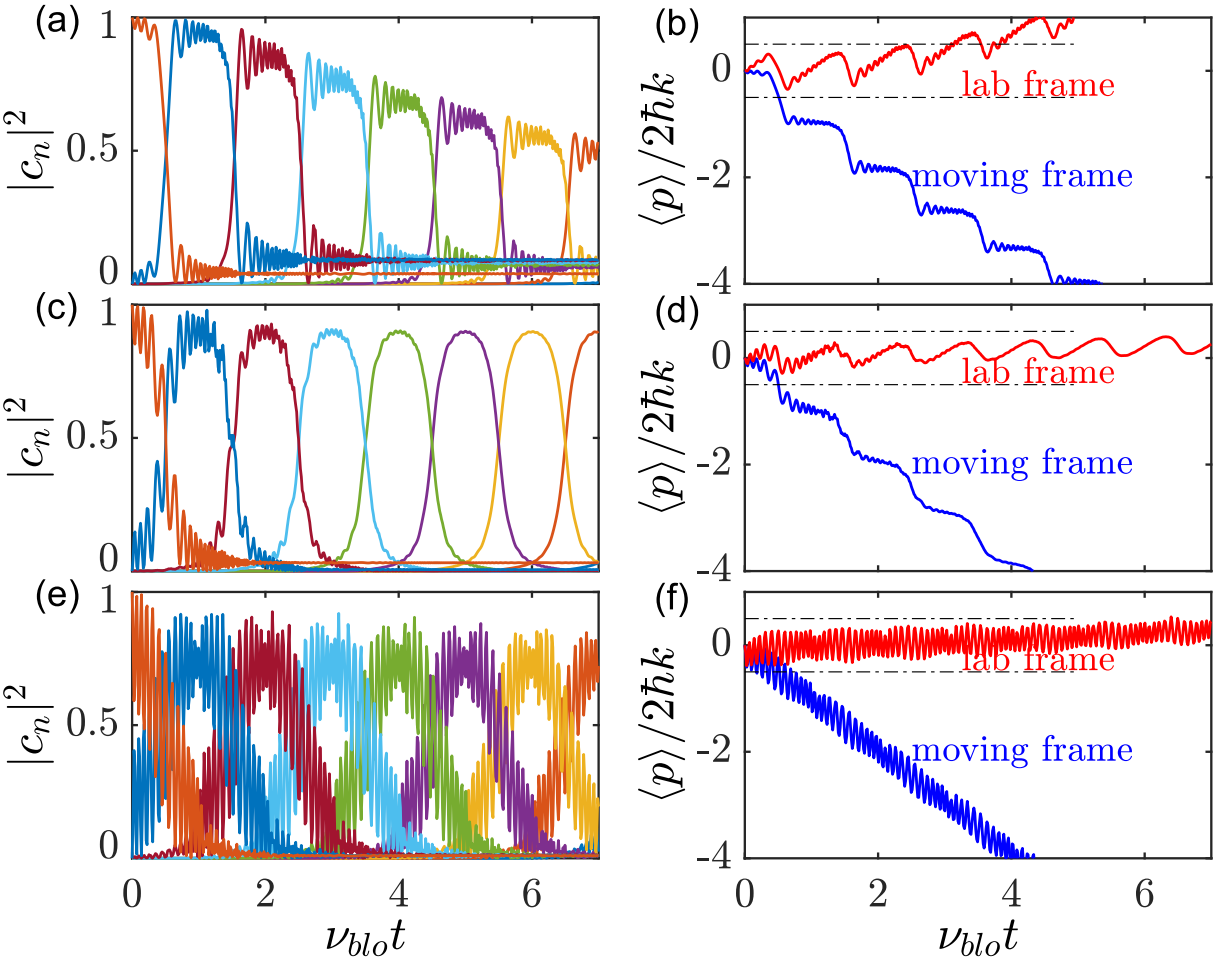

Figure 44 – Dynamics of Bloch oscillations (a-b) for $W_0 = 0.4\omega_{rec}$, (c-d) for $W_0 = 0.8\omega_{rec}$, and (e-f) for $W_0 = 1.6\omega_{rec}$. Furthermore, $\omega_{rec} = (2\pi)\ 4.8$ kHz and $\nu_{blo} = 0.05\omega_{rec}$.

Source: By the author.

The figure of merit for the occurrence of Bloch oscillations is the adiabatic rapid passage (ARP) condition, according to which the dipolar standing wave potential should only support a single bound state (6, 99),

$$\frac{16\nu_{blo}}{\omega_{rec}} \ll \left(\frac{V^{\updownarrow}_{0,dip}}{\hbar\omega_{rec}}\right)^2 \ll 1\ . \tag{4.18}$$

Or analogously to what other authors performed (22, 98), the height of the dipolar potential should correspond to:

$$1 \ll \frac{V^{\updownarrow}_{0,dip}}{\hbar\omega_{rec}} \ll 10\ . \tag{4.19}$$

For the strontium line λ_{689} we have $16\nu_{blo}/\omega_{rec} = 0.398$, so that, defining a 'Bloch parameter',

$$\boxed{\varepsilon_{blo} \equiv \frac{V^{\updownarrow}_{0,dip}}{\hbar\omega_{lat}} = \sqrt{\frac{V^{\updownarrow}_{0,dip}}{\hbar\omega_{rec}}} = \sqrt{4|\alpha_+||\alpha_-|\frac{U_0}{\omega_{rec}}}}\ , \tag{4.20}$$

the dipole trap depth needs to satisfy $0.631 < \varepsilon_{blo} < 1$.

For an intracavity laser powers of $P_{cav} = G \times P_{tr}$, with $P_{tr} = 4nW$, Which is achievable experimentally, we expect: This result suggests that we should look for Bloch

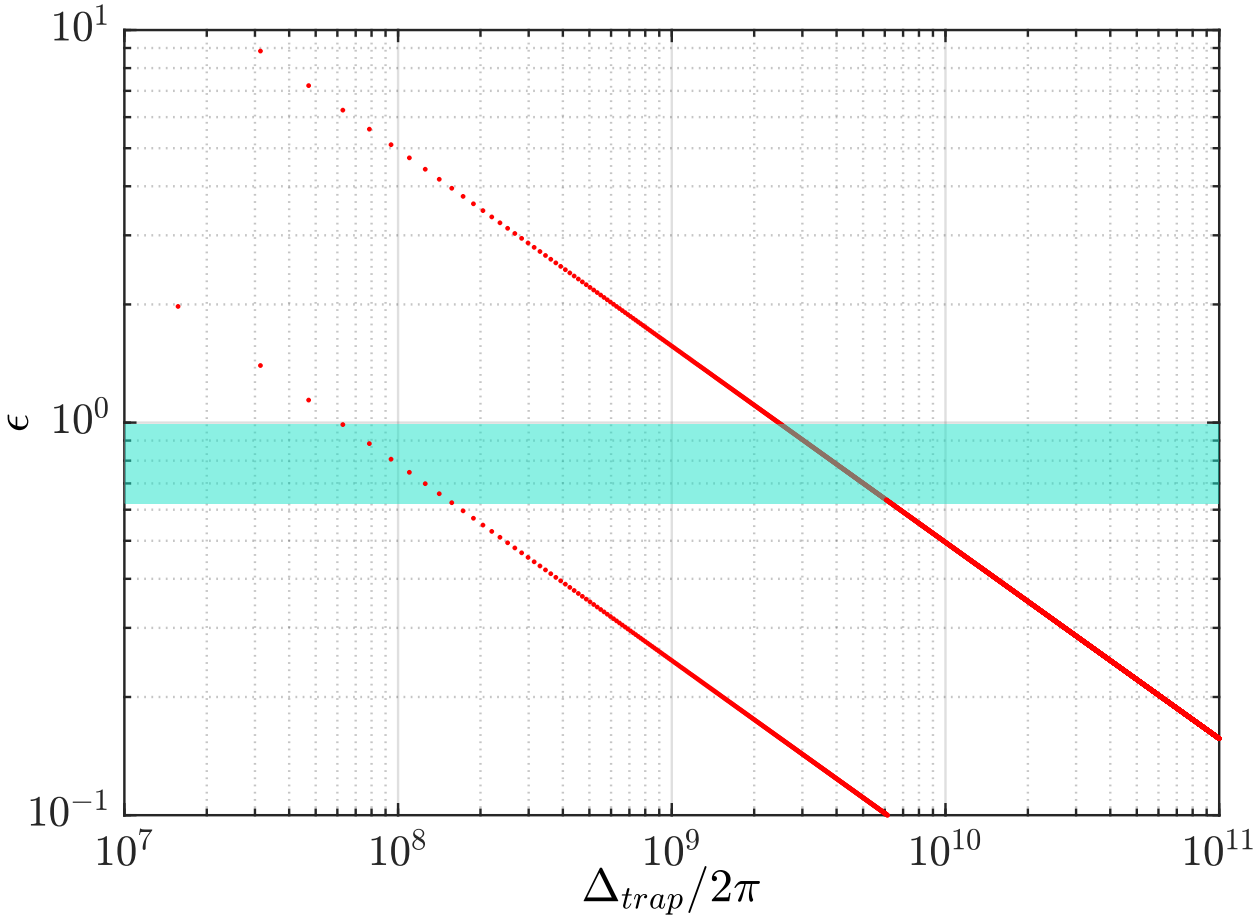

Figure 45 – Bloch parameter simulation, according to equation 4.20, as a function of the trap detuning for a fixed gain, the lines limit gains of 10 and 400 respectively. The shaded blue area represents the band at which BO can be observed.

Source: By the author.

oscillations at frequency detunings of the cavity laser bigger than 2 GHz, with the lowest possible gain, or at $\Delta\nu_{red2} > 14.5GHz$ if we work at the high finesse.

4.2 Experimental search for Bloch oscillations

The search for signatures of Bloch oscillations was performed using the setup already shown in the previous chapter (See figure 38). This setup offers more stability for the standing wave inside the cavity[‡].

[‡] Since each mode of the cavity is pumped by individual paths the phase difference of the light modes can be measured as the temporal evolution of the interference of the transmitted light. Differences in the phase can be attributed to thermal and mechanical noise introduced

We perform the usual proceeding to produce the cold cloud of Sr atoms, and we adjust the alignment and experimental parameters in order to have the lowest achievable temperatures in our experiment. After this, we usually have a cloud with about 80^3 atoms, at temperatures of 800 nK. The cloud is adiabatically transferred into the mode volume of a ring cavity via magnetic displacement of the center of the red MOT.

An optical dipole potential, operated near the strontium resonance, forms a standing wave inside the ring cavity via two laser beams coupled into counter-propagating TEM_{00} modes.

The next step, the cloud performing Bloch oscillations dynamics, can be pursued with different schemes:

- By adiabatically turning on the periodic potential, and consequently waiting for a time t_{hold}, at which the atoms are performing Bloch oscillations. As it was done in ref (22)
- After inserting the cloud inside of the periodic potential we wait a short period of time for thermalization and then we shut down the trap (at t) and quickly turn it back on (at $t_1 > t$), this sets the beginning of the oscillations of the ensemble to the second light period (t_1).
- Another way to proceed would be to trap the atoms into a periodic potential with the height of $V_0 > \epsilon_{Bloch}$, at which the atoms cannot perform Bloch oscillations, and subsequently diminish the height of the dipolar trap to values according to eq. 4.18.

After the cloud entered the cavity potential we wait for a time t_{hold} and record TOF images together with time records of the cavity transmissions. The analysis of the TOF images monitors momentum distributions of the cloud as a function of the time held in the cavity trap. FFT spectra of the transmitted light of the cavity are also investigated in the search for signatures of Bloch dynamics. The time-of-flight analysis plays an important role in the dynamics. Since the typical signatures of Bloch oscillations are given by the momentum track of the cloud, then we need to take into account that a minimum TOF is necessary to separate the momentum states.

Let us say, that we have a cloud of atoms that will experience the recoil caused by the interaction with the borders of the Brillouin zone, in a momentum states picture

via the devices that supply the laser light to enter the cavity. The setup shown in fig. 38 ensures a shorter laser path difference between pumps by separating the beams right before entering the cavity. This diminished the phase difference that was being accumulated in the old setup with the use of independent AOMs and fibers before the cavity for each mode. An alternative stable setup could be done by retro-reflecting the light rejected by the first cavity mode, nonetheless, this imposes some limitations of power and optical access that we strategically rejected.

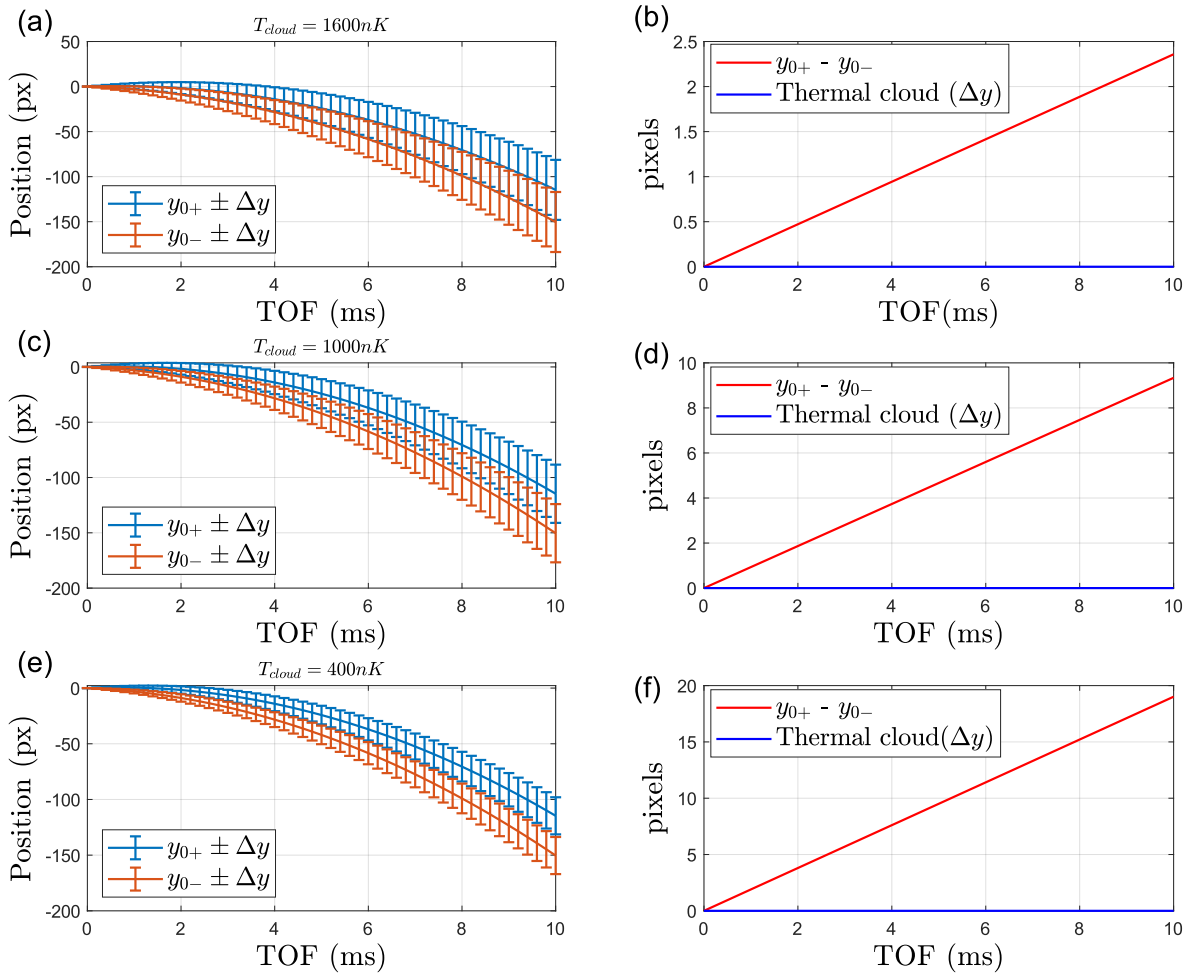

Figure 46 – (a,c,e) Calculated displacement (in pixels for our setup) for a free fall cloud (kicked at different directions ($\uparrow = y_{0+}$ and $\downarrow = y_{0-}$)), for different temperatures, as a function of the time of flight (TOF). The error bar describes the thermal expansion of the cloud-centered at the position displacement. (b,d,f) shows the net separation expected for different temperature clouds.

Source: By the author.

that corresponds to a superposition of states. Looking at TOF images we can understand it as a separation of the cloud in two fractions (See fig. 46), that is, one will be kicked in the upwards direction (y_{0+}) while the second will be kicked in the gravity direction (y_{0-}), while both fractions are constantly accelerated by gravity. As both clouds are overlapped at the same position, we have to measure the distribution after a TOF, at which we will observe a significant separation. For a cloud of Sr atoms, we can also calculate the thermal expansion of the cloud, which depends on its temperature, but will behave accordingly in the free fall behavior. That is, while the cloud breaks into two momentum clouds, each one of them will be also characterized by a thermal cloud according to its temperature. In fig 46 we picture the expected behavior for a free fall cloud at different temperatures, as a function of the displacement (in pixels for our setup). The error bar describes the

thermal expansion of the cloud for each position displacement.

As can be seen in figure 46a,c,e, the two clouds, are separated by a defined momentum kick (ω_{rec}), which can be seen clearer in TOF images. The cloud's temperature plays an important role in the separation of the momentum states as defined by absorption images since it also behaves accordingly. The separation of the different kicked clouds could be overlapped with the thermal tail, and for that, we have a shorter separation among the clouds. Figure 46b,d,f, pictures the net expected separation for clouds at different temperatures when we subtract the clouds displacement from its thermal tail.

The Bloch oscillations frequency 4.11 that we expect to measure for a cloud of Sr atoms (m= 88au), in a red detuned periodic potential created by a light far off-resonance (λ = 689 nm), in an experiment performed at São Carlos, Brazil (g = 978489668 μGal $\pm$13 μGal or g = $9.785 m/s^2$)(101) is given by:

$$\nu_{blo} = \frac{mg}{2\hbar k} = 743.3875 \text{ Hz} . \tag{4.21}$$

Now, let us remember that our cavity presents an angle with respect to the gravity direction, measured in 2.4.5 as $\alpha = 12.3°$, which translates to Bloch frequencies of:

$$\nu_{blo}x = \frac{mg \sin\alpha}{2\hbar k} = 157.8735 \text{ Hz} . \tag{4.22}$$

$$\nu_{blo}y = \frac{mg \cos\alpha}{2\hbar k} = 726.4302 \text{ Hz} . \tag{4.23}$$

The trials performed in our experiment were realized by taking into account the conditions already specified in 4.18, that is, the height of the potential created by the standing wave is :

$$\frac{V_{0,dip}^{\updownarrow}}{\hbar} \ll 10\omega_{rec} . \tag{4.24}$$

That can be achieved by increasing the detuning of the laser from the resonance or by decreasing the intensity of the light coupled to the cavity. We also take care of the temperature of the cloud, around 1 μK, as well as the stability of the standing wave.

The experiments performed showed no conclusive presence of a cloud oscillating with the Bloch's frequency. The light transmitted through the cavity was also analyzed and no clear signatures of the atom's presence were extracted. A typical analysis of the absorption images is presented in fig 47. Subfigures a and b show that the position of the cloud is stable in time, and the error bar (commonly associated with the width of the thermal cloud) is as well. We perform FFT of the data, see subfigure d, in an attempt to clean up or filter frequencies, but no clear signals were found. Subfigure c, shows an oscillation present on the number of atoms, that nonetheless, is also not conclusive, since the periodicity is not sufficiently strong.

We perform many trials with the main parameters varying from the lowest achievable experimental conditions to the upper limits. We also tried 3 different schemes for

introducing light into the cavity to create the standing wave. And we monitored our experiments via 2 different methods. Although the conditions could be improved, the approach used was clean and reproducible.

4.3 Preliminary conclusions

This chapter summarized the ingredients necessary to study Bloch oscillation with cold atoms, nonetheless, our observations are still inconclusive.

An important issue for experiments of Bloch Oscillations is the phase stability of the standing wave. Normally these experiments are performed in optical lattices created by retro-reflected beams (22). In this setup, the phase difference is given by the phase acquired by the light in the retro-reflection, therefore the stability of this mirror is fundamental for the lattice. Some other setups create lattices with two counter-propagating beams, showing that this issue can lead to a dephasing that destroys the Bloch dynamics (98) In our experiment, the phase stability of the lights (different pumping directions of the ring cavity) is fixed for only one of the beams, meanwhile, the second beam that enters the cavity could accumulate a phase difference. Experimental techniques can be applied to diminish the phase difference among the beams, just like already done by Krenz *et al.*(102). We also analyzed a beat between the lights transmitted by the cavity and observed an oscillation on the order of a few Hz (less than 5Hz), this time constant is large compared with the time we spent performing a measurement of the oscillating cloud. This parameter can be improved by creating feedback to one of the amplitude modulators of the non-stabilized arms, ensuring in that way a super-stable lattice.

Strontium atoms oscillating in a periodic potential have been seen already in different experiments, nonetheless, most of that experiments count on a BEC as a matter wave. Experiments using a thermal cloud were already performed by (98), using rubidium, and just as they justified in their observations, the thermal cloud affects in a negative way the visibility of the momentum states. We strongly believe that the temperature of the cloud is playing against us, since the lattice of our trap is defined by k_{red}^{-1}, which means that the recoil experienced by the atoms is on the order of the tail of the thermal cloud. Further cooling of Sr atoms can be achieved with a more complex setup, in which the atoms are velocity selected by means of Raman beams, or Bragg beams, as already performed by different interferometers in the literature.

We are able to achieve the proper conditions for the evolution of a trapped cloud in a periodic potential in the presence of a co-linear constant force, nonetheless, a clear signature has not been confirmed.

Since our cavity presents already confirmed strong collective interaction, we also suggest the use of the low finesse as a cavity stabilizer, while the creation of the standing

wave could be performed by means of the bi-directional probe. Fine adjustment of the frequency and intensity of the trap should be possible with the probe light. The signatures in the absorption images could still be sneaky, but signatures in the light should appear since the atom-cavity interaction is enhanced by the collective behaviour.

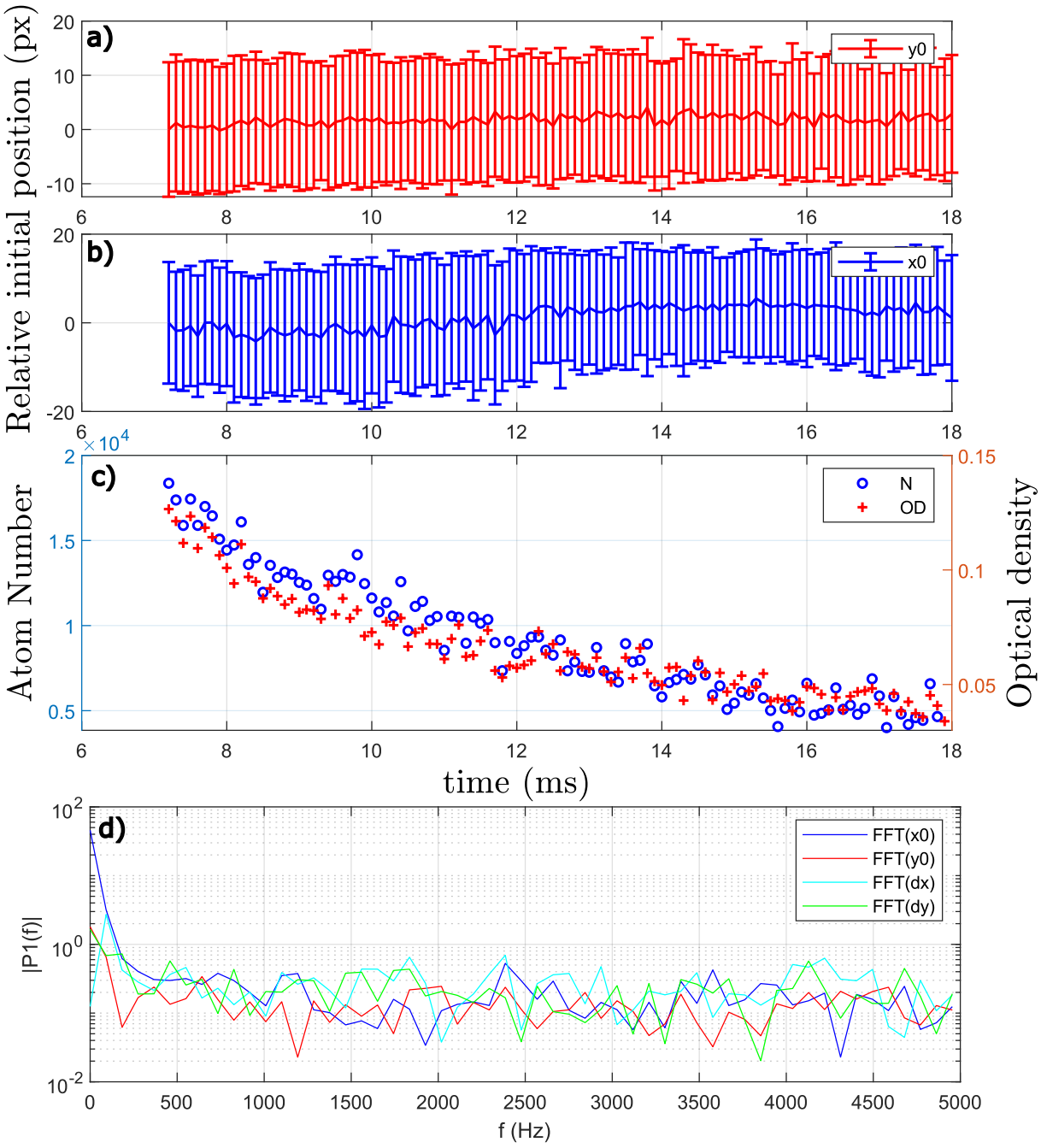

Figure 47 – Typical experimental characterization of the absorption images acquired in a BO experiment, TOF= 7 ms, $V^{\updownarrow}_{0,dip}/\hbar = 7\omega_{rec}$. a,b) Relative initial position of the cloud in the specified direction, the error bars correspond to the rms of the cloud. c) Number of atoms, and optical density of the cloud as a function of time. d) FFT of the parameters analyzed.

Source: By the author.

CONCLUSION

In this thesis, we described our approach to constructing and optimizing a machine capable of producing a cold atom cloud of strontium atoms inside a pumped ring cavity. The setup has proven to be stable in terms of performance and reproducibility of the experiments, and bistable in the saturated resonant regime.

In chapter one, we detailed the ingredients necessary for the machine's construction. Characterizations of the two stages of cooling of Strontium atoms were presented. A so-called 3D-blue magneto-optical trap operated on a broad atomic transition is loaded by a bichromatic 2D-MOT, which produces a blue cloud sufficiently cold to serve as an atomic source for the second cooling stage, the red MOT. In order to address the red transition an injection lock scheme for stabilization, control, and light amplification was implemented. The cloud produced in our red MOT holds 250000 atoms, at temperatures as low as 800 nK. Automatization and remote control of the electronic devices were developed, together with software to retrieve and analyze experimental data.

In the second chapter, we show the design, calculations, and characterizations of our bare ring cavity. A lock chain by means of a DPLL transmits the stability of a supercavity to our ring cavity. Furthermore, we also show the steps and details to take care of the introduction of the cloud in the ring cavity, which serves as a dipolar trap for the atoms. The dipolar potential trapped cloud, in running wave and standing wave configurations, was characterized, showing that we can transfer up to 80% of the red cloud, with temperatures of around 1μK.

Chapter 3, offers a more detailed description of the atom-cavity interactions. We study and perform normal mode splitting measurements, and we found a behavior that has not been reported in the literature, yet. The results are properly understood within a mean-field approach. Collective effects are found to be, responsible for the bistable dynamics observed in our coupled atoms-bad cavity system.

The search for Bloch Oscillations is further pursued in chapter 4. A guide of the necessary ingredients, as well as simulations of the expected frequencies, are shown. Clear measurement of the Bloch oscillations its been elusive so far, but we suggest further steps that can be implemented in the setup.

The playground provided by a strong resonantly driven interacting atom-cavity system is of enormous potential for the studies of different physical systems. Future studies may focus on the realization of non-classical quantum correlations in this system. The potentiality of the machine to perform experiments on diverse regimes is enormous.

REFERENCES

1 SANSONETTI, J. E.; NAVE, G. Wavelengths, transition probabilities, and energy levels for the spectrum of neutral strontium (sri). **Journal of Physical and Chemical Reference Data**, v. 39, n. 3, p. 033103, 2010.

2 STELLMER, S. **Degenerate Quantum Gases of Strontium**. 2013. 1–80 p. Tese (Doutorado) — University of Innsbruck, Faculty of Mathematics, Computer Science and Physics, 2013.

3 COURTEILLE, P. W.; BACHELARD, R. **Dispositivo e método para medida da aceleração gravitacional**. 2015. Available at: https://patents.google.com/patent/BR102015007944A2. Accessed on: 11 Jan, 2021.

4 PEDEN, B. M. *et al.* Nondestructive cavity qed probe of bloch oscillations in a gas of ultracold atoms. **Physical Review A**, American Physical Society, v. 80, n. 4, p. 043803, Oct 2009.

5 GOLDWIN, J.; VENKATESH, B. P.; O'DELL, D. H. J. Backaction-driven transport of bloch oscillating atoms in ring cavities. **Physical Review Letters**, American Physical Society, v. 113, p. 073003, Aug 2014.

6 SAMOYLOVA, M. *et al.* Mode-locked Bloch oscillations in a ring cavity. **Laser Physics Letters**, v. 11, n. 12, p. 126605, 2014.

7 SAMOYLOVA, M. *et al.* Synchronization of Bloch oscillations by a ring cavity. **Optics Express**, v. 23, n. 11, p. 14823, June 2015.

8 RIVERO, D. *et al.* High-resolution laser spectrometer for matter wave interferometric inertial sensing with non-destructive monitoring of bloch oscillations. **Applied Physics B**, Springer Science and Business Media LLC, v. 128, n. 3, Feb. 2022.

9 BORDé, C. Atomic interferometry with internal state labelling. **Physics Letters A**, v. 140, n. 1, p. 10–12, 1989.

10 GUO, J. *et al.* Recoil-induced resonances in nonlinear spectroscopy. **Physical Review A**, American Physical Society, v. 46, p. 1426–1437, Aug 1992.

11 STENGER, J. *et al.* Bragg spectroscopy of a bose-einstein condensate. **Physical Review Letters**, American Physical Society, v. 82, p. 4569–4573, June 1999.

12 ANDREWS, M. R. *et al.* Direct, nondestructive observation of a bose condensate. **Science**, American Association for the Advancement of Science, v. 273, n. 5271, p. 84–87, 1996.

13 GERICKE, T. *et al.* High-resolution scanning electron microscopy of an ultracold quantum gas. **Nature Physics**, v. 4, n. 12, p. 949–953, Dec 2008.

14 BLOCH, F. Über die Quantenmechanik der Elektronen in Kristallgittern. **Zeitschrift für Physik**, v. 52, n. 7-8, p. 555–600, July 1929.

15 ZENER, C.; WILLS, H. H. A theory of the electrical breakdown of solid dielectrics. **Proceedings of the Royal Society of London. Series A, Containing Papers of a Mathematical and Physical Character**, v. 145, n. 855, p. 523–529, July 1934.

16 BONIFACIO, R.; De Salvo, L. Collective atomic recoil laser (CARL) optical gain without inversion by collective atomic recoil and self-bunching of two-level atoms. **Nuclear Instruments and Methods in Physics Research Section A: Accelerators, Spectrometers, Detectors and Associated Equipment**, v. 341, n. 1-3, p. 360–362, Mar 1994.

17 KRUSE, D. *et al.* Observation of lasing mediated by collective atomic recoil. **Physical Review Letters**, v. 91, n. 18, p. 1–4, 2003.

18 VON CUBE, C. *et al.* Self-synchronization and dissipation-induced threshold in collective atomic recoil lasing. **Physical Review Letters**, v. 93, n. 8, p. 8–11, 2004.

19 COURTEILLE, P. W. The collective atomic recoil laser. In: **AIP Conference Proceedings**. [S.l.]: AIP, 2005. v. 770, p. 135–143. ISBN 0735402558.

20 Ben-Dahan, M. *et al.* Bloch Oscillations of Atoms in an Optical Potential. **Physical Review Letters**, v. 76, n. 24, p. 4508–4511, June 1996. DOI:10.1103/PhysRevLett.76.4508.

21 MORSCH, O. *et al.* Bloch oscillations and mean-field effects of Bose-Einstein condensates in 1D optical lattices. **Physical Review Letters**, v. 87, n. 14, p. 140402, Sep 2001.

22 FERRARI, G. *et al.* Long-lived bloch oscillations with bosonic sr atoms and application to gravity measurement at the micrometer scale. **Physical Review Letters**, American Physical Society, v. 97, p. 060402, Aug 2006.

23 SLAMA, S. *et al.* Superradiant rayleigh scattering and collective atomic recoil lasing in a ring cavity. **Physical Review Letters**, American Physical Society, v. 98, p. 053603, Feb 2007.

24 BUX, S. *et al.* Cavity-controlled collective scattering at the recoil limit. **Physical Review Letters**, American Physical Society, v. 106, p. 203601, May 2011.

25 KATORI, H. *et al.* Magneto-optical trapping and cooling of strontium atoms down to the photon recoil temperature. **Physical Review Letters**, American Physical Society, v. 82, p. 1116–1119, Feb 1999.

26 YASUDA, M.; KATORI, H. Lifetime measurement of the $^3p_2$ metastable state of strontium atoms. **Physical Review Letters**, American Physical Society, v. 92, p. 153004, Apr 2004.

27 IDO, T.; KATORI, H. Recoil-free spectroscopy of neutral sr atoms in the lamb-dicke regime. **Physical Review Letters**, American Physical Society, v. 91, n. 5, p. 053001, July 2003.

28 TAKAMOTO, M. *et al.* An optical lattice clock. **Nature**, v. 435, n. 7040, p. 321–324, May 2005.

29 DEREVIANKO, A.; KATORI, H. *Colloquium*: physics of optical lattice clocks. **Reviews of Modern Physics**, American Physical Society, v. 83, n. 2, p. 331–347, May 2011.

30 TINO, G. M. *et al.* Sage: A proposal for a space atomic gravity explorer. **The European Physical Journal D**, v. 73, n. 11, p. 228, Nov 2019.

31 RUDOLPH, J. *et al.* Large momentum transfer clock atom interferometry on the 689 nm intercombination line of strontium. **Physical Review Letters**, American Physical Society, v. 124, n. 8, p. 083604, Feb 2020.

32 HU, L. *et al.* Atom interferometry with the sr optical clock transition. **Physical Review Letters**, American Physical Society, v. 119, n. 26, p. 263601, Dec 2017.

33 HU, L. *et al.* Sr atom interferometry with the optical clock transition as a gravimeter and a gravity gradiometer. **Classical and Quantum Gravity**, IOP Publishing, v. 37, n. 1, p. 014001, Nov 2019.

34 KESSLER, H. *et al.* In situ observation of optomechanical Bloch oscillations in an optical cavity. **New Journal of Physics**, IOP Publishing, v. 18, n. 10, p. 0–7, 2016.

35 KITAGAWA, M.; UEDA, M. Squeezed spin states. **Physical Review A**, American Physical Society, v. 47, n. 6, p. 5138–5143, Jun 1993.

36 LEROUX, I. D.; SCHLEIER-SMITH, M. H.; VULETIC, V. Implementation of cavity squeezing of a collective atomic spin. **Physical Review Letters.**, v. 104, n. 7, p. 073602, 2010.

37 SCHLEIER-SMITH, M. H.; LEROUX, I. D.; VULETIC, V. Squeezing the collective spin of a dilute atomic ensemble by cavity feedback. **Physical Review A**, v. 81, n. 2, p. 021804(R), 2010.

38 SCHLEIER-SMITH, M. H.; LEROUX, I. D.; VULETIC, V. States of an ensemble of two-level atoms with reduced quantum uncertainty. **Physical Review Letters.**, v. 104, n. 7, p. 073604, 2010.

39 CHEN, Z. *et al.* Conditional spin squeezing of a large ensemble via the vacuum rabi splitting. **Physical Review Letters.**, v. 106, n. 13, p. 133601, 2011.

40 BOHNET, J. G. *et al.* Reduced spin measurement back-action for a phase sensitivity ten times beyond the standard quantum limit. **Nature Photonics**, v. 8, p. 731, 2014. DOI:10.1038/nphoton.2014.151.

41 COX, K. C. *et al.* Deterministic squeezed states with collective measurements and feedback. **Physical Review Letters.**, v. 116, n. 9, p. 093602, 2016.

42 XU, M. *et al.* Supercooling of atoms in an optical resonator. **Physical Review Letters.**, v. 116, n. 15, p. 153002, 2016.

43 SALVI, L. *et al.* Squeezing on momentum states for atom interferometry. **Physical Review Letters.**, v. 120, n. 3, p. 033601, 2018.

44 MEISER, D. *et al.* Prospects for a millihertz-linewidth laser. **Physical Review Letters.**, v. 102, n. 16, p. 163601, 2009.

45 MAIER, T. *et al.* A superradiant clock laser on a magic wavelength optical lattice. **Optics Express**, v. 22, n. 11, p. 13269, 2014.

46 NORCIA, M. A. *et al.* Superradiance on the millihertz linewidth strontium clock transition. **Science Advances**, v. 2, n. 10, p. e:1601231, 2016.

47 NORCIA, M. A.; THOMPSON, J. K. Cold-strontium laser in the superradiant crossover regime. **Physical Review X**, v. 6, n. 1, p. 011025, 2016.

48 NORCIA, M. A. *et al.* Cavity-mediated collective spin-exchange interactions in a strontium superradiant laser. **Science**, v. 361, n. 6399, p. 259, 2018.

49 DAVIS, E. J. *et al.* Photon-mediated spin-exchange dynamics of spin-1 atoms. **Physical Review Letters.**, v. 122, n. 1, p. 010405, 2019.

50 BYCHEK, A. *et al.* Superradiant lasing in inhomogeneously broadened ensembles with spatially varying coupling. **ePrints**, arXiv2105.11023, 2021.

51 ORIOLI, A. P.; THOMPSON, J. K.; REY, A. M. Emergent dark states from superradiant dynamics in multilevel atoms in a cavity. **Physical Review X**, v. 12, n. 1, p. 011054, 2022.

52 HOSTEN, O. *et al.* Quantum phase magnification. **Science.**, v. 352, n. 6293, p. 1552, 2016.

53 CLINE, J. R. K. *et al.* Continuous collective strong coupling between atoms and a high finesse optical cavity. **ePrints**, arXiv:2211.00158v1, 2022.

54 LAMBRECHT, A. *et al.* Squeezing with cold atoms. **Europhysics Letters**, v. 36, n. 2, p. 93, 1996.

55 TURCHETTE, Q. A. *et al.* Squeezed excitation in cavity qed: Experiment and theory. **Physical Review A**, v. 58, n. 5, p. 4056, 1998.

56 SCHNABEL, R. *et al.* Quantum metrology for gravitational wave astronomy. **Nature Communications**, v. 1, p. 121, 2016. DOI:10.1038/ncomms1122.

57 LOUCHET-CHAUVET, A. *et al.* Entanglement-assisted atomic clock beyond the projection noise limit. **New Journal of Physics**, v. 12, n. 6, p. 065032, 2009.

58 DANTAN, A. *et al.* Spin squeezing and light entanglement in coherent population trapping. **Physical Review Letters.**, v. 97, n. 2, p. 023605, 2006.

59 GIBBS, H. M.; MCCALL, S. L.; VENKATESAN, T. N. C. Differential gain and bistability using a sodium-filled fabry-perot interferometer. **Physical Review Letters.**, v. 36, n. 19, p. 1135, 1976.

60 LAMBRECHT, A.; COURTY, J.; GIACOBINO, E. Optical nonlinear dynamics with cold atoms in a cavity. **Optics Communications.**, v. 115, n. 1-2, p. 199, 1995.

61 GUPTA, S. *et al.* Cavity nonlinear optics at low photon numbers from collective atomic motion. **Physical Review Letters.**, v. 99, n. 21, p. 213601, 2007.

62 RITTER, S. *et al.* Dynamical coupling between a bose-einstein condensate and a cavity optical lattice. **Applied Physics B**, v. 95, p. 213, 1976. DOI:10.1007/s00340-009-3436-9.

63 GABOR, B. *et al.* Ground state bistability of cold atoms in a cavity. **arxiv:2207.01724**, 2022.

64 SUAREZ, E. *et al.* Collective atom-cavity coupling and nonlinear dynamics with atoms with multilevel ground states. **arXiv:2210.06085**, 2023.

65 GRIPP, J.; MIELKE, S. L.; OROZCO, L. A. Evolution of the vacuum rabi peaks in a detuned atom-cavity system. **Physical Review A**, American Physical Society, v. 56, n. 4, p. 3262–3273, Oct 1997.

66 GRIPP, J.; OROZCO, L. A. Evolution of the vacuum rabi peaks in a many-atom system. **Quantum and Semiclassical Optics part B.**, v. 8, n. 4, p. 823, 1997.

67 GOTHE, H. *et al.* Optical bistability and nonlinear dynamics by saturation of cold yb atoms in a cavity. **Physical Review A**, v. 99, n. 1, p. 013849, 2019.

68 ZHU, Y. *et al.* Vacuum rabi splitting as a feature of linear-dispersion theory: Analysis and experimental observations. **Journal of Optical Society of America B**, v. 64, n. 21, p. 2499, 1990.

69 SCHUSTER, I. *et al.* Nonlinear spectroscopy of photons bound to one atom. **Nature Physics Letters**, v. 4, n. 5, p. 382, 2001.

70 MÜCKE, M. *et al.* Electromagnetically induced transparency with single atoms in a cavity. **Nature**, v. 465, n. 7299, p. 755, 2010.

71 ARNOLD, K. J.; BADEN, M. P.; BARRETT, M. D. Collective cavity quantum electrodynamics with multiple atomic levels. **Physical Review A**, v. 84, n. 3, p. 033843, 2011.

72 RITSCH, H. *et al.* Cold atoms in cavity-generated dynamical optical potentials. **Review of Modern Physics**, v. 85, p. 553, 2013.

73 ROHLF, J. **Modern Physics from alpha to Z0**. [S.l.]: Wiley, 1994. ISBN 9780471572701.

74 MICKELSON, P. G. *et al.* Bose-einstein condensation of ^{88}Sr through sympathetic cooling with ^{87}Sr. **Physical Review A**, American Physical Society, v. 81, n. 5, p. 051601, May 2010.

75 MOORE, R. W. G. *et al.* Measurement of vacuum pressure with a magneto-optical trap: a pressure-rise method. **Review of Scientific Instruments**, v. 86, n. 9, p. 093108, 2015.

76 PERRIN, H. Les houches lectures on laser cooling and trapping. Accessible at 23 Jan. 2021. Disponível em: <http://www-lpl.univ-paris13.fr/bec/bec/Teaching/lecture2_2012-.pdf>.

77 COURTEILLE, P. W. **Quantum mechanics applied to atoms and light**. 2019. Disponível em: <http://www.ifsc.usp.br/~strontium/Publication/Scripts-/QuantumMechanicsScript.pdf>.

78 ARMIJOS, M. A. M. **Construction of an experiment providing cold strontium atoms for atomic interferometry in a ring cavity**. 2020. 1–68 p. Dissertação (Mestrado) — Instituto de Física de São Carlos, Universidade de São Paulo, São Carlos, 2020.

79 RAAB, E. L. *et al.* Trapping of neutral sodium atoms with radiation pressure. **Physical Review Letters**, American Physical Society, v. 59, n. 23, p. 2631–2634, 1987.

80 METCALF, H.; STRATEN, P. van-der. **Laser cooling and trapping**. [S.l.]: Springer New York, 2012. (Graduate Texts in Contemporary Physics). ISBN 9781461214700.

81 DIECKMANN, K. *et al.* Two-dimensional magneto-optical trap as a source of slow atoms. **Physical Review A**, American Physical Society, v. 58, n. 5, p. 3891–3895, Nov 1998.

82 PEDROZO-PEÑAFIEL, E. *et al.* Direct comparison between a two-dimensional magneto-optical trap and a zeeman slower as sources of cold sodium atoms. **Laser Physics Letters**, IOP Publishing, v. 13, n. 6, p. 065501, May 2016.

83 RIVERO, D. *et al.* Hollow bessel beams for guiding atoms between vacuum chambers: a proposal and efficiency study. **Journal of the Optical Society of America B**, Optica Publishing Group, v. 37, n. 9, p. 2660–2667, Sep 2020.

84 STELLMER, S.; SCHRECK, F. Reservoir spectroscopy of $5s5p\ ^3p_2$–$5snd\ ^3D_{1,2,3}$ transitions in strontium. **Physical Review A**, American Physical Society, v. 90, n. 2, p. 022512, Aug 2014.

85 MORIYA, P. H. *et al.* Comparison between 403 nm and 497 nm repumping schemes for strontium magneto-optical traps. **Journal of Physics Communications**, IOP Publishing, v. 2, n. 12, p. 125008, Dec 2018.

86 DREVER, R. W. P. *et al.* **Laser phase and frequency stabilization using an optical resonator**. [S.l.], 1983. v. 31, 97–105 p. DOI:10.1007/bf00702605.

87 SILVA, C. B. **Development of a stable diode laser system for cavity-assisted matter-wave interferometry**. 2020. 1–65 p. Dissertação (Mestrado) — Universidade Federal de São Carlos, São Carlos, 2020.

88 RAZAVI, B. A study of injection locking and pulling in oscillators. **IEEE Journal of Solid-State Circuits**, v. 39, n. 9, p. 1415–1424, 2004.

89 YUAN, F. **Injection-locking in mixed-mode signal processing**. [S.l.]: Springer International Publishing, 2019. ISBN 9783030173647.

90 LIU, Z.; SLAVIK, R. Optical injection locking: from principle to applications. **Journal of Lightwave Technology**, v. 38, n. 1, p. 43–59, 2020.

91 COMITO, G. B. **Estudo e solução experimental da transferência de átomos de estrôncio da armadilha magneto-ótica inicial (azul) para a subsequente (vermelha)** . [S.l.], 2019.

92 MUNIZ, S. R. *et al.* Measurements of capture velocity in a magneto-optical trap for a broad range of light intensities. **Physical Review A**, American Physical Society, v. 65, n. 1, p. 015402, Dec 2001.

93 APPEL, J.; MACRAE, A.; LVOVSKY, A. I. A versatile digital GHz phase lock for external cavity diode lasers. **Measurement Science and Technology**, IOP Publishing, v. 20, n. 5, p. 055302, Apr 2009.

94 SCULLY, M. O. *et al.* Directed spontaneous emission from an extended ensemble of n atoms: Timing is everything. **Physical Review Letter.**, v. 96, n. 1, p. 010501, 2006.

95 COURTEILLE, P. W. *et al.* Modification of radiation pressure due to cooperative scattering of light. **The European Physical Journal. D**, v. 58, p. 69–73, 2010. 10.1140/epjd/e2010-00095-6.

96 SAMOYLOVA, M. *et al.* Microscopic theory of photonic bandgaps in optical lattices. **Optics Communications.**, v. 312, p. 94, 2014. DOI:10.1016/j.optcom.2013.09.016.

97 PIOVELLA, N.; GISBERT, A. T.; ROBB, G. R. M. Classical and quantum collective recoil lasing: A tutorial. **Atoms**, v. 9, n. 3, 2021. DOI:10.3390/atoms9030040.

98 DAHAN, M. B. *et al.* Bloch oscillations of atoms in an optical potential. **Physical Review Letters**, American Physical Society, v. 76, n. 24, p. 4508–4511, June 1996.

99 PEIK, E. *et al.* Bloch oscillations of atoms, adiabatic rapid passage, and monokinetic atomic beams. **Physical Review A**, American Physical Society, v. 55, n. 4, p. 2989–3001, Apr 1997.

100 DEH, B. *et al.* Feshbach resonances in mixtures of ultracold ^{6}Li and ^{87}Rb gases. **Physical Review A**, American Physical Society, v. 77, n. 1, p. 010701, Jan 2008.

101 UNIVERSIDADE DE SÃO PAULO ESCOLA Politecnica Instituto GEOGRAFICO E CARTOGRAFICO. **Estação absoluta de gravidade. SP018**. 2020. Disponível em: <https://drive.google.com/file/d/1YsIwpntfR_zPbbBqxkqvLk9MKPhIQiD0/view>.

102 KRENZ, G. *et al.* Controlling mode locking in optical ring cavities. **Applied Physics B**, v. 87, n. 4, p. 643–647, Jun 2007.

103 KETTERLE, W.; DURFEE, D. S.; STAMPER-KURN, D. M. Making, probing and understanding Bose-Einstein condensates. ArXiv:cond-mat/9904034, Apr 1999.

104 LOUDON, P.; LOUDON, R. **The Quantum Theory of Light**. [S.l.]: Clarendon Press, 1983. (Oxford science publications). ISBN 9780198511526.

ANNEX A – PUBLICATIONS:

A.1 Hollow Bessel beams for guiding atoms between vacuum chambers: a proposal and efficiency study

DOI: https://doi.org/10.1364/JOSAB.395200

ArXiv [physics.atom-ph]: https://arxiv.org/abs/2010.09792v1

A.2 Progress towards a matter wave interferometer for inertial sensing with non-destructive monitoring of Bloch oscillations

DOI: https://doi.org/10.48550/arXiv.2108.13516

ArXiv [physics.atom-ph]: https://arxiv.org/abs/2108.13516

APPENDIX

APPENDIX A – DATA ACQUISITION AND ANALYSIS

In the experiment, we deal with three main sets of data. The absorption images of the atomic cloud beat traces extracted from the spectrum analyzer and the traces of the cavity transmission are analogous to beat signals in certain experimental setups. Let us understand how to retrieve and analyze the absorption images.

A.1 Absorption imaging

We implemented absorption imaging on our system as a tool to characterize the atomic clouds. Essentially a resonant beam (*probe*) is shined to the cloud and the shadow produced (attenuation of the probe intensity) is captured by a CCD camera, as schematized in figure 48. The capture is done with a CCD camera (Thorlabs 340M-USB Fast Frame Rate) with a quantum efficiency of 46% at 461 nm. The software to control the camera and optimize the image acquisition is developed by us (**SrCamera**).

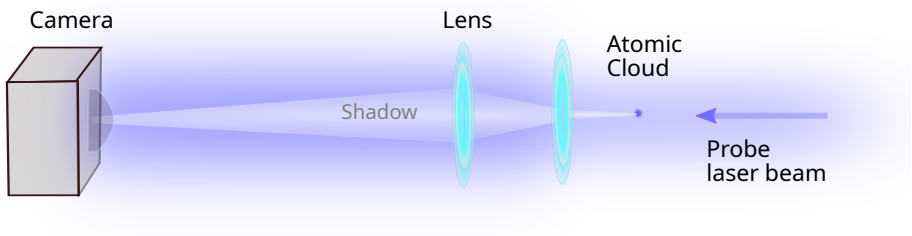

Figure 48 – Scheme of the Absorption imaging system: A resonant laser beam interacts with the cloud and the absorbed part is imaged in a camera to extract the OD. The lenses are used to zoom in (or zoom out) without losing resolution.

Source: By the author.

An image of the light after interacting with the atoms (I_{atoms}), an image of the light beam without the presence of the atoms (I_{probe}), and an image of the background without any light beams present (I_{dark}), are taken and used to compute the optical density of the cloud (See fig. 49).

$$\alpha(x,y) = OD = -\ln \frac{I_{atoms} - I_{dark}}{I_{probe} - I_{dark}} \tag{A.1}$$

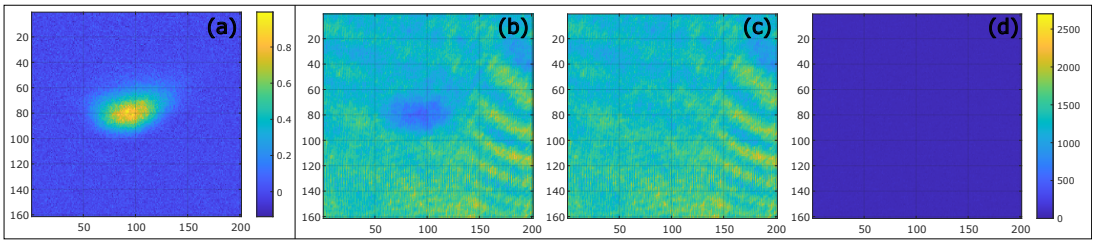

Figure 49 – a)OD: Resulting OD image of an atomic cloud. b) I_{atoms}: image of the light absorbed by the atoms. c) I_{probe} image of the probe beam without atoms. d) I_{dark} Dark image containing information of the camera noise (Without atoms and probe beam).

Source: By the author.

The local attenuation of the beam intensity (I) can be related to the absorption coefficient α, also called optical density (OD), with the atomic density via the Beer-Lambert law, $I = I_0 e^{-\alpha(x,y)}$:

$$-\ln\frac{I(x,y)}{I_0} = \alpha(x,y) = \sigma(\Delta)\int n(\mathbf{r})dz \quad \text{with} \quad \sigma(\Delta) = \frac{\sigma_0}{1+4(\frac{\Delta}{\Gamma})^2+\frac{I_0}{I_{sat}}} \tag{A.2}$$

Where $n(\mathbf{r})$ is the density distribution of the cloud and $\sigma(\Delta)$ the optical absorption cross-section with $\sigma_0 = \hbar\omega\Gamma/2I_{sat}$ the on-resonance cross section.

Another parameter that we can extract from the image of the optical density is the size of the cloud. This is done by fitting a Gaussian profile centered in the cloud for each axis of the image, as it can be appreciated on the insets of figure 50. With this information, we can then calculate all the parameters that describe our cloud. An analysis program that we created ourselves can automatically calculate for us: the atom number, the density of the cloud, peak density, temperature, etc.

Temperature measurement

A direct measurement of the temperature can not be realized since any test probe would disturb the equilibrium of the system.(103) The time of flight technique (TOF) can be useful to estimate temperature with great accuracy. We can take advantage of the thermal expansion of the cloud after its release from the trap.

Since the expansion of the cloud after a time t_{TOF} will affect the density distribution ($n(\mathbf{r})$) as:

$$n(\mathbf{r}) = n_0 e^{-mv^2/2k_BT} \quad \text{with} \quad \mathbf{v} = m\mathbf{r}/t_{TOF} \tag{A.3}$$

The trapping potential of the cloud can be, in a linear approximation, considered Gaussian. Hence we can approximate the density distribution as:

$$n(\mathbf{r}) = n_0 e^{-\mathbf{r}^2/2\overline{r}^2} \quad \text{with} \quad \overline{r} = t_{TOF}\sqrt{\frac{k_BT}{m}} \tag{A.4}$$

With $\overline{r}$ the rms (root-mean square) or full width ($1/\sqrt{(e)}$) of the cloud, and k_B the Boltzmann constant. Hence the temperature T can be written as:

$$T = \frac{m}{k_B}\left(\frac{\overline{r}}{t_{TOF}}\right)^2 \tag{A.5}$$

A.2 Experiment: Control and analysis programs

The previous calculation needs to be performed for each image individually, and the extracted data saved properly. We developed an analysis program that automatically performs the analysis. The interface of the **Sr Process©** can be appreciated in figure 50.

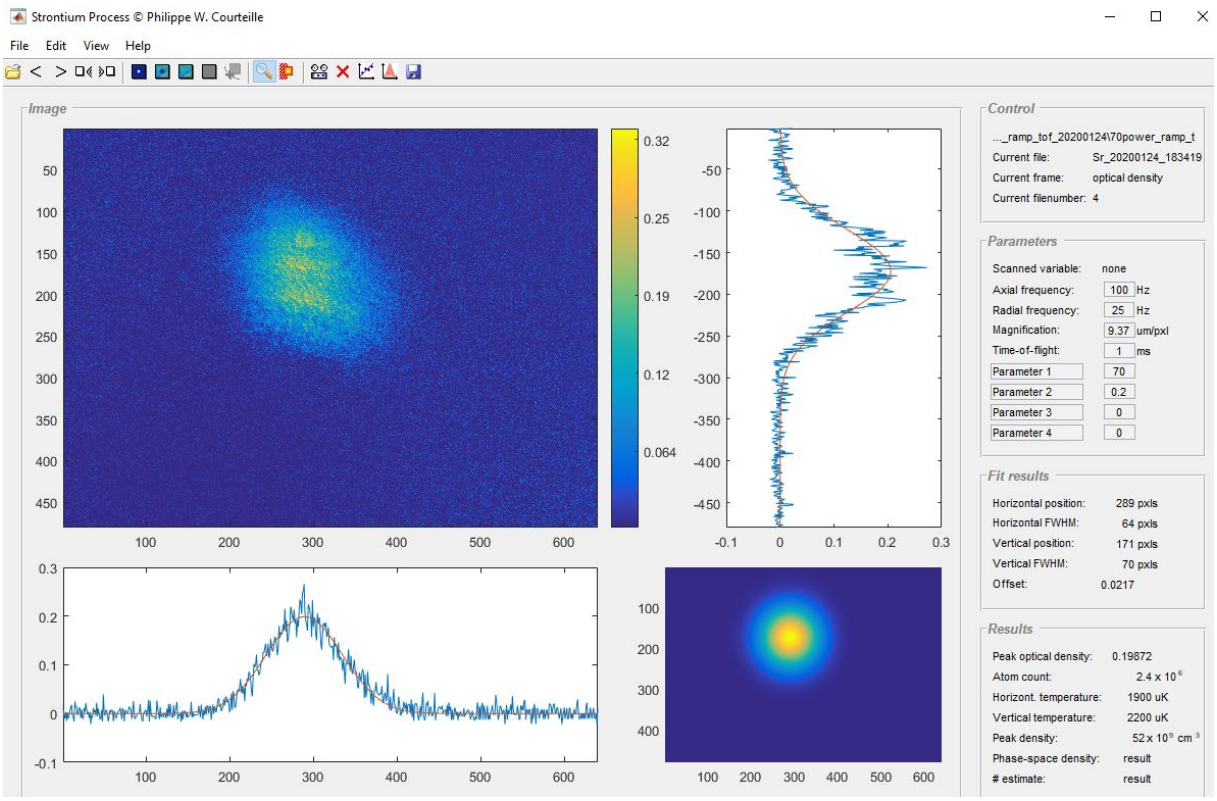

Figure 50 – Interface of our analysis program, *SrProcess* © : An image of the OD of the Blue atomic cloud is being analyzed and the results are shown in the rightest panel. The op bar offer tools to treat the images, as well as visualization. Traces taken from the oscilloscope are also accessible through those buttons. Automatic graphs generated from the analyzed data can also be displayed.

Source: By the author.

Visualization of the oscilloscope traces and automatic plot of the extracted parameters are among the utilities of the SrProcess program.

The program that controls the boards, and executes the experimental sequence was also programmed by us (**SrControl**). MATLAB® is the platform that runs our control programs. The **SrControl** is responsible for the coordinated distribution of triggers to each of the digital interface boards connected to the devices of the experiment. Each

device has an inner calibration already integrated into the sequence of the SrControl. We have 2 main control boards, the PCI6723 from national instruments (NI) is mainly used to control Analogic Outputs and has a time resolution of $20\mu s$. A PCI6259-NI is our fast board with a time resolution of 1μs and it's used to implement fast switches and the modulations and ramps of the red cloud frequency. As most of this Ph.D. thesis was

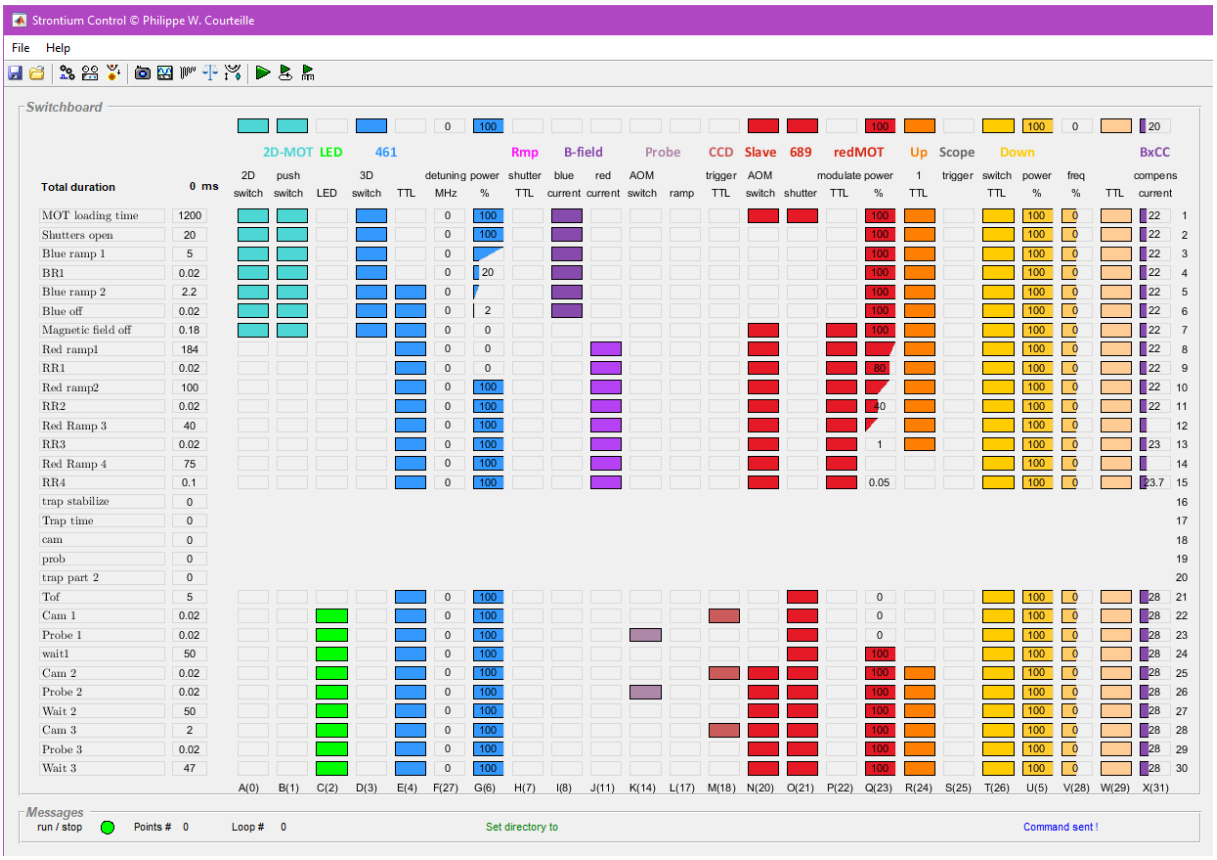

Figure 51 – Interface of our control program, *SrControl* ©: The top bar represents the steady state, or default experimental parameters. The different color boxes are organized in a color scale related to their appearance in the experiment. The vertical direction is given by the time (second column from left to right). The time periods are established then by rows, and an experimental trial begins at period **5**. The sequence for the Blue-MOT is pictured until period **5** and afterward, the Red-MOT sequence is programmed until period **13**. From period **21** until period **30** the absorption imaging sequence is executed in this script. The colored vertical bars represent each of the controlled channels (Analogic and TTLs) already named accordingly to the experimental parameters. At the top right panel, different tools can be called, among those we have: automatic communication with the *SrProcess*, simulation of TOF images, call the *SrCamera* (activates record of images), data recording of the oscilloscope traces, modification of the modulation matrix created in the fast board, calibration of channels, simulation of experimental parameters as well as remote control of extra external devices.

Source: By the author.

performed by the author, a big part of her work was focused on automatizing the data

acquisition as well as device control and monitoring to ease the Laboratory work. In that way, we now have a control program that also integrates with: the Camera control and acquisition of images, oscilloscope configuration, data acquisition, frequency generator configuration, and control. Additionally to the controlled devices, the program contains an option that automatically transfers data to the *SrProcess*, as well as some extra useful functions for calculating or simulating experimental parameters.

A print of the Graphical User Interface (GUI) of the *SrControl* as well as an experimental sequence can be appreciated in figure 51. The top panel (de)activates the different tools and devices. The colored top bar inside of the *switchboard* panel represents the 'steady-state' stage. Later on, a big colored matrix shows the experimental sequence executed on an experiment. The rows are time periods and the columns represent each of the controlled channels (Analogic and TTLs) already named accordingly to the experimental parameters.

Besides the aforementioned information, our SrControl program creates a file for each measurement with all the information of the sequence realized at the time. This file together with the camera images, as well as the traces of the oscilloscope and the devices information, is saved in a low-weight (size $< 1,257$ kB) file format (.par) that can be easily read for the SrProcess program, as well as any other data analysis program.

APPENDIX B – LIGHT MATTER INTERACTION FORCES

The computation of the forces of light excerpt in the atoms could give us a better understanding of the dynamics. For this the atom is described as a two-level system, where the excited level $|2\rangle$ is decaying to the fundamental level $|1\rangle$ with a rate Γ, ω_0 is the frequency of the transition and ω is the frequency of the laser, which can be detuned from the resonance using technical devices $\Delta = \omega - \omega_0$, now consider the Hamiltonian describing the atom-light interaction: (77)

$$\hat{H}_{int} = \hbar\Omega(\hat{\mathbf{r}})e^{i.\mathbf{k}.\hat{\mathbf{r}}}\hat{\alpha}^{\dagger}\hat{\sigma} + \text{c.c} \tag{B.1}$$

where $\hat{\sigma} \equiv |1\rangle\langle 2|$ is the atom transition operator, $\hat{\alpha} \equiv \sum_n |n\rangle\langle n+1|$ is the photon annihilation operator and $\hbar\Omega(\hat{\mathbf{r}}) \equiv \mathbf{d}_{12}.\mathbf{E}$ is the Rabi frequency, $\mathbf{d}_{12}$ the transition dipolar matrix element and $\mathbf{E}$ the electric field amplitude of the light. Using the semi-classical density operator $\hat{\rho}$ we can calculate the force that the light field exerts on the atom,

$$F(\mathbf{r}) = \langle \hat{F(\mathbf{r})} \rangle = -\text{Tr}_{at}\hat{\rho}\nabla_r \hat{H_{int}} \tag{B.2}$$

$$F(\mathbf{r}) = -\frac{1}{2}\hbar\sum_j \langle j|\,\hat{\rho}\nabla_r\left(\Omega(\mathbf{r})\exp\{i.\mathbf{k}.\mathbf{r} - i\Delta t\}\,|2\rangle\langle 1| + \Omega(\mathbf{r})\exp\{-i.\mathbf{k}.\mathbf{r} + i\Delta t\}\,|1\rangle\right)\langle 2|\,|j\rangle \tag{B.3}$$

With the atom at the center of the coordinates system:

$$= \frac{1}{2}\hbar\nabla_r\Omega_0(\langle 1|\,\hat{\rho}e^{-i\Delta t}\,|2\rangle + \langle 2|\,\hat{\rho}e^{+i\Delta t}\,|1\rangle) - \frac{i}{2}\hbar\mathbf{k}\Omega_0(\langle 1|\,\hat{\rho}e^{-i\Delta t}\,|2\rangle - \langle 2|\,\hat{\rho}e^{+i\Delta t}\,|1\rangle) \tag{B.4}$$

$$= -\frac{1}{2}\hbar\nabla_r\Omega_0\left(\rho_{12}e^{-i\Delta t} + \rho_{21}e^{+i\Delta t}\right) - \frac{i}{2}\hbar\mathbf{k}\Omega_0\left(\rho_{12}e^{-i\Delta t} - \rho_{21}e^{+i\Delta t}\right) \tag{B.5}$$

The coherences $\rho_{12} \equiv \langle 1|\,\hat{\rho}\,|2\rangle = \rho_{21}^*$ can be substituted by the stationary solution of the Bloch equations(104):

$$\rho_{22} = \frac{\Omega^2}{4\Delta^2 + 2\Omega^2 + \Gamma^2} \qquad \text{and} \qquad \rho_{12} = \frac{(2\Delta - i\Gamma)\Omega^2}{4\Delta^2 + 2\Omega^2 + \Gamma^2}e^{-i\Delta t} \tag{B.6}$$

We obtain:

$$\mathbf{F}(\mathbf{0}) = \underbrace{-\frac{1}{2}\hbar\frac{4\Delta\Omega}{4\Delta^2 + 2\Omega^2 + \Gamma^2}\boldsymbol{\nabla}_r\Omega}_{\text{Dipolar}} + \underbrace{\hbar\mathbf{k}\frac{\Gamma\Omega^2}{4\Delta^2 + 2\Omega^2 + \Gamma}}_{\text{Radiative pressure}} \tag{B.7}$$

Defining the cross-section $\sigma_a(\Delta)$ and the resonant cross section for a 'classical' transition σ_{a0} as:

$$\sigma_a(\Delta) = \sigma_{a0}\frac{\Gamma^2}{4\Delta^2 + 2\Omega^2 + \Gamma^2} \qquad \text{with} \qquad \sigma_{a0} = 3\lambda^2/2\pi \tag{B.8}$$

And $\Omega^2 = \sigma_{a0}\Gamma I/\hbar\omega$

$$\mathbf{F}(\mathbf{0}) = -\frac{1}{2}\hbar\Delta\boldsymbol{\nabla}_r \ln\left(1 + \frac{2\Omega^2}{4\Delta^2 + \Gamma^2}\right) + \hbar\mathbf{k}\frac{I}{\hbar\omega}\sigma_a(\Delta) \tag{B.9}$$

From B.9, for $|\Delta| \gg \Gamma$ (away from resonance) we obtain:

$$\mathbf{F}_{dp} = \boldsymbol{\nabla}_r \frac{-\hbar\Delta\Omega^2}{4\Delta^2 + \Gamma^2} \xrightarrow{|\Delta|\gg\Gamma} -\boldsymbol{\nabla}_r \frac{\hbar\Omega^2}{4\Delta} \tag{B.10}$$

and:

$$\mathbf{F}_{rp} = \hbar\mathbf{k}\frac{I}{\hbar\omega}\sigma_a(\Delta) = \hbar\mathbf{k}\gamma_{sct} \tag{B.11}$$

In that way, we see that the **radiative pressure** is a dissipative force. It dominates close to resonance and is due to absorption and spontaneous emission, which together with a magnetic field gradient can be useful to cold down the atoms till the Doppler limit. Describes the force as a product of the number of photons in the incident beam($I/\hbar\omega$), the absorption cross-section, $\sigma_a(\Delta)$, and the recoil momentum per photon, $\hbar k$.

On the other hand, the **dipolar force** is conservative and it is normally used to confine (or shove out, depending on the detuning) the atoms, and the strength of the potential created is proportional to the intensity of the light beam.

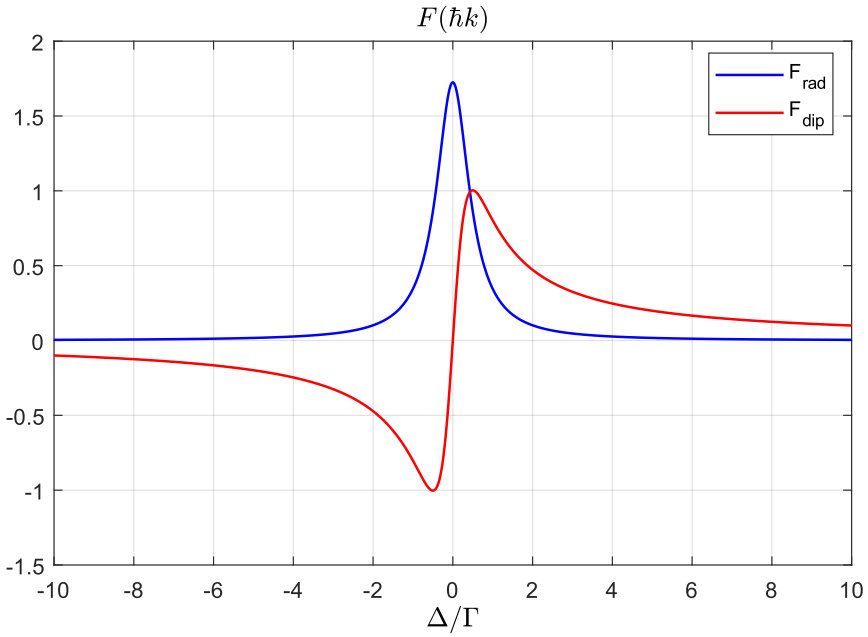

Figure 52 – Atomic Forces as a function of the detuning. The dispersive behavior of the radiative pressure can be understood easily when comparing the strength of the effects with the detuning from the resonance.

Source: By the author.

The orientation of the force depends on the light frequency as compared to the resonant frequency. when the frequency is tuned below ω_0, the force attracts the atom to regions where the light field is strong, when the frequency is tuned above ω_0, it attracts the atom to regions of weak fields. As seen in Figure 52, from the top to the center, in the vertical axes, the force will be repulsive, and will push the atoms away from the high-intensity regions. Analogously the bottom region will attract the atoms, with

a strength proportional to the gradient of I. The horizontal scale can also be separated into two regions, to the right of the center is blue detuned (associated with the decrease in wavelength), while the increase in frequency is normally referenced as tune to the red of the transition. Integration over the relevant spatial coordinates results in an effective potential or barrier to the atom.

Normally, when we talk about intensity, the saturation parameter is a more commonly term:

$$s = \frac{\frac{1}{2}\Omega^2}{\Omega^2 + \frac{1}{4}\Gamma^2} \tag{B.12}$$

And Eq. B.9 can be rewritten as:

$$\begin{aligned} \mathbf{F}_{dp} =& \frac{\hbar\Delta}{6}\frac{1}{1+s}\nabla s = \frac{\hbar\Delta}{6}\nabla ln(1+s) \\ \mathbf{F}_{rp} =& \frac{\hbar\mathbf{k}\Gamma}{6}\frac{s}{1+s} \end{aligned} \tag{B.13}$$

Eq. B.13 shows that the radiation pressure force 'saturates' as s increases, and is therefore limited by the spontaneous emission rate. The saturation parameter essentially describes the relative importance of terms appearing in the denominator of the line profile function for the light forces. The spontaneous emission rate is an intrinsic property of the atom (γ_{sct}), proportional to the square of the atomic transition dipole moment, whereas the square of the Rabi frequency is a function of the incident laser intensity (I).

If $s \ll 1$, the spontaneous emission is fast compared to any stimulated process, and the light field is said to be weak. If $s \gg 1$, the Rabi oscillation is fast compared to spontaneous emission, and the field is considered as strong. The line profile factor indicates a 'power broadening' by saturation of a factor of $\sqrt{2}$. Note that the dipolar gradient force and potential, Eqs. B.13, do not saturate when the intensity of the light field is increased.

INDEX

2D-MOT, 38

absorption imaging, 123
atom-field coupling, 77

Beat measurement, 45
Bloch frequency, 97
Bloch state picture, 98
Blue MOT, 39
Bragg reflection, 97
bunching parameter, 79

cooperativity, 77

Dali's art, 71
digital PLL, 59
dipolar gradient force, 66
displacement coils, 69
Doppler free spectroscopy, 37
Doppler temperature, 35

finesse, 62

injection Lock, 46

Optical lattices, 95

Red MOT, 44
Repumpers, 40
ring cavity, 62

saturation, 80
Strontium, 31

vacuum chamber, 33